Embedding Optical Sensors in Additively Manufactured Parts for In-Situ Performance Measurement

by

Kelvin J. Son

A thesis
presented to the University of Waterloo
in fulfillment of the
thesis requirement for the degree of
Master of Applied Science
in
Mechanical and Mechatronics Engineering

Waterloo, Ontario, Canada, 2021

Author's Declaration

I hereby declare that I am the sole author of this thesis. This is a true copy of the thesis, including any required final revisions, as accepted by my examiners.

I understand that my thesis may be made electronically available to the public.

Abstract

The aim of this project is to explore the potential of embedding sensors in additively manufactured metal parts towards smart product development. Smart product development is desirable due to its ability to detect product stress in-situ. There are challenges both in the construction of appropriate channels (for sensor embedding) in metal Additive Manufacturing (AM) and in packaging the sensor in an AM part for application-specific specimen measurands. Thus, this project investigates the feasibility of incorporating specific channels into AM parts for sensor embedding, packaging of the sensor in the parts, and the characterization of the sensor for sensing a given measurement. Primarily, Fiber Bragg Grating (FBG) sensors have been chosen for their compact size, ability to operate in hazardous environments, and their immunity to electromagnetic radiation. By creating such fiber-embedded smart products, it is possible to take preventive action for part failure by monitoring key areas of the product.

To see the feasibility of such development, stainless steel coupons were fabricated via laser powder-bed fusion (LPBF) and its fabrication parameters were optimized. LPBF uses lasers to melt layers of metal powder layer by layer for its fabrication. LPBF allows diverse material choices while giving more dense parts compared to traditional casting methods and has high part accuracy due to the small laser spot size utilized. Parameters such as laser power, hatch offset, and print orientation were optimized to yield a channel best suited for embedding FBG sensor within the bulk of the material. Thermal epoxy was injected into the channel after the FBG sensors were embedded to package the sensors and effectively translate the stress from the AM-created part to the FBG sensors.

With the fabricated proof-of-concept coupons, various tests and simulations were conducted to characterize the property and performance of the coupons. This was done to compile a guideline for designing such a part in the future and to understand the overall feasibility of the design. Tensile tests such as cyclic and fracture tests were conducted to understand the accuracy of the sensors during deformation. A thermal test was conducted to understand the temperature sensitivity of the product. COMSOL simulation was utilized to explore the geometry limitations of the sensor when packaged inside of the AM part.

The obtained results and characterizations show that it is indeed feasible to embed FBG sensors in metal AM parts for its monitoring and enhanced functionality. 500 micron diameter channel was able to be fabricated via LPBF. Recurring trends were observed from the dataset and results corresponded with hypothesized theoretical results. FBG readings were able to accurately monitor cyclic test until 240 cycles and its plastic deformation. The condition of the AM parts can be predicted using the sensors and established guidelines from this experiment. This guideline is to be utilized as a foundation for future fabrication of smart products of varying applications.

Acknowledgements

First, I would like to sincerely thank Professor Ehsan Toyserkani for being a supportive supervisor that enabled me to be involved in projects and work that I truly enjoyed during my time at MSAM. I joined this research team to get into the field of additive manufacturing and his guidance allowed me to plant me feet firmly in the field.

Thank you especially to Professor Farid Ahmed for mentoring me throughout my Master's journey. His expertise in the field was greatly appreciated each time I needed some guidance or tips during my research.

I want to acknowledge my other co-workers Professor Usman Ali, Dr. Brian Zhang, and Dr. Ehsan Marzbanrad for lending me their knowledge throughout the various parts of my research. Their expertise on their respective fields was invaluable to my work.

I also want to express my gratitude to Henry Ma, Grace Kurosad, Jerry Ratthapakdee, and Karl Rautenberg for helping my designs come to life and coordinating various tests.

Shout-out to everyone at the Multi-Scale Additive Manufacturing Lab for not only helping me academically but also for being great people to hangout both inside and outside of the lab.

Finally, sending love to my family and friends who has always been by my side during and long-before my journey at grad school.

Dedication

This thesis is dedicated to my grandparents.

Table of Contents

List of Figures

List of Tables

Chapter 1
Introduction

Smart products that can live-track its stress can be designed by embedding fiber Bragg grating (FBG) sensors inside parts that are fabricated via additive manufacturing (AM). FBG sensors can monitor mechanical and thermal strain while being relatively simple in design and easy to incorporate. FBGs are commonly utilized in extreme environments due to their resilience, reliability, and consistency. Utilization of AM grants a design freedom where the host material can incorporate FBG sensors inside of it. This sort of design would be difficult to fabricate using conventional manufacturing methods. This thesis focuses on investigating the potential of creating such smart products and establishing a design guideline for future studies/products.

1.1 Motivation

Advancements in technology opens the potential of having manufacturing methods, processes, and controls connected to a centralized system. Production trends have been shifting towards such centralized systems where use of automation, customization, and data usage are prevalent. As such, creation of smart products that are connected to centralized systems are starting to be explored. Smart products are products that can process data, highly interconnected, and even give feedback regarding its external surroundings. Creation of smart products where sensors are embedded into a host material is desirable as live-time tracking of the product's measurands is achievable through this method. Products or parts that are critical such as valves in an aircraft or building support benefit heavily from being able to give live feedback on its status. FBG sensors are a good choice as a sensor in such applications due to its ability to be small and give reliable readings. They are immune to electro-magnetic interference and corrosion.

It is of interest to utilize the benefits of FBG sensors by embedding it into products to create smart products. By embedding FBGs into materials, it is possible to find various properties and parameters that the material is subjected to such as tensile and thermal stress [1]. When a material is subjected to normal strain in the form of tension or compression, it will subject the FBG inside to the tensile stress. When FBG sensor is stretched or compressed, the wavelength reflected will be different from when it is at rest [2] [3]. By looking at this shift in wavelength, it is possible to look at the strain the host material experiences. Just like tensile stress, change in temperature applies stress in the host material in the form of thermal stress [4]. The FBG can pick up the thermal strain by measuring the wavelength shift to calculate the temperature the material is exposed to. It is also possible to multiplex these capabilities. This means that on a single optical fiber, multiple FBGs can be put in a series with each FBG sensors having different capabilities [5]. These capabilities can be more than measuring mechanical and

tensile stress such as acceleration, pressure, gas, and liquid concentrations of chemicals such as carbon dioxide and carbon monoxide [6].

The aim of the research is to look at current limitations in the design of smart-materials due to printability issues and limitations of the FBG sensors themselves. Products made via additive manufacturing has limitations due to fabrication technology as the quality of the resultant part depends on machine parameters, part geometry, and orientation [7][8]. Optimal settings are needed to be determined first before any testing or work can be done to create a realistic, ideal samples. Orientation of the fiber inside the part needed to be looked at as orientation limits the usage of FBGs in complex geometry [9]. This is because FBG sensors obtain the most accurate data when they are parallel to the direction of the strain, their usage is limited when the orientation of the sensors is curved or misaligned as the accuracy of the readings decrease [10]. Thus, it was desired to see what the limit of such curvature would be while still maintaining an acceptable accuracy. By knowing this limitation, a guideline can be created when designing complex geometry for parts and tooling in the future so that the sensors can still obtain accurate enough readings. Other limitations such as the behaviour of the FBG sensors will be explored when they are under tensile stress or thermal stress. Finding out what their limits will be helpful for applications in Design for Additive Manufacturing (DFAM). In this research, characterizing mechanical and thermal stress will be the main objectives as these two are the core parameters of interest when looking at smart products.

1.2 Challenges

One of the challenges in this project was creation of a channel to accommodate for the sensors. There were previous studies where the sensors were attached along the surface of the host-material; however, this is a not ideal configuration as the setup did not properly reflect the stress the host material was subjected to. Instead, it is ideal to have the sensor along the core/center of the host material. For such reasons, an AM part with a channel needed to be created. The sensors are around 125 microns in diameter, while the channels must be at least 4cm long to accommodate for the testing equipment. This creates a very large length-to-diameter ratio which is not ideal in AM operations. Large length-to-diameter ratio is not desirable at it increases the chance of having a blockage somewhere along the channel.

Caution was taken regarding embedding of the sensors. This was due to thermal expansion coefficient differences between the host material and the fiber. Ideally, the bonding mechanism transfers the strain from the host material to the fiber seamlessly; however, this was outside the realistic feasibility of design. This is the benefit of creating a design guideline; the guideline is appealing as it would forego

the need to account for the expansion coefficient difference. Instead, it would show directly how the sensors are expected to behave once they have been embedded inside of the host material. Variation in expansion coefficient can be detrimental due to potential of creating additional residual stress inside of the host-material. Under elevated temperature or mechanical strain, the elasticity difference between the various components of the assembly could damage the sensors. Such facts were kept in mind of when deciding the appropriate bonding mechanism for the assembly.

Optic fibers in general are made up of silica, as a result, they inherently have a degree of flexibility to them. However, they are still prone to breakage due to their overall thinness and they can still snap when bent at a steep angle. Such geometrical limitation on the fiber's angular limit must be considered when designing a part that must accommodate it. Having a wide choice of fiber angle allows the designer to have more freedom when prototyping a part. A limited flexibility of the fiber poses a challenge when designing a part. In an ideal scenario, the FBG sensors are parallel with the external stresses upon it. If the external stress is angular to the installed orientation of the FBG sensors, its accuracy drops. As a result, the initial test was done in an ideal stress loading scenario, but realistic scenarios would need to be accounted for in future works.

Finally, the tests prepared in this research involved both tensile and thermal testing. Each test was to be done independently from each other. However, the FBG sensors are affected by both temperature and tensile stress. The elevated temperature may expand the host material, adding additional stress onto the fiber. This creates an incorrect reading from the FBG sensor as it will overestimate the temperature due to the additional stress caused by the thermal expansion.

1.3 Objectives

There are two main objectives with several sub-objectives for each:

1. Explore potentials of embedding of fiber Bragg grating (FBG) sensors in additively manufactured metal parts towards smart product development
   - 1.1 Look at current limitations in the design of smart products due to printability issues and due to the limitations of the FBG sensors themselves
   - 1.2 Integrate channels (for sensor embedding) in the AM part design and find optimized printer parameters for best printable coupons
   - 1.3 Study the packaging of FBG sensors in the optimized printed channels. For this, suitable adhesives and their performance in sensing will be studied
   - 1.4 Determine best method of embedding FBG sensors in coupons
2. Characterization of the embedded sensors in functional AM parts

2.1 Study the influence of sensor embedding (both channel geometries, location, adhesives, etc.) on characterization behavior

2.2 Perform detail characterization of the embedded sensors for measurands such as temperature, strain, force etc.

2.3 From analyzing the data obtained from the tests, develop a design guideline

Each of the objectives and the sub-objectives all follow a chronological order leading from an initial step to the next step. This can be seen visually in Figure 1.1.

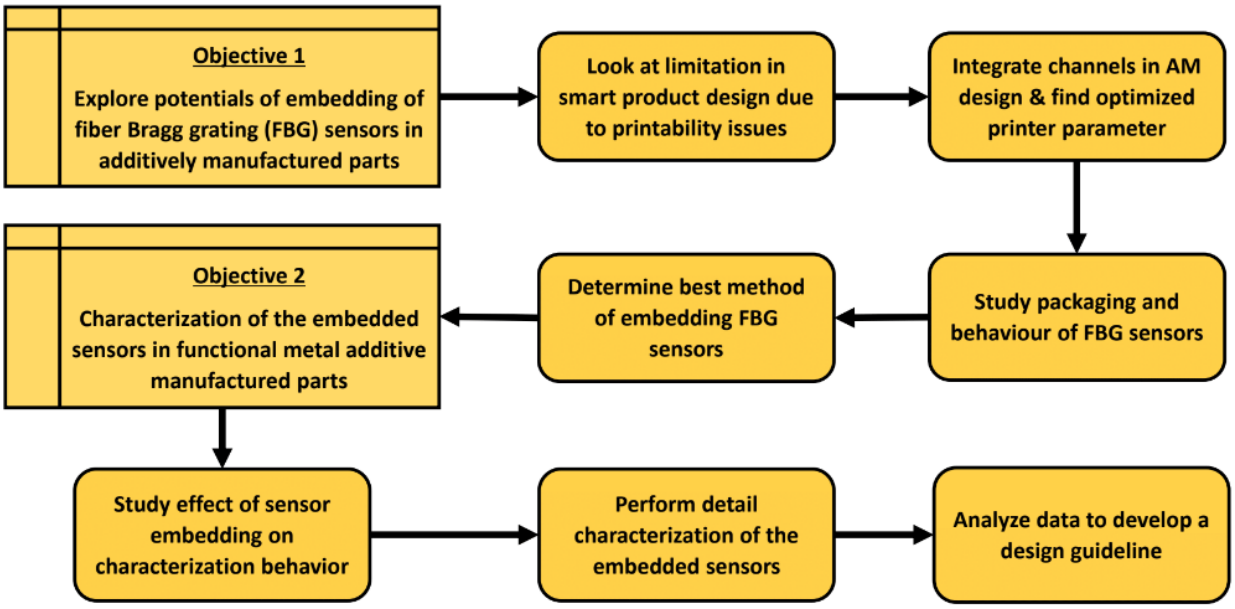

Figure 1.1 Objective Flowchart

1.4 Thesis Layout

This thesis is split into 5 chapters. The current chapter introduced the project, talking about the motivations, challenges, and objectives for the project. Chapter 2 discusses the necessary background research to understand this project such as overview of additive manufacturing, theory of fiber Bragg grating sensors, smart products, and embedding mechanisms. Chapter 3 talks about set up and design for the experiments conducted for testing FBG-Coupon assemblies. This section goes into detail why certain tests were chosen and designed in such a fashion. Chapter 4 shows the results from the experiments and discusses about them, talking about its significance for characterization. Chapter 5 starts wrapping up the thesis with conclusion for this research. It also discusses future steps regarding FBG-Coupon testing and potential of applying the characterization data into smart products.

Chapter 2
Background Research

In this background research section, literature review regarding topics relevant for this research was conducted. Before current research could be conducted, information regarding fiber Bragg grating sensors, additive manufacturing technology, embedding methodologies, and various applications of the topics were required to better understand the current technological limits for this study.

2.1 Fiber Bragg Grating Sensor

Fiber Bragg Grating (FBG) sensor is an optical fiber sensor where there are periodic phase structures called gratings along the core the of the fiber [11]. The fiber consists of a core surrounded by cladding that is usually made with polymer or glass-based materials [12]. The cladding and the core have different index of refraction values with the refraction value of the core usually being higher. This allows total internal reflection of light to occur which results in low level of signal loss. The grating is an interference pattern is inscribed on the core of the optical fiber [13]. This interference pattern can be created by intersecting two UV laser beams to create the pattern. Usually, around 1cm of the fiber is exposed to create the interference pattern. Inscription via laser permanently changes the index of refraction and it is stable up to operation temperatures of ~300°C [14]. This pattern at the core of the fiber acts as a reflector for a certain wavelength of light [1] [13]. The core of the grating has a periodic perturbation that works as a band-stop or band-rejection filter used in signal processing. Diagram of the FBG sensor can be seen visually in Figure 2.1.

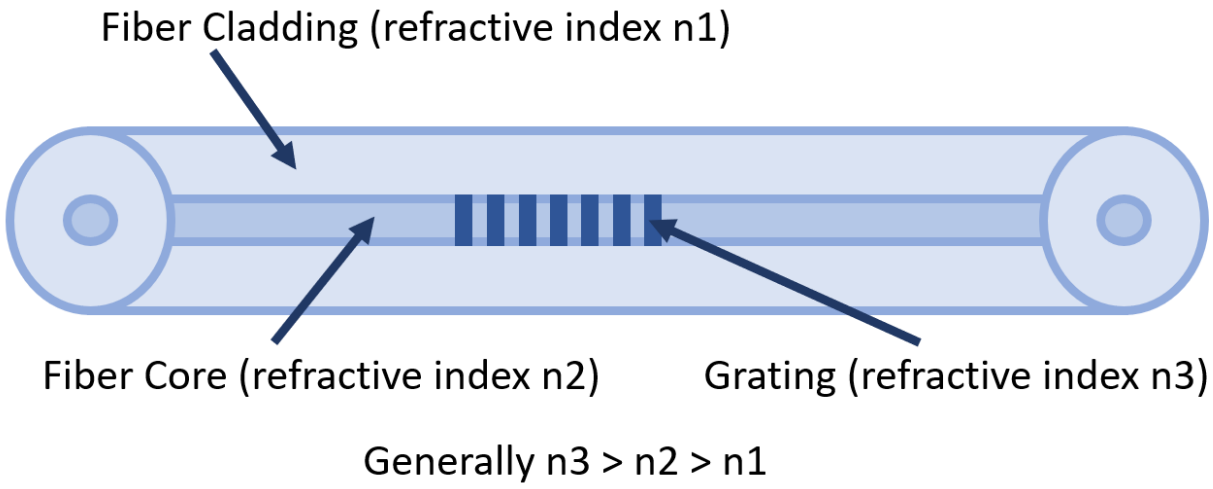

Figure 2.1 Optical Fiber Core with FBG

For the operation of the sensor, light from a laser is shined through a nominally monomode optical fiber and the grating reflects back a narrow range of wavelength of the original light. The original light's spectrum can be seen in the leftmost spectrum in Figure 2.2 [15]. The light that passes through the grating without getting reflected can be also seen in the middle spectrum. The reflected spectrum is the subtraction of the transmitted spectrum from the original [16]. This reflected spectrum is what is of interest as it is the spectrum required for measurements. In specific, the reflection occurs via successive and coherent scattering caused by the periodic perturbations of the grating [17].

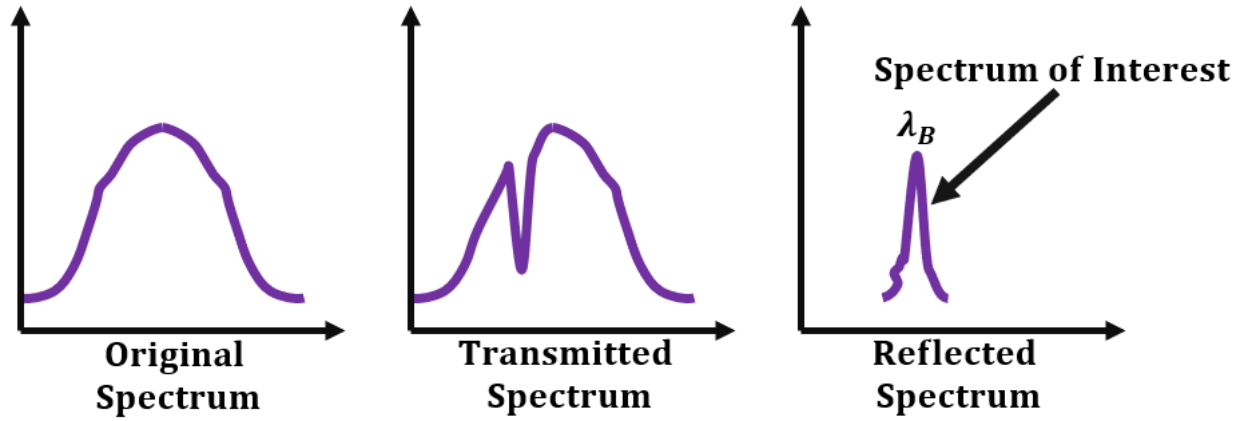

Figure 2.2 Spectrums in Fiber Optic Operations

Most intense reflection occurs at the Bragg wavelength λ_B, its equation being

$$\lambda_B = 2\eta_{eff}\Lambda$$

Where $2\eta_{eff}$ is the modal index and Λ is the grating period [13]. Usually, grating period varies between 0.6 to 1 μm. External influences such as temperature or strain will the modal index and grating period of the fiber, which changes the Bragg wavelength. This change in wavelength value is what is used to identify the type and magnitude of the external influences such as temperature or mechanical strain on the fiber. When the fiber expands/contract due to mechanical stress or thermal stress, the wavelength reflected back changes [18]. Since the modal index and grating period is in linear proportional relationship with the Bragg wavelength, this is makes in convenient to measure the strain of the fiber by looking at the shifted wavelength. Also, its proportionality makes it flexible to use in various measurements types from parts-per-billion to percent measurements [14]. Thus, strain sensing using FBGs are a matter of determining the wavelength of the light reflected by a grating before and after strain is applied [19]. Figure 2.3 shows the typical reflected spectrum for a uniform FBG sensor, with the Bragg wavelength occurring at 1500nm.

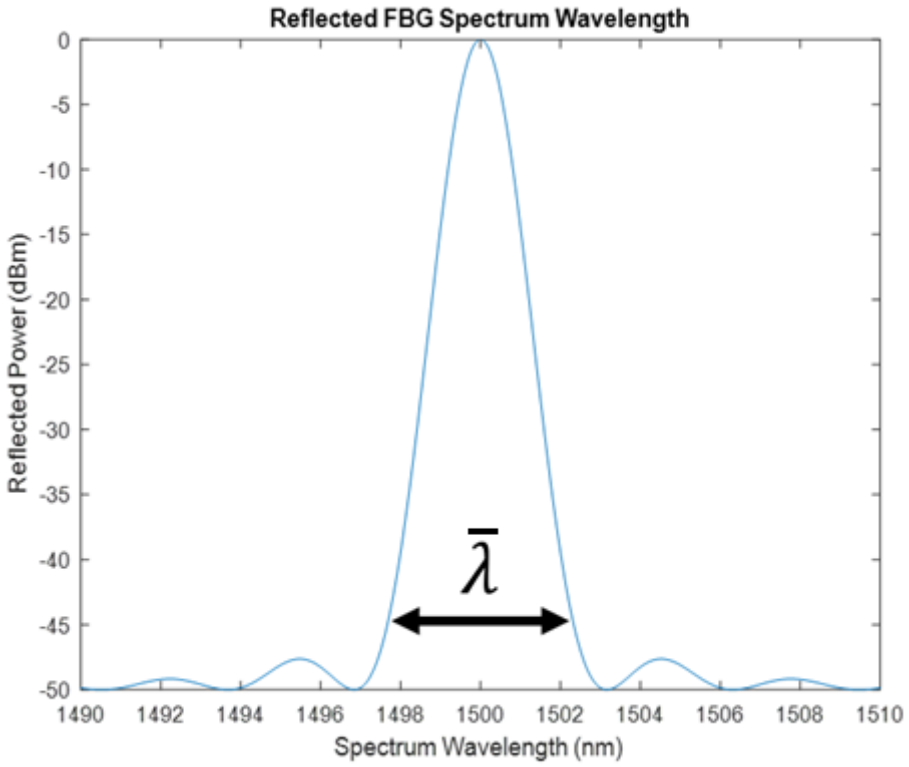

Figure 2.3 Reflected Spectrum of Uniform Grating

As mentioned, λ_B is the Bragg wavelength which is the wavelength at maximum reflectivity and $\bar{\lambda}$ is the bandwidth which is the distance between the first two minima of the spectrum [20]. When the fiber is put under tension or compression from external influences such as thermal, pressure, and mechanical stress, the wavelength shifts assuming that the grating is under constant stress throughout its length. By measuring the peak of the shift, the wavelength shift of the FBG spectrum is observed and used to determine the magnitude of the stress it experiences. As an example of expected FBG behaviour, Figure 2.4 shows an expected before and after behaviour of an FBG after it has been given tension. The initial spectrum would move to the right once tension is applied due to the increase in Bragg wavelength. The peak values of the spectrum before and after would be measured to determine the value of the stress.

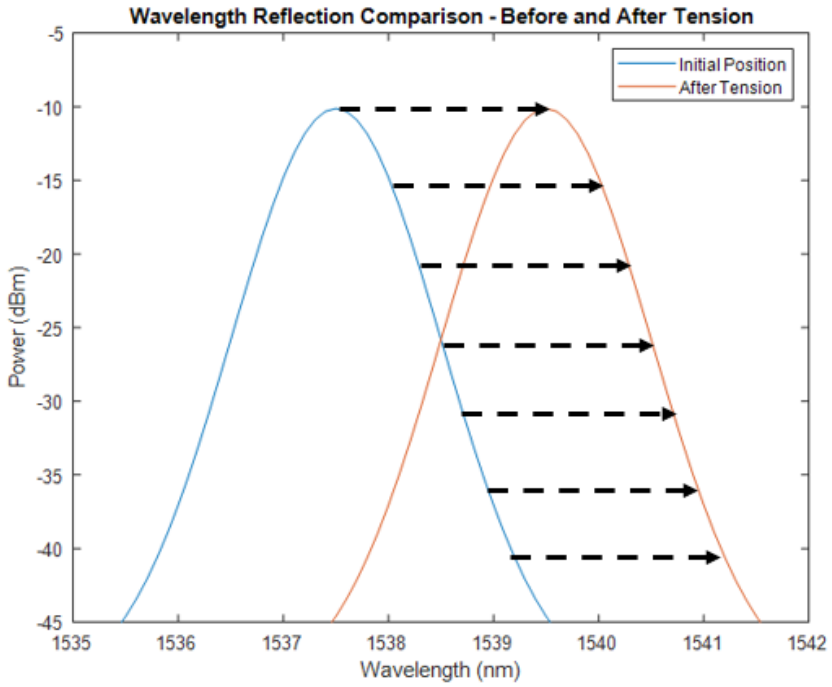

Figure 2.4 FBG Wavelength Shift Due to Tension

2.2 Fiber Bragg Grating Sensor Feasibility

Since FBG is an optical fiber sensor, it is undisturbed from electro-magnetic interference (EMI) and radio-frequency interference (RFI) [1]. FBG sensor has all the advantages usually attributed to fiber optic sensors such as being lightweight and compact while being reliable in hazardous environments with a long lifecycle [2]. Furthermore, FBG has the benefit of not requiring a reference point/data while providing an accurate measurement [21]. These advantages make it an attractive option over traditional electrical sensor options. Optical fiber sensor has the advantage of being highly sensitive and having a geometric versality as they can be bent/flexible. Furthermore, they are rather simple in design and can be operational in extreme conditions such as electro-magnetic interfering, high temperature, high voltage, high corrosion, etc. [22]. FBG sensors can be extremely robust if made of glass as glass has higher yield point than steel if the core is properly protected. The electromagnetically passive aspect of FBG allows it to operate in high and variable electric field environments, which is useful in the power industry. They are chemically and biologically inert since its material, silica, is untouched by most chemical and many biological agents. Fiber sensors can be physically small and light in weight; though, in some industries this can be a distinct disadvantage and large packages are required to conceal the small optics. Conversely, small size is sometime immensely beneficial in applications in biomedical measurements [23].

Similar usage of FBG sensor to determine thermal and mechanical stress has been done prior in prior research to monitor key areas of focus [24][25]. However, these studies were conducted with the FBG sensor taped on the surface of the host materials. FBG sensors were used to determine localized thermal and mechanical strain during cold spraying process. Embedment of FBGs were able to properly determine the thermal and mechanical strain the host material experienced during cold spraying [27]. Using FBGs to simultaneously determine both thermal and mechanical stress of a material has already been proven [26]. The sensors were shown to be able to measure strain in a rotating bending cyclic test with high level of accuracy and repeatability[30]. Prior studies have been conducted where two of the FBG sensors are in series to have a dual parameter fiber where it is possible to measure both the temperature and mechanical stress with a single fiber optic cable [4][6][28]. This method enabled was able to monitor the internal strain of a material at a relatively low-cost point with a simpler design compared to some of the existing alternatives [14]. Figure 2.5 shows an example of FBG setup schematic where multiple FBG sensors are connected for reading. These sensors can read various data such as tensile stress or temperature.

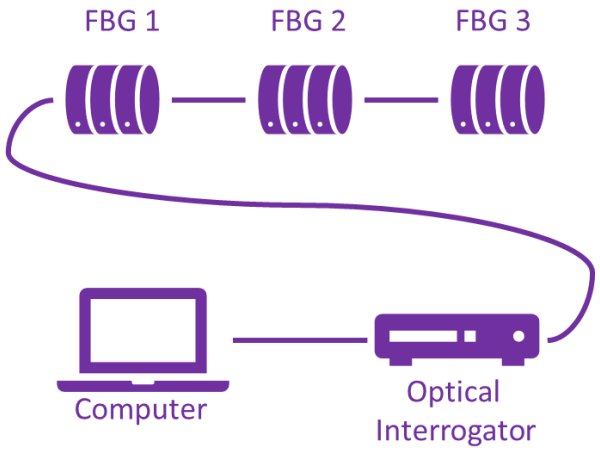

Figure 2.5 FBG Setup Example Schematic

It was seen in recent years that FBG sensors were preferred in the field of structural and infrastructure monitoring. They are used in applications such as roads, bridges, and ships [29]. This is due to their ability of measuring strain while being stable in harsh environments. FBG sensors were examined and tested to see their suitability for strain measurement in real-life scenarios. The sensors were tested in infrastructure materials for strain measurement and was found reliable in practical applications [31]. However, as mentioned, majority of FBG applications involved it simply being pasted onto the surface of the material. Such a design is not desirable as the core of a material/structure is the most key aspect in overall structural integrity. The center of the host material is likely to have different temperature

compared to the surface of the material as the source of heat/cooling would be from an external source. Thus, measuring only the surface of the material does not accurate reflect the entirety of the host material's status. This research differentiates from similar studies of the past as it focuses on testing smart product feasibility where the sensors are at the center/core of the host material rather than on the surface. To embed the fiber at the core of the host material, the usage of a substrate/bonding mechanism is a necessity. The usage of bonding mechanism for FBG measurement application has been previously proven [32]. In terms of accuracy of strain measurements, prior studies have shown that measuring host material properties via FBG sensors are feasible and similar in accuracy to those of traditional strain gauges [33]. If the accuracy of the FBG sensor for strain measurement is of upmost importance, there has been studies on ways to increase the accuracy of the sensors. By utilizing microstructure fibers, it is possible to enhance the overall sensitivity and accuracy of the FBG sensor [34].

For measuring temperature perturbations, FBG sensors were previously explored and have potential regarding its application. Utilized for advanced engineering materials such as carbon epoxy composite in extreme environments in low earth orbit settings, FBG sensors were found to accurately measure the composite's thermal expansion coefficient. In its application, FBG sensors were able to monitor the composite's thermal deformations for over 1000 aging cycles [35]. The fact that FBG sensors were able to be utilized in the most advanced engineering applications further highlight their potential impact once properly utilized and implemented. Although it is rarer, some FBG sensors remains serviceable at temperatures over 1000°C. For extremely high temperature operations, a femtosecond laser pulse irradiation can be utilized to fabricate the FBG sensor. By utilizing fabrication with pre-annealing treatment, it is possible to create high-heat resistant FBG sensors that function at 1200°C for over 20 hours of operations [36]. It is also possible to account for the substrate or bonding mechanism for thermal testing as it can be accounted for using dynamic temperature scanning where both the host-material and bonding mechanism are measured separately and used as a comparative reference [37]. FBGs can be utilized in extreme cold operations as well. In one research, FBG sensors were used to measure thermal expansion coefficient of polymers at cryogenic temperatures [38]. European Organization for the Nuclear Research (CERN) have previously tested polymer coated FBG sensors in operating conditions as low as 1.9K [39]. The purpose of the study was to have a way of measuring the temperature of superconductive magnets that are utilized in CERN's Large Hadron Collider (LHC). It was found that when various sensors were used throughout the magnet, it was feasible to be used as an accurate temperature monitoring system for the whole device. As the scale of the LHC is large, FBG sensors were found to be able to be utilized along the long distances of the superconducting cables in a reliable way. The signal quality they provided was deemed acceptable and the overall robustness of the fiber made CERN deem the technology as a promising to further research.

2.3 Smart Products

"Connectivity" and "Integration" have been the trend in the industry for the last few decades. As the IT industry started to boom, much of existing manufacturing methods, processes, controls, etc. have begun to transition from conventional methodologies of being standalone to being all connected to a centralized system. This trend has been coined as industry 4.0, where companies strive to have personalized products for each consumer, have minimal human intervention in processes, being data-driven, and utilize automation [40]. This enables the ability to monitor every single minute detail of a system which leads to efficient troubleshooting, quick resolutions, and high quality control. Industry 4.0 has the benefit of having a flexible yet fast production and overall high levels of customer satisfaction due to its ability to customize products for individuals. As of current, companies have successfully integrated most of their assembly processes to a central system. The next step in this transition is to be able to connect materials and products themselves via sensors. By creating such a smart product, it is also possible to monitor tooling and materials themselves.

Smart products are essentially products that can process data, highly interconnected, and even give feedback regarding its external surroundings. The definition of smart product is not always uniform, and its definition is sometimes different depending on research. They are sometimes called Intelligent Product and usually brought up in the fields of systems engineering and software engineering [41]. For the sake of clarity, in this research, smart product refers to the first stated definition above. The main idea is to have a product that is suitable for industry 4.0 where the transmission of external information being a distinctive feature from products of the old. Smart products are required to properly automate and functionally run production lines of industry 4.0 factories as the main idea behind it is having a data-driven and custom product [42]. In the following figure, the flow towards industry 4.0 can be seen.

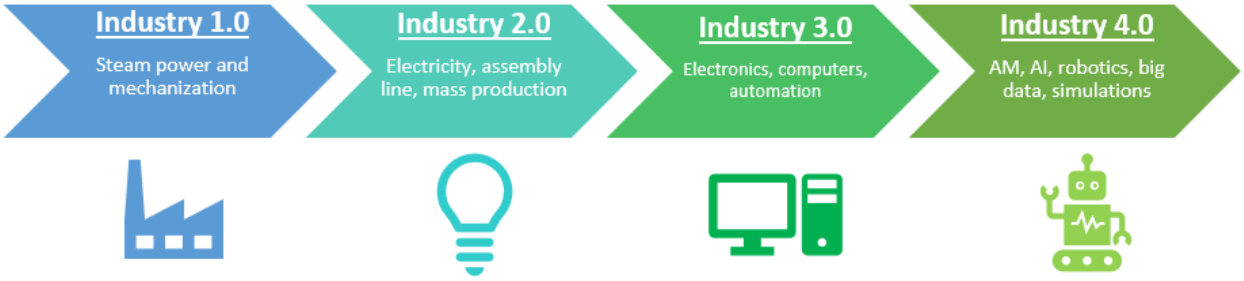

Figure 2.6 Industry 4.0 Flowchart

Creation of smart products are desirable in engineering applications as it can avoid serious/permanent damage to a part by tracking various live-time data of the part such as temperature, corrosive wear, etc.; thus, allowing preventive action to be taken before irreversible damage happens

[14][43]. Multiple properties at various key locations of the part can be found via embedment of multiple FBG Sensors. These FBG sensors can be embedded throughout the part and send back live-data to the central control unit [17]. The host material ideally has a channel embedded at the core to accommodate for measurements at the main bulk of the material. In a conventional product lifecycle tracking method, the lifecycle of a product and its reliability is usually conducted with accelerated lifecycle tests. Such tests have flaws as such approximation does not account for any unexpected events or cover all potential work condition the product will encounter during its lifecycle. Destructive evaluation and destructive testing are another conventional way of measuring product lifecycle; however, this adds overall time and cost to the product development as multiple product prototype and testing phases would be required. In a large infrastructure project, this would be substantial delay in cost and time due to the scope of the project itself.

Monitoring of products would primarily give assurance and confidence in the users utilizing the product especially as the product nears end-of-life (EOL) as users would look at the live data of the product rather than relying on an arbitrary guideline where the timing of the EOL would need to be estimated. There are also financial benefits of knowing the timing of EOL. Users can know what components are still serviceable when the product is discontinued, letting users keep/sell functional components, saving cost during EOL procedures [44]. By following conventional guidelines, some products are disposed when they could be serviceable for much longer; thus, costs could be saved by not making unnecessary replacements. Finally, by live-tracking component data individually, the user can compare via cost-analysis to see if they should scrap the product entirely or if the product can be functional much longer if certain components are replaced. Even in structural sensor applications, embedded ultrasonic sensors were found to be suitable replacements for conventional destructive evaluation testing [45].

2.4 Additive Manufacturing

For testing and readings of the prototype to be reliable, the host material should be able to incorporate the sensor in an efficient way. An important factor that affects the embedding process is the fabrication method of the coupons that would have the FBG sensors inside. For this research, Additive Manufacturing (AM) was utilized for its advantages.

2.4.1 Background/General Information about Additive Manufacturing

Desire for more complex and intricate manufacturing of parts has always been sought after. With the rapid advancements in manufacturing during the past 200 years, mass production of advanced products has been made possible. As the manufacturing capabilities increased, so did the demand for complex

products. Products are now desired to be durable enough to endure elevated temperature and pressure in extreme environments such as deep underground or outer space. As mentioned earlier, there are now demands to create smart products that can interact with the external environment. The material in which smart products are made of are often much difficult to work with in terms of manufacturing and post-processing. Difficult post-processing limits the complexity of creating a smart product as it will be harder to integrate electrical components as it is more difficult to create grooves and cutaways which the electronics can be mounted on the smart product.

Additive manufacturing (AM) is a rapidly growing field that is a very attractive alternative method of manufacturing for such applications. Unlike traditional manufacturing method where materials are removed or "subtracted" from the original piece, additive manufacturing creates a product by usually combining materials layer by layer or "adding" until a final product is created [46]. An example of an additive manufacturing process would be Stereolithography (SLA). This was first AM process that was commercialized and it uses an ultraviolet beam to solidify a layer of liquid photopolymer. After the first layer solidifies, the build platform moves down so that the next layer can be solidifies [47]. Visual of SLA printing can be seen below in Figure 2.7. Outside of SLA, more methods of AM have been developed due to technological breakthroughs. Different methods offer different benefits and drawbacks such as time, geometrical design freedom, strength, material selection, etc. Some of these methods include selective laser melting (SLM), fused filament deposition modeling (FDM), selective laser sintering (SLS), and electron beam melting (EBM).

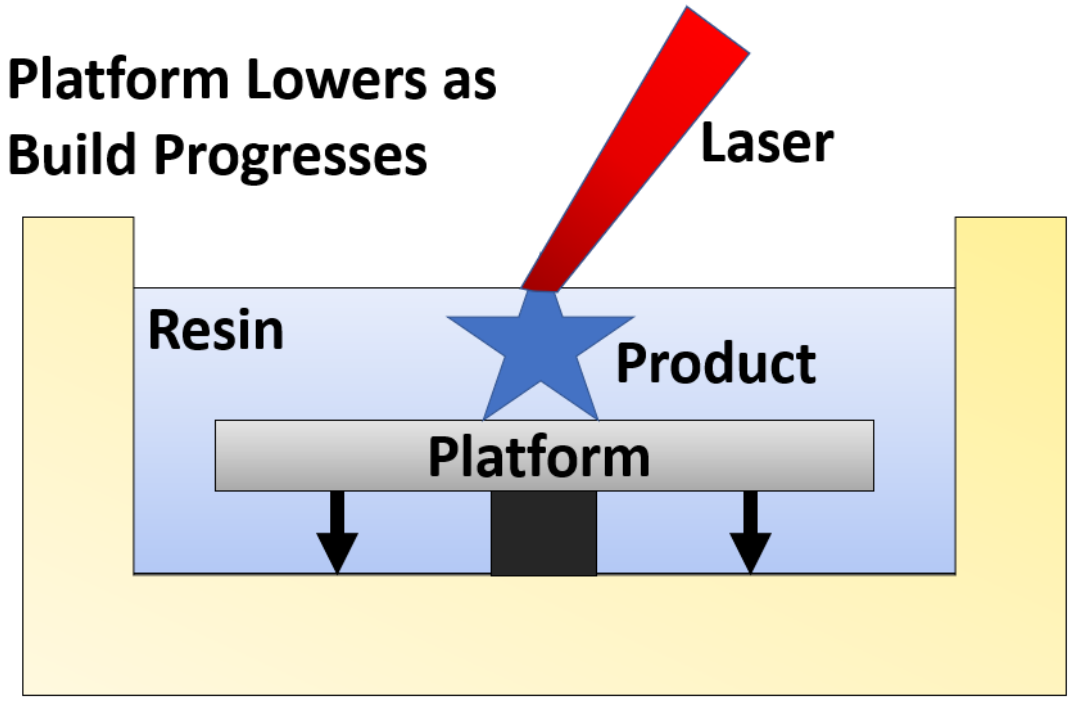

Figure 2.7 SLA Printer Schematic

Unlike traditional manufacturing methods which commonly requires the usage of custom tooling, additive manufacturing only requires computer generated 3D model file. Once generated, this 3D model file is sent to the machine that will print the said file without requiring modifications/customized parts for the machine [48]. In a more technical term, computer-aided design (CAD) file is created via a design software and then it is converted to a stereolithography (STL) file. When the file is converted to a STL file, it is simplified to a collection of triangles and sliced into layers that contains information of file that will be fabricated [49]. Figure 2.8 shows the technological steps for AM fabrication from design to implementation [47].

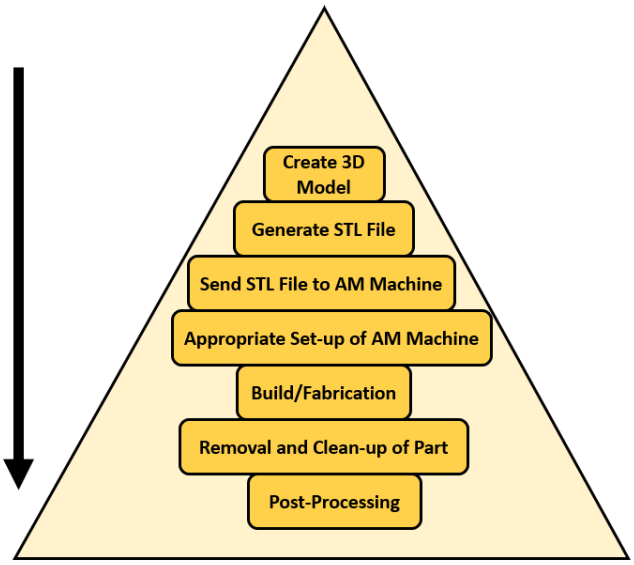

Figure 2.8 AM Technology Steps

Historically, rapid prototyping has been the main usage of additive manufacturing [50]. Due to AM not requiring change in tooling to accommodate for design changes, it has been ideal for rapid prototyping. Also, as rapid prototyping does not put heavy emphasis on the speed of fabrication, the low cost per unit price for small scale production make it a great choice [51]. However, now due to advancements in AM technology, it is an enticing choice for fabricating smart products. As mentioned before, complex geometry and strength of host-material are the limiting factors when creating smart products or other high-grade parts used in industries such as aerospace and biomedical. AM requires little to no post-processing and gives more design freedom for materials that are harder to work with [52]. AM increases the design potential of creating smart products as it allows fabrication of more complex geometry while broadening the material choices. Furthermore, it comes with the added benefit of being able to customize products and reducing impact on the environment [48]. In the recent years, the trend of customized/tailored parts for an individual consumer has been going on. This is evident in the biomedical field where custom implant parts are highly desired to ensure the best fit and comfort for the individual. With traditional manufacturing it is difficult to tailor such needs as dies/casts/molds would need to be altered for each custom part, making the fabrication process be unviable. Medical device industry has begun to use customized exact-fit medical implants that address the need for low-cost, quick parts [53]. Personal protective equipment (PPE) can also be custom fitted to ensure maximum degree of safety for the users. AM has benefit of being able to control microstructure of the material to a degree. This can be utilized to create PPE that maximize impact absorption [54]. The ability of customization can be further

applied to other industries including smart products where it gives the designers flexibility to alter the design for different users depending on their needs and applications.

2.4.2 Applicable Additive Manufacturing Techniques

Few AM technologies were considered to create the prototype of the FBG smart product test sample. One potential technology is Ultrasonic Additive Manufacturing (UAM). Main idea of UAM is utilizing ultrasonic vibrations to join/weld the layers together. The process can be seen in Figure 2.9, where a rotating sonotrode that oscillates ultrasonically is shown. Through this motion, ultrasonic vibrations are created to fracture surface oxides to conjoin metallic lattices between two desired layers [55]. These vibrations are around 20 kHz and applies a transverse force to the workpiece. This ultrasonic vibration combined with the normal force clamping down on the work piece welds the joined workpiece/layers together [55]. UAM would be utilized to build a part midway and paused so that the sensor can be placed on the half-completed part. Once the FBG sensor is secured, it would finish building to fully encompass the sensor [56].

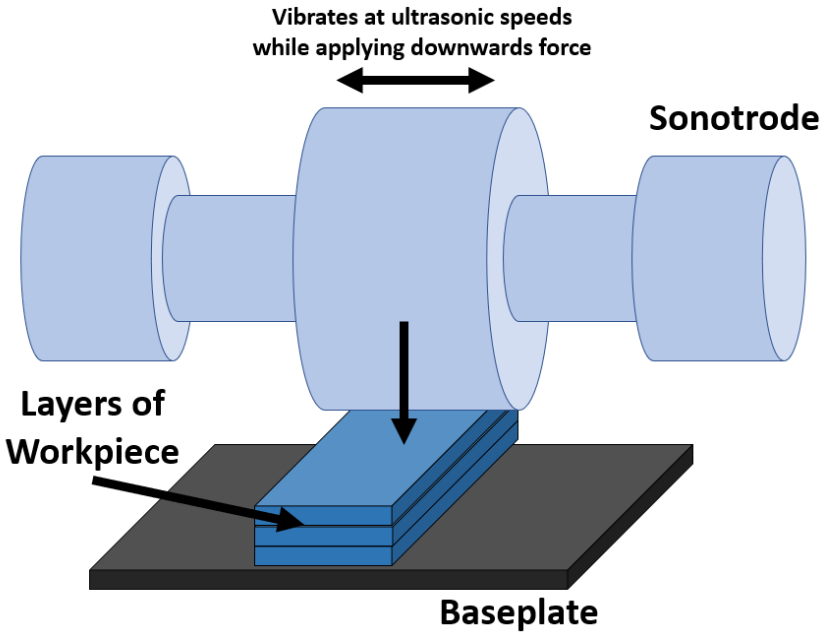

Figure 2.9 Ultrasonic Additive Manufacturing

UAM has the benefit of being able to reinforce selected areas in the workpiece. By doing this, it is possible to enforce the material where the highest stress concentrations are and save material by using less or lighter support materials on areas with low stress concentration [57]. As it utilizes ultrasonic vibrations instead of high input heat, UAM is beneficial as it can operate around room temperature. By operating at room temperature, the process avoids problems that arise from high processing temperatures

that some AM methods have [58]. This method is useful for bonding metals with different melting points and avoids problems that arise from solidification. Furthermore, it can avoid thermal damage to FBG sensors since some FBG sensors can get damaged in operation temperatures exceeding 400°C. For such reasons, UAM was utilized for some prior studies involved embedding of fiber optic sensors [56]. However, embedding with UAM have limitations as it is mostly only applicable on surfaces or channels that are closer to the surface. In the applications used in this proposal, the sensor is required to be at the core of the host material so UAM process was deemed inappropriate. Furthermore, UAM requires specialized equipment which was difficult to find access to.

Metal binder jetting is another potential AM technology that can be utilized for printing metal. The idea of binder jetting is that for each layer, the nozzle injects a liquid binding agent on a layer of metal powder. Schematic for binder jetting process can be seen in Figure 2.10 where the print head distributes the binder onto the layer of metal powder. The nozzle moves along in x and y-axis of the build platform to apply the binder for that layer. Once a layer is completed, build plate moves down along the z-axis and a new layer of metal powder is distributed along the top via a roller. Binder jetting has the benefit of being able to create complex geometric parts as they utilize binders compared to support structures used in other AM processes [59]. This allows the design to bypass some design constraints that come with supports. Binder jetting can be utilized fabricate colored parts by utilizing colored binders. These attributes combined with their lower cost and generally higher process speed makes them an appealing AM process to utilize.

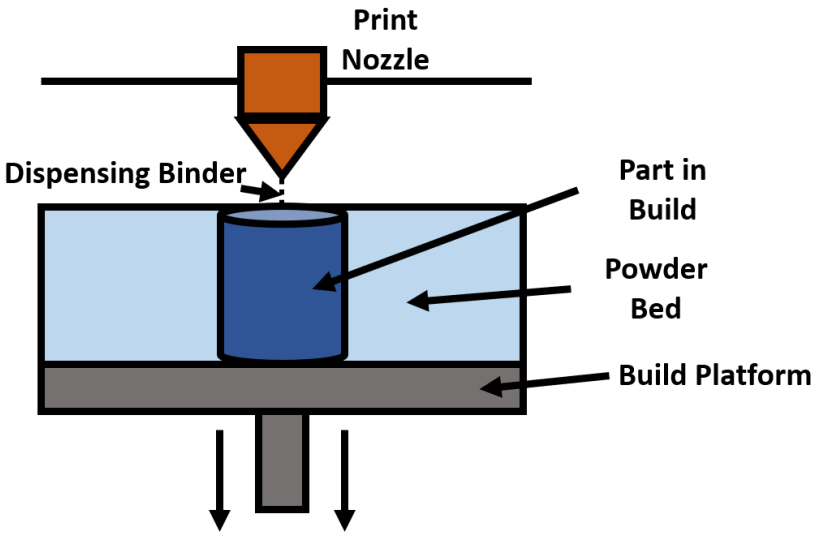

Figure 2.10 Binder Jet Process

However, binder jetting is limited in its overall structural strength and electrical/thermal conductivity. The process yields low mechanical strength compared to other AM processes, so it is usually followed up with post-processing such as sintering and infiltration [60]. This is due to the limitation in the packing/density in the packing of the metal powder used [61]. As the resultant part is not fully dense, it lacks yield strength and conduction compared to other AM methods such as SLM [62]. Furthermore, the process' main drawback is the limitation in material choice in comparison to laser-powder bed processes [59]. This is because the sintering post-processing is not hot enough to sinter some metals such as titanium. As the main goal of this project is to create a design guideline, it was judged that a fabrication method that can accommodate for more wide variety of material choice was to be chosen.

Finally, laser powder bed fusion (LPBF) fabrication technique was explored. LPBF is a type of SLM process mentioned in the AM background section. Just like binder jetting, LPBF utilizes metal powder; however instead of a binding agent, LPBF uses lasers to melt layers of metal powder on top of previous layers. Once a layer is completed, the build platform lowers, and a new layer of metal powder will be laid on top. Visual of the LPBF process can be seen in Figure 2.11 where the laser scans and melts the powder for the layer. Set by the United States' National Institute of Standards and Technology, a commercial LPBF system has max power of laser to be 195W with the layers being 0.02mm thick. The scan speed is set and operates at around 1m/s [63].

LPBF requires the usage of support to fabricate complex structures. Supports act as a mechanism to stabilize unsupported features in the design such as overhangs. Furthermore, it helps to maintain the structural integrity of the part during fabrication as the part can experience shrinkage during the solidification process. For LPBF and SLM processes, factors that affect the final part quality are layer thickness, scanning velocity, laser spot size, laser power, powder properties, scanning pattern, hatch spacing, and the operation temperature [64]. When creating a smart product, it is ideal to find an optimized value for the stated parameters.

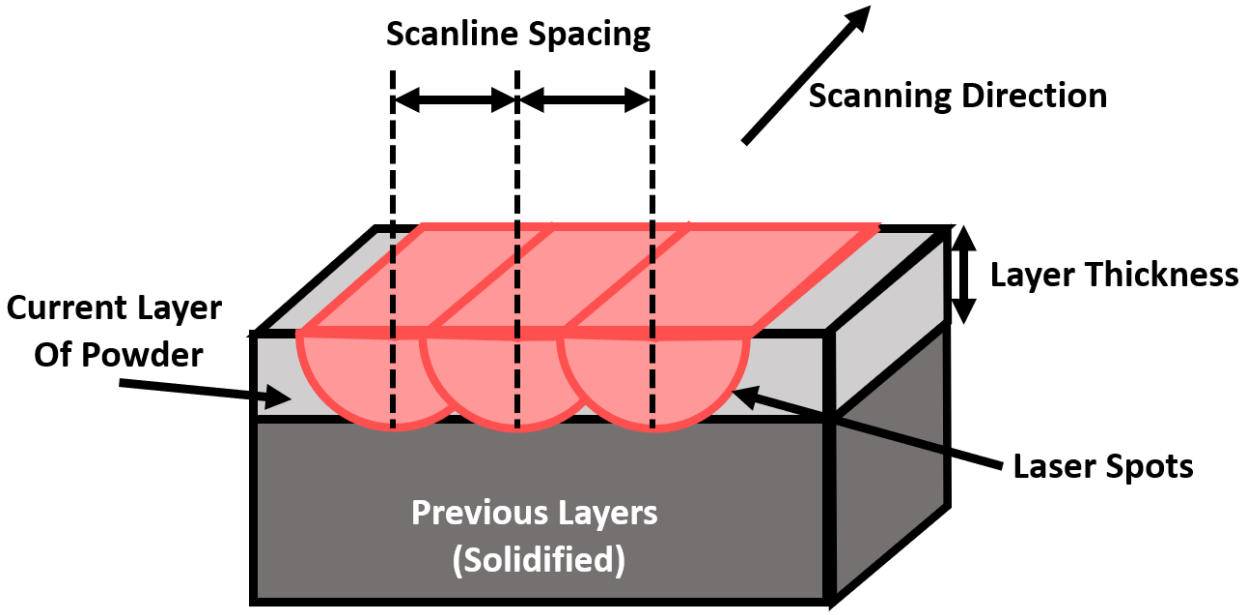

Figure 2.11 LPBF Process

The overall process speed of the fabrication ($\dot{V}_{process}$) is mainly affected by layer thickness (D_s), scanning velocity (v_s), and scanline spacing (Δy_s) which is the center to center difference between two adjacent laser spots. Following equation shows the build rate of the part in relation to the three variables [65].

$$\dot{V}_{process} = D_s * v_s * \Delta y_s$$

LPBF has high design freedom, allowing designers to create complex geometry while achieving near net shape manufacturing [66][67]. The design flexibility is due to the inherent design of SLM based procedures. By utilizing a laser beam to melt the powder, this offers the accuracy from the small spot size of the laser beam [68]. This allows the designer to create high resolution designs using LPBF. Furthermore, LPBF allows users to have extremely diverse material choice including aluminum, iron, stainless steel, titanium, chromium, nickel, copper, and alloy combinations of the stated metals [69]. In terms of resultant products, LPBF yields dense parts that can be stronger than parts made via traditional casting method [70]. For such reasons, LPBF process using Renishaw's AM400 machine was utilized for this project as it was deemed most suitable for the applications in this study.

2.5 Embedding Technology

A coupon with a channel size small enough to accommodate for the FBG sensor can be produced with relative simplicity by utilizing LPBF. However, to bond the FBG sensor inside the channel with a host material, a bonding material/mechanism is mandatory. As such, once the optimal coupons were printed, it

was important to find the optimal method to bond the FBG cables inside of the printed coupons. There are two factors to consider when looking at embedding fiber into a host material. First, the thermal expansion coefficient difference between the host material and the epoxy needs to be considered. The results obtained from testing will be analyzed to determine the characterization of the FBG sensors when they are embedded into the 3D printed stainless steel. To obtain the most accurate results, the strain caused by thermal or mechanical stress must be transferred exceptionally from the host material to the bonding material [32]. This transfer behaviour will be characterized to be used as a design guideline. Second factor is to look at is the bonding material between the fiber and host material, the material needs to be consistent throughout the channel to make the sensor-host material assembly more robust. Also, the bonding material must be in a condition where it stays at a stable equilibrium after several cycles of expansion and contraction.

One potential bonding material looked at was silver nanoparticle paste. When materials are in nanoparticle form, its characteristics significantly differs compared to its original form in bulk state. In nanoparticle form, materials have higher melting point and have higher thermal/electrical conductivity, which makes it easier to utilize as bonding materials [71]. In the recent years, silver nano particles have been utilized to bond semi-conductors to metallic structures [72]. Silver nanoparticles have the advantage of having high thermal conductivity and serviceable in high temperature which is desirable in FBG applications [73]. The paste needs to be sintered usually at temperatures exceeding 600°C with some pastes requiring external pressure to fully activate the paste [74]. However, as the material requires to be sintered or cured with a laser afterwards, they are more applicable in surface applications and not for embedment inside at the core of the material. There have been studies that have allowed the sintering process to occur at room temperatures [75]. The study utilized chemical reaction to reenact sintering effects via heat. However, the method is still a novel idea and are still in its infancy stage; therefore, silver nanoparticle paste was deemed not desirable for this study.

For this experiment, epoxies were considered as the ideal bonding material between the fiber and the host material. Epoxies have the benefit of being much more flexible than other bonding materials, offering high flexural strength. Epoxies also are great when bonding two different materials as is the case in the experiment. Its adhesive strength is excellent while offering good mechanical properties. In this study, polymer-based epoxy was determined to be the ideal fit. This is due to their low shrinkage rate after curing, excellent fatigue, and mechanical strength. They also have great resistance to thermal stress and degradation, which makes it a good fit to use for smart product applications. Polymer based epoxies have been utilized to embed FBG sensors into metallic parts in prior studies and tests which indicates their viability and bonding mechanism in the applications for this test [76][77]. Various epoxies were

considered such as: Master Bond's EP21TDCHT epoxy which is great to use in applications where there are dissimilar substrates, J-B Weld 8265S which gives bonding strength greater than steel, and Aremco 805 Ultra High Epoxy Resin which is used in applications where the epoxy is exposed to high temperature settings of up to 300°C. However, 353ND Optical Epoxy by Paisley was chosen to be used as a bonding mechanism. This because the 353ND is utilized in semiconductor, hybrid, and fiber optic applications while serviceable in high temperature environments.

2.6 Applications

By utilizing technologies such as AM and FBG sensors, the reality of creating economically and technologically feasible smart product and tooling is becoming achievable. As a result, investment in research for developing smart products are recommended for companies to stay innovative and ahead of competitions. Smart products allow creation and design of tooling and machinery that conventional materials are unable to achieve.

An example of such smart product would be in monitoring drills during downhole drilling operation. As seen in Figure 2.12, downhole drilling operations can occur several hundred meters below the surface as the item of interest for extraction is often below several layers of soil and aquifers. As a result, the drill is constantly in a high-risk environment due to factors such as elevated temperature and pressure while being several hundred meters away from operators and technicians. Currently when equipment fails or breaks, there are financial and time losses associated with it. There are replacement costs from broken pieces/parts; however, bigger losses stem from downtime from personnel and equipment. Furthermore, there are additional costs from retrieving/fishing out the broken parts/bits. By having smart tools that can live-track its damage, it is possible to prevent such losses from occurring. Such a smart drill can be created by applying AM technology for the creation of the drill as it can fabricate drills with complex geometry to accommodate for the FBG sensors that will do the tracking. As a distant future step, the stress and strain data obtained from key points around the drill can be used to develop an optimized design of the drill itself. By looking at where the critical points are and how much stress and strain it experiences, select areas can be strengthened while less critical areas can be made be optimized in terms of weight and cost.

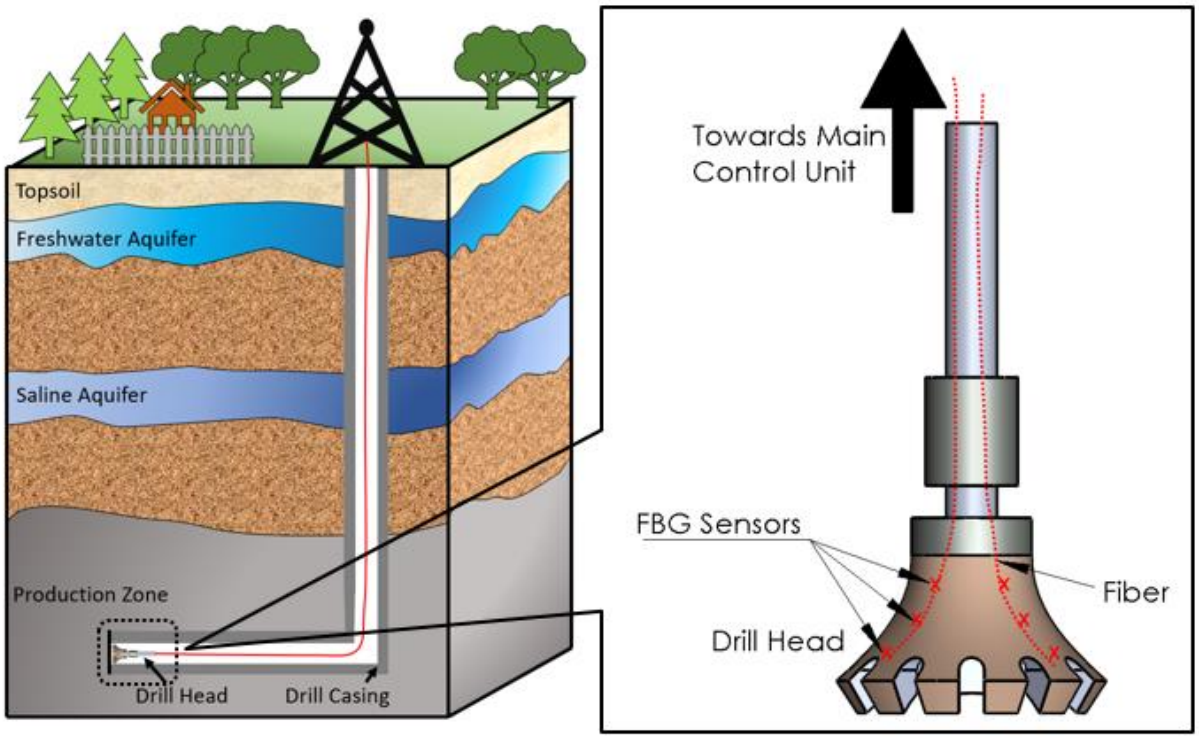

Figure 2.12 Downhole Drilling Operations

Another application of FBG with AM technology can be tracking of aerospace parts. Currently, there have been adoption of AM technologies in the aerospace industry. This is because parts in aerospace have complex geometry and must be operational in extremities, which means using high-grade materials that are often difficult to manufacture. To take a step further, such printed parts can be embedded with FBG sensors by designing grooves or notches. This way the part the user can track the part damage live time. Seen in Figure 2.13, FBG sensors can be potentially used to track various components within the plane. In aerospace applications, the crucial components should be monitored heavily as its failure can lead to catastrophic disaster. Furthermore, the FBG sensors on the wings can measure various surrounding parameters such as temperature, humidity, and pressure of the airspace surrounding the plane.

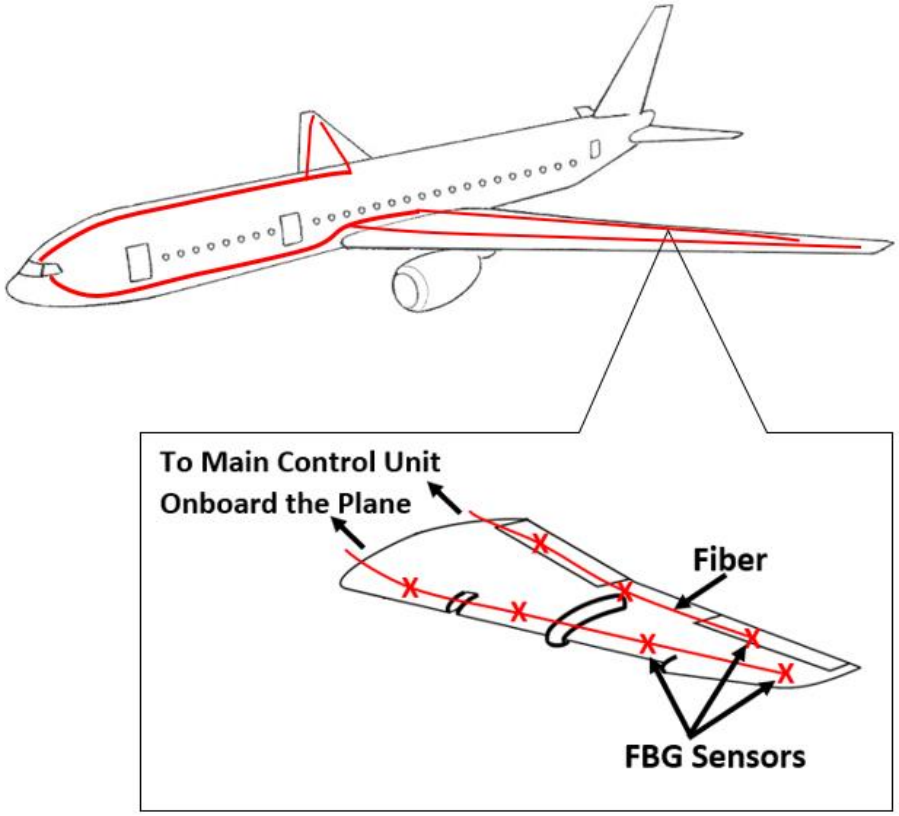

Figure 2.13 FBG Application on Planes

This research aims to act as a solid starting ground for developing such smart products. To design such tooling, the limitations in the design must be known as stated prior. Also, knowing the material characteristic when under mechanical or thermal stress will allow the designer to account for them and make any conversion/changes necessary in its corresponding operational environment. The characterization would be handy reference/guide when creating such tooling and smart products.

2.7 Summary

This thesis explores the combination of FBG sensors and LPBF to fabricate smart products capable of monitoring in-situ strain. As both fields/technologies are relatively new in development, literature on their combined application was limited and rare. However, there are still prior research and investigation that looked at their potential and feasibility in their combination [78][79][80][81][82]. Currently, FBG sensor are only embedded on the surface of the monitored material. This can lead to inaccurate reading of the material strain as residual stress within the material will be neglected. It is also challenging to fabricate a channel small enough to accommodate for FBG sensors within metallic structures by utilizing traditional subtractive manufacturing. This thesis aims to monitor strain along bulk

of the material by utilizing LPBF to fabricate channels and embedding FBG sensors to obtain more accurate strain readings experienced by the host material.

Smart products are products that are connected to a network, various sensors, and external environment. These products would be highly customizable based on needs and would be a highly data-drive device where feedback of the external environment would be utilized to better use the product. Usage of smart products have the benefit of monitoring their status to give assurance and confidence to the users as any failures/damages can be tracked live time. Fiber Bragg grating sensors can be utilized for the sensing of smart products due to its resilience and accuracy. FBG sensor are commonly utilized in extreme hazardous environment due to its functionality in high temperature, voltage, and corrosion environments. They have long lifecycle when properly maintained and is immune to effects of EMI and RFI. The sensors are light and have some degree of flexibility to them. Although not as widespread compared to traditional piezoelectric sensors, FBG sensors are used as well in industries such as aerospace and mining. However, if not packaged well, FBG sensors are prone to breakage and incorrect readings. Also, as the wavelength of the light needs to be read, they must always be connected to an optical interrogator to have live readings.

Additive manufacturing has the benefit of being able to fabricate complex geometry and having the ability to fabricate high strength materials. This allows higher degree of design freedom and allows smaller features to be added onto the product. LPBF allows material choices including aluminum, iron, stainless steel, titanium, and chromium. Currently, LPBF is used to fabricate metallic components used in biomedical, electrical, and aviation industries. They are commonly used to reduce the number of components used in an assembly and to create core components that require complex geometry. LPBF still has limitations as the finish is porous and the parts are not as strong compared to other methods such as forging.

Chapter 3
Experimental Procedure

3.1 Test Coupon Creation

Before running any tensile or thermal tests, a coupon of the host material was created. This is because a functional coupon with an embedded FBG sensor is to be used as a proof-of-concept before any smart materials or tools are created in the future. The dimensions of the coupon can be seen in Figure 3.1, the length of the coupon was around 4.33cm. The coupon was designed to be fabricated as short as possible to allow smaller channel diameters to be feasible in design. This is because as mentioned in the background section, a large length to diameter ratio makes the formation of a channel become more difficult. Due to the small diameter of the channel, the length must be reduced as much as possible. The FBG patterns inscribed on the fiber are around 10mm in length. For such reasons, the middle part of the coupon was designed at 12mm in length to accommodate for any minor shift of fiber inside the coupon. To make the tensile machine able to grip the coupon snugly, the grip portion length of the coupon was set at 10mm on each side.

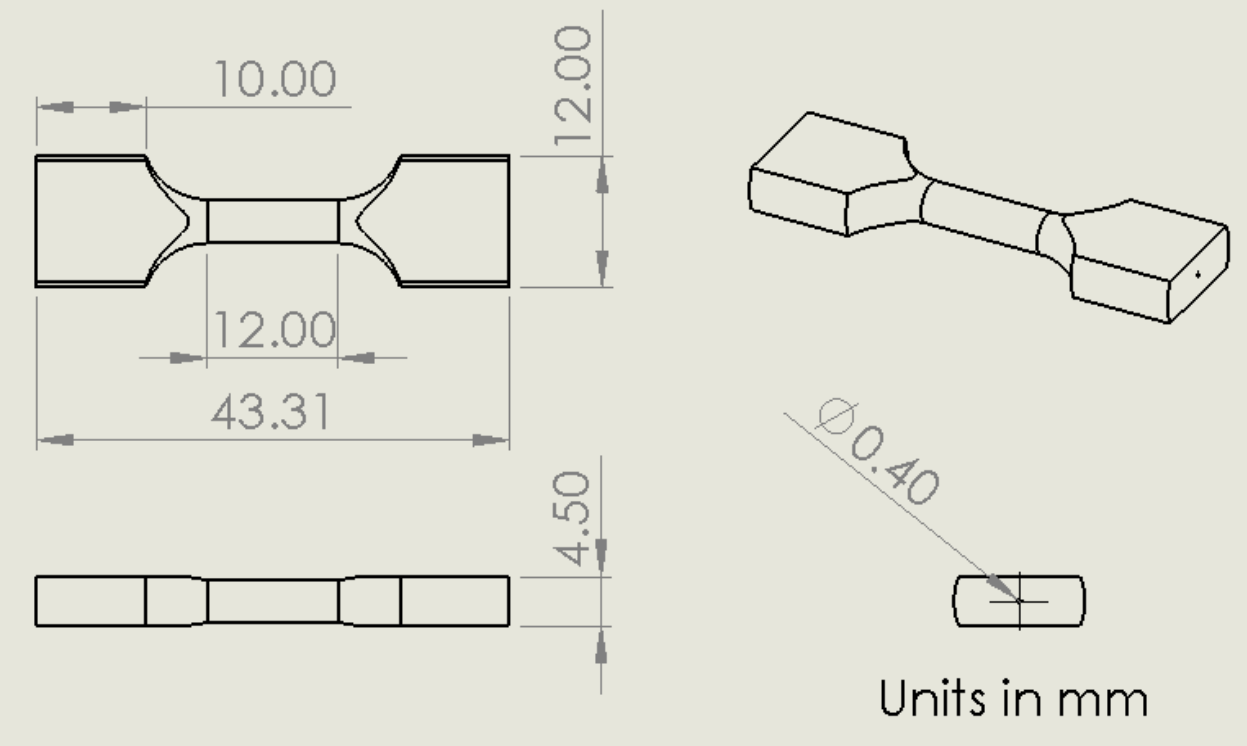

Figure 3.1 Coupon Geometric Diagram (400 Micron Dia. Channel)

The optimal coupons would yield a constant porosity throughout and contain a channel where the fiber can be embedded inside. The channel size should be just bigger than the fiber to have it embedded

securely. At the Multi-Scale Additive Manufacturing Laboratory, various stainless steel 316 coupons were printed using Renishaw's AM400 printer. Material chosen was stainless steel 316 due to its high strength and corrosion/water resistance [83] [84] [85], making it a great choice to be used in engineering applications. One of the sub-objectives involved finding the optimal printing parameter so parameters such as laser power, printing orientation, channel shape, and upskin/downskin parameters were all to be altered. Various printing orientation such as vertical orientation were to be tested as seen in Figure 3.2.

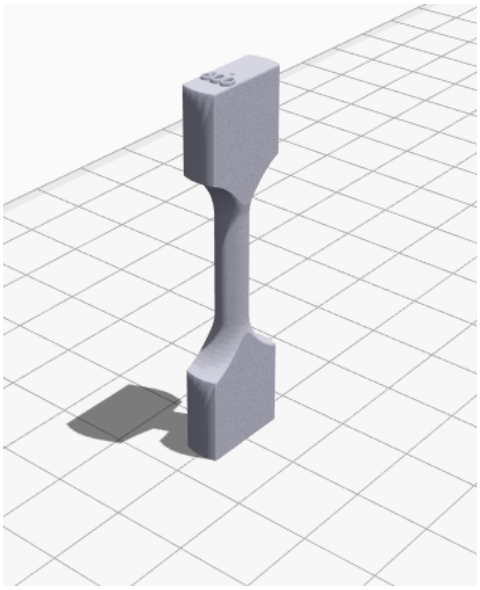

Figure 3.2 Vertical Printing Orientation

Table 3.1 Stainless Steel 316 Bulk Properties

Property	Value
Poisson Ratio	0.27
Density	$8000\,\frac{kg}{m^3}$
Young's Modulus	$193\ GPa$
Coefficient of Thermal Expansion	$17.5 * 10^{-6}$ in/in°C
Thermal Conductivity	$15\,\frac{W}{K^o}$

The fiber used was 250 microns in diameter and this can be further reduced to 125 microns in diameter if the jackets were stripped. Fabrication method chosen in this study was Laser-Powder Bed Fusion (LPBF). LPBF processes by nature creates melt pool during its fabrication [86]. This is of significance for small channel diameters as a melt pool offset inside the channel wall makes it likely for blockage to occur. If the size of the channel is too small, even a small melt pool can impact it along most

of the channel length. Longer channel length increases the probability of such formation happening due to the more numerous layer count during printing. At the same time, the channel cannot be too oversized as there may be issues regarding stress translation from host material to the sensor [10]. This stress translation must be efficient to get the most accurate readings [87].

The fiber and the presence of a bonding mechanism was thought to require at least 350 microns channel size for the coupons. Accounting for the uneven/rough channel wall formation during the fabrication process, minimum channel size planned for fabrication was 400 microns. To determine the smallest hole size usable for the study, various hole diameter sizes were printed starting at 400 microns up to 800 microns. Light was shined through each coupon's channel to see if was fully through. Initially, the test was done with a laser of 190W and the results can be seen in the results section. Depending on the result of the first batch, a second batch with optimized parameters was to be fabricated. Parameters that were altered and tested for the fabrication can be seen in Table 3.2 with their definitions below.

Table 3.2 Printing Parameters

Volume Hatch Distance	Volume Hatch Offset	Volume Fill Contour Distance
Volume Fill Contour Offset	Volume Border Distance	Downskin Hatch Offset
Downskin Hatch Distance	Upskin Hatch Offset	Upskin Hatch Distance
Upskin Border Offset	Laser Power	Print Orientation
Channel Size	Radius of Curvature	

Hatch Distance: Distance between laser scan vectors

Hatch Offset: How close laser gets to the edge of the build (boundary)

Fill Contour Distance: Distance between fill contours

Fill Contour Offset: Distance between last fill contour to the boundary

Border Distance: Distance between hatchlines and the boundary

Upskin: Area of the build where the angle of the area in relation to the bottom plane of the platform is greater than 0

Downskin: Area of the build where the angle of the area in relation to the bottom plane of the platform is less than 0

Laser Power: Output of the laser for the sintering process

Print Orientation: How the build is going to get setup geometrically

Channel Size: Diameter of the channel to embed the FBG in

Radius of Curvature: Radius of the curvature for the channel for the curved channel testing – will be discussed further in later section

The threat of internal residual stress is a potential issue during the fabrication of the host-material. Not just limited to LPBF process, the existence of residual stress is common to all metallic materials either coming from mechanical or thermal solicitation during the manufacturing process [88]. In LPBF, the residual stress is caused by high levels of thermal gradients present in the material. Residual stress can cause cracking and distortion which leads to the overall part failure [89]. Although it is possible to reduce the residual stress caused by the process, it is not possible to outright eliminate it [88]. The existence of the residual stress would affect the reading of the sensor once embedded. Seen in Figure 3.3, as the prior layers cool, it introduces residual stress inside the material due to shrinkage. During the fabrication process, a gradient of stress appears as various layers are at different temperatures. Also, as the material is subjected to external perturbation, it could change the magnitude of the residual stress within the material. This would result the readings having discrepancy when exposed to cyclic stress. Thus, there was the need to relieve the residual stress or calibrate the product so that the stress reaches an equilibrium, this solution is covered later.

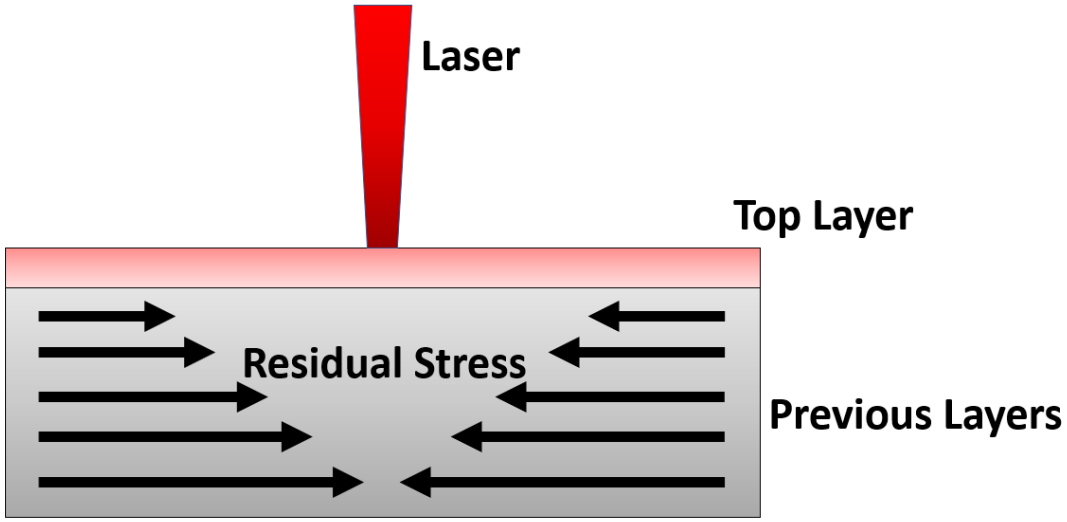

Figure 3.3 Residual Stress Representation

3.2 Embedding Coupons

After the coupon was prepared, it was put inside a beaker filled with ethanol and put into an ultrasonic cleaning machine for 1 hour. Ultrasonic cleaning machine uses ultrasonic waves to agitate the ethanol to clean the printed coupons. This was done to remove any debris that may remain within the channel of the coupon. For the FBG-Coupon assembly to have high reading accuracy, the bonding mechanism needs to have exceptional axial strain transfer from host material to epoxy [87]. This is because the host material needs to be able to translate the stress experienced efficiently to the FBG to have the most accurate

measurements [90]. For the applications in this study, polymer-based epoxy was determined to be the ideal fit. This is due to their low shrinkage rate after curing, excellent fatigue, and mechanical strength. Its elasticity would account for the expansion and compression rate difference between the fiber and the coupon. The model of FBG-Coupon assembly can be seen in Figure 3.4, the fiber was to be concentric to the coupon's neck and traverse through it completely. As stated in the background review section, 353ND Optical Epoxy by Paisley was chosen to be used as a bonding mechanism for the 316 stainless steel coupon and the FBG. This because the 353ND is utilized in semiconductor, hybrid, and fiber optic applications used in high temperature settings as well.

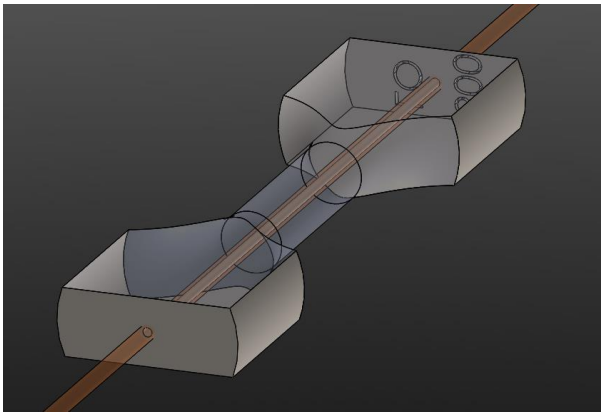

Figure 3.4 FBG-Coupon Assembly Schematic

The epoxy is a two-part epoxy, where there is a 10:1 ratio mix between the two parts. Each part was put into a separate beaker and stirred for a minute to evenly distribute the substrates within it. After, they were put together in the same beaker and stirred together for another minute. The material properties of the combined 353ND epoxy is as follows.

Table 3.3 353ND Epoxy Properties

Property	Value
Poisson Ratio	0.3
Density	$1180\frac{kg}{m^3}$
Young's Modulus	13.79 MPa
Coefficient of Thermal Expansion	$54 * 10^{-6}(below\ Tg), 160 * 10^{-6}(above\ Tg)$ in/in°C
Thermal Conductivity	$0.34\frac{W}{K^o}$
Index of Refraction	*1.56*

Fiber was marked beforehand on how deep to insert it into the channel as the grating portion of the fiber (10mm long) needed to be at the center of the coupon for the most accurate measurement. The fiber comes wrapped in a jacket and to reduce the number of layers the stress has to transfer from the host material to the actual core grating, the jacket was removed. The polymer jacket can be removed by dipping the desired section of removal in ethanol for about 10 minutes.

The fiber was then slid into the coupon's channel up until the marked point as the marked point at the channel entrances indicates that the grating is now at the center of the coupon. Once the markings line up with the edge of the coupon, the other end of the fiber is cut off as it is excess fiber. From this, the fiber would be along the entire length of the coupon. Finally, the mixed epoxy was poured inside a syringe with a 350-micron diameter tip and injected into the channel on the side where the excess fiber was cut. During the process, it was important to hold the coupon and the fiber still as the injected epoxy can potentially push the fiber out of the channel. Due to the thick viscosity of the epoxy, the process took several minutes as the epoxy needed to be ejected out of the syringe and traverse through the entire channel. Once the epoxy can be seen leaking out from the other end of the channel, the syringe was to be removed. As 353ND epoxy is a thermal epoxy, the combined fiber and coupon assembly was put on a heat plate at 150°C for 1 hour to complete its curing process. To summarize the embedding process:

<u>Stainless Steel 316 Coupon</u>

- Put into beaker filled with ethanol
- Ultrasonic cleaning for 1 hour

<u>Epoxy</u>

- Each part of the epoxy put into a separate beaker and stirred for minute
- Combine the two parts and stir for another minute
- Mixture pour into syringe

<u>Fiber</u>

- Mark along fiber where core of the fiber will be when put into the coupon
- Dip the sections that will be inside the coupon into ethanol to strip jacket for 5 minutes

<u>Assembly</u>

- Slide fiber into coupon until marked section
- Cut off excess fiber on one side
- Inject epoxy until it leaks onto other side
- Cure in 150°C for 1 hour to complete process

After the FBG was embedded inside the coupon via epoxy, the full assembly had to be set up so that the wavelength spectrum of the FBG can be read. The setup can be seen in Figure 3.5.

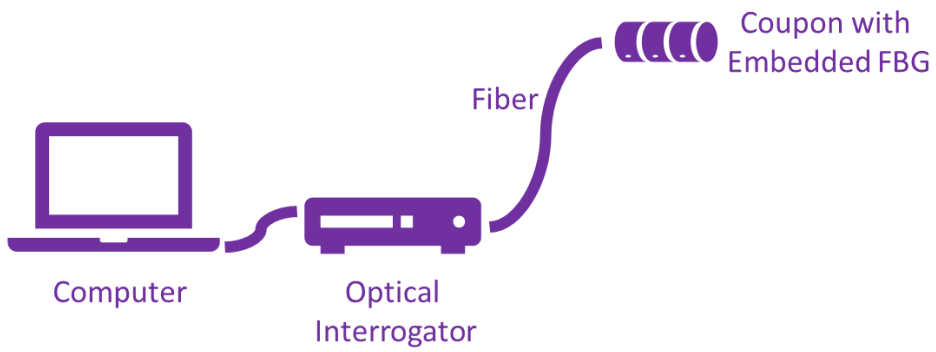

Figure 3.5 FBG Schematic

The fiber coming out from the coupon with the embedded FBG gets connected to an optical interrogator. The optical interrogator is a system that can monitor the FBG sensor in both static and dynamic settings. The interrogator has a wavelength swept optical source that shines light along the connected fiber. The spectrum data of the FBG is measured by detecting and processing the wavelength of light reflected back to the unit [91]. Optical interrogator used in the experiment was Micron Optics' HYPERION Optical Sensing Unit si155. This interrogator was preferred due to its flexible peak detecting algorithm. This allows the users to change the identified peak depending on the circumstances. When the sensors were subjected to various conditions, certain peaks disappeared or altered. The flexible peak detection allowed the appropriate/discernible peaks to be selected. The optical interrogator is also connected to a PC via an ethernet cable. The PC is installed with an ENLIGHT software that acts as an interface/control/adjustment for the optical interrogator.

3.3 Sensor Characterization

In this section, various tests were designed to understand characteristics of the sensor in various situations such as mechanical and thermal strain. Each subsection will discuss different testing scenarios and how it was designed. The three big scenarios explored in this research were: effects of tensile stress, effects of thermal stress, and effect of curvature of the channel on the FBG spectrum.

3.3.1 Tensile Test

Purpose of this test is to find the spectrum characteristics based on the stress applied on the coupon. With this knowledge, it can be used as a guideline for the wavelength readings in the future. For this part, tensile stress machine was to be used on the coupon with the embedded FBG. Tensile stress machine's output on the stress and strain value of the coupon was recorded. This value was to be compared to the

spectrum reading of the FBG which can be used to determine the characterization of the fiber. Neck of the coupon is the area of interest as it is the location where the FBG sensor is located and the neck would be the failure point during a tensile test.

For the tensile testing, it was again separated into multiple sections as three types of tensile loading scenarios were desired to be explored. First part involved determining the elastic limit of the FBG-Coupon assembly to determine what is the max stress limit appliable to the FBG sensor assembly before irreversible damage (plastic deformation) occurs. It is then followed by cyclic loading scenario and finally the failure test where the coupon was elongated until FBG signals were not able to be captured. The cyclic test and the failure test is what will be used to characterize the sensors.

When installing the coupon on the machine, it was important to carefully position the fiber attached so that it does not get tangled in any of the machinery or the clamps. The clamp was tightened until there was around 400N of tension applied to the coupon because of the tightening. It was important that there was no slippage during the testing as it will result in low quality stress-strain curve. Once the clamp has been sufficiently tightened, the machine was lowered to relieve the coupon from the ~400N force and calibrate it at 0N at the start of the test. The photo of the test setup and the schematic can be seen respectively in Figure 3.6 and Figure 3.7 respectively.

Figure 3.6 Tensile Coupon Test Setup

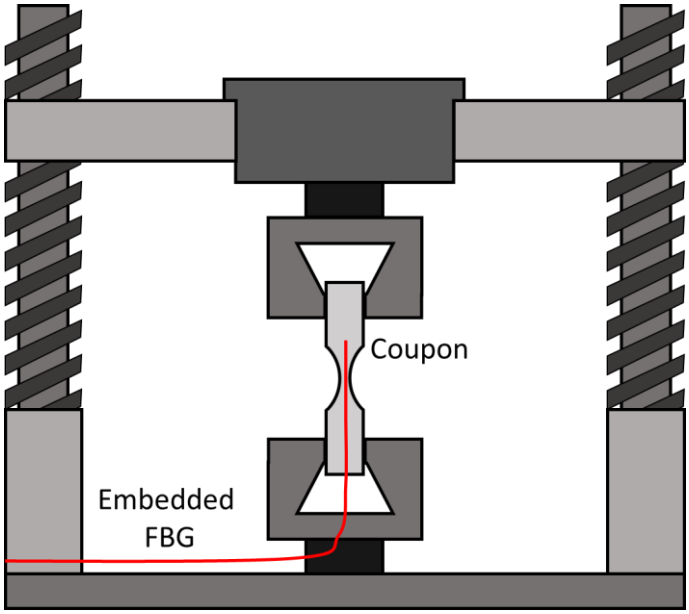

Figure 3.7 Tensile Test Set-up Schematic

3.3.1.1 Observation of Elastic Limits

The elastic limit for the coupon needed to be found so that the stress range for the succeeding tensile tests can be set up. As mentioned, the purpose is to determine what the max loading stress is before permanent damage occurs. This way, the testing can be done in a more controlled manner where unnecessary damage to the FBG-Coupon assembly can be avoided. For this test, the coupon is to be stretched until plastic deformation on the tensile stress machine. For all the tensile tests, the setup on the tensile machine was done in a constant fashion. Coupons were held at the edges with a vice grip and the rate of strain was set to be 0.675 mm/min as per corresponding ASTM standards for the dimensions of the coupon. For this test, as only the property of the coupon itself is of interest and not the fiber, the test was ran with only the coupon without any fiber embedded inside of it. After the coupon has been tightened and set up as seen in the previous figures, the tensile machine was set up to run at 0.675 mm/min until the coupon was broken.

Since various hole sizes were used for testing, the elastic limit for each hole size was to be found. It was hypothesized that parts with smaller hole sizes will have a higher elastic limit due to less material occupancy. The holes sizes tested were in Table 3.4 and its results can be seen in the results section

Table 3.4 Elastic Limit Test Samples

Channel Diameter	400 microns x3 samples	500 microns x3 samples	600 microns x3 samples	700 microns x3 samples

3.3.1.2 Cyclic Test

Low cyclic test in intervals of 5, 10, and 20 cycles were planned for this test to see if the reading for the wavelength will return to initial state after multiple cycles. This test is of interest as repeatability and lifecycle of the coupon and the FBG are of interest to understand to see the overall feasibility in implementing the technology in smart products. Also, it was hypothesized that due to the nature of the epoxy, some cyclic load may be required to calibrate it and make the spectrum reading reach an equilibrium as epoxy may stretch initially after it has been injected and cured inside the coupon [87]. The test was to range the strain of the coupon from 0 to 0.03 and back multiple times. This value was based on the established elastic limit of the coupon. The breakdown of the cyclic test can be seen in Table 3.5. After each test cycle, the coupon was examined to see if there were any visible damages to the coupon or the fiber. The tests initially start with lower cycle count to see if there are any impacts to the coupon at low cycles. Also, after each test iteration, the grip for the tensile machine was tightened again to have no slippage.

Table 3.5 Counts for Cyclic Test

Test Iteration	Cycles for Test	Accumulated Cycles
Test 1	5	5
Test 2	5	10
Test 3	10	20
Test 4	10	30
Test 5	10	40
Test 6	20	60
Test 7	20	80
Test 8	20	100
Test 9	20	120

3.3.1.3 Spectrum Analysis at Failure Point

For this test, the behaviour of FBG spectrum and wavelength shift at breakage point would be observed and analyzed. It is desirable to find out exactly at what point the FBG is no longer operational (at necking point, elastic point, UTS, etc.). As fiber can elongate much more than metal used for the coupons, it is suspected the fiber is operational even after the necking. FBG reading of the fiber was to be taken before fiber is embedded inside the channel, after embedding, and after curing. This information will help with

calibration of the FBG by acting as a design setup guideline. As a step further, being able to recognize the failure point based on patterns or indicators from the wavelength spectrum may provide useful for future applications. In this part, like the elastic limit test section, coupons embedded with FBGs would be stretched until breakage while the spectrum monitored for the entire duration at a rate of 0.675 mm/min.

3.3.2 Thermal Test

Main objective of this test is to look at the sensitivity of the FBG sensors in various temperature settings. With this test, the characteristics of the sensor can be seen at each temperature range and increments. This test would give a good understanding of the accuracy and behaviour of the FBG assembly. For initial characterization, the FBG embedded stainless steel coupon was subjected to various temperatures. FBG-Coupon assembly was placed on top of a controllable thermal plate – its schematic and picture can be seen in Figure 3.8 and Figure 3.9.

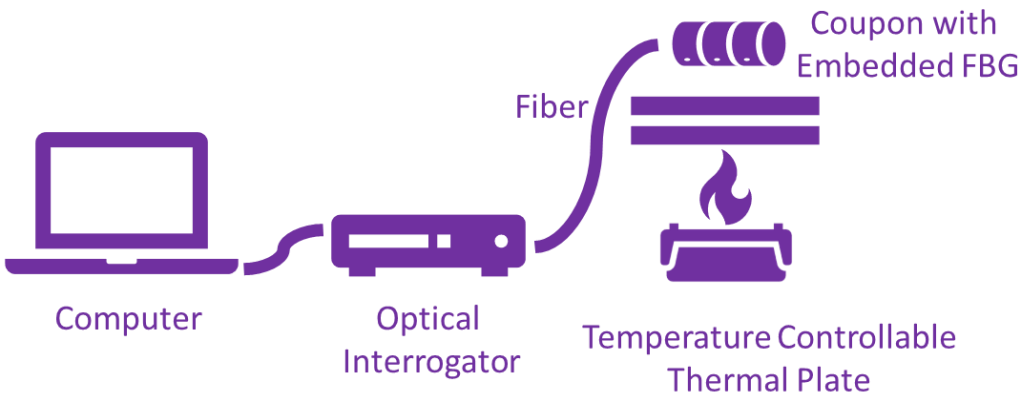

Figure 3.8 FBG-Coupon Thermal Testing Schematic

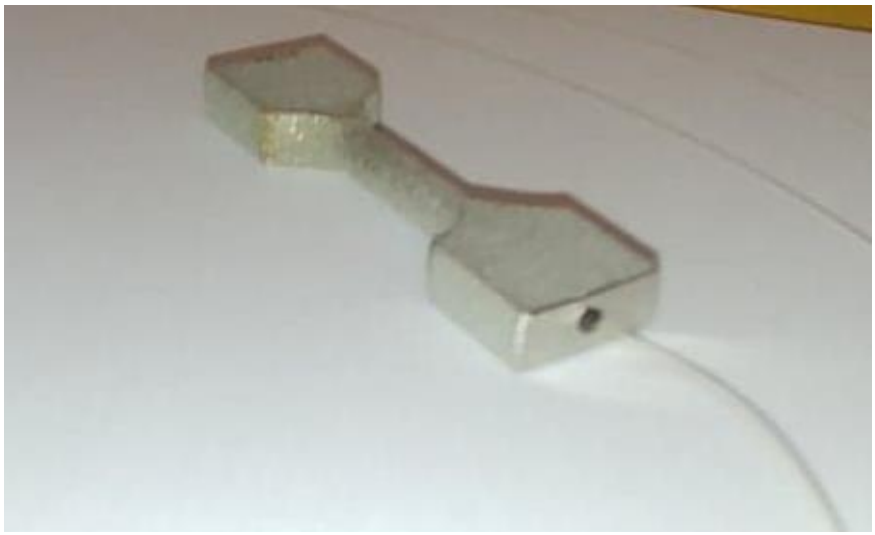

Figure 3.9 FBG-Coupon Assembly on Hotplate

For the test, the sample was left on a hotplate for a long enough duration so that the inside of the coupon is the same temperature as the surface to get the most accurate results for the experiment. The sample was heated to a certain temperature, held at the temperature for ten minutes, and temperature was raised again. The detailed procedure can be seen in Table 3.6. The temperature was held at each step for ten minutes to allow the readings to stabilize and come to an equilibrium. This is because it was thought that the epoxy at elevated temperature might relieve some residual stress inside the channel during the initial thermal testing. Also, the effect of residual stress may affect the overall accuracy of the reading; thus, it was important to find a way to potentially isolate or minimize the effect of an external perturbation when testing for thermal characteristics [15].

Table 3.6 Thermal Testing Steps

Steps	Description
Initial Condition	Coupon is at room temperature
Step 1	Heat coupon to 30°C at a constant rate of 300°C/hour (If overshoot happens, wait until temperature stabilizes before proceeding to next step)
Step 2	Hold coupon for 10 minutes at 30°C
Step 3	Heat coupon to 50°C at a constant rate of 300°C/hour
Step 4	Hold coupon for 10 minutes at 50°C
Step 5	Heat coupon to 70°C at a constant rate of 300°C/hour
Step 6	Hold coupon for 10 minutes at 70°C
Step 7	Heat coupon to 90°C at a constant rate of 300°C/hour
Step 8	Hold coupon for 10 minutes at 90°C
Step 9	Heat coupon to 110°C at a constant rate of 300°C/hour
Step 10	Hold coupon for 10 minutes at 110°C

Currently the limiting component for the test is the epoxy as the epoxy is not operational over temperatures of 300 degrees Celsius. For raw FBG, there is an increase of 10 picometers in wavelength per 1°C of temperature increased. It is of interest of see how this is affected due to the FBG now being embedded inside a stainless-steel coupon.

3.3.3 Curved Channels

When designing smart products, there will be instances where the designer cannot embed the FBG sensors along the direction of the stress. In many realistic scenarios, the gratings will be embedded in a curved fashion due to restrictions in the design geometry or the stress acting on the fiber may not be parallel to the fiber but instead be applied at an angle. It is of interest at how various curvature orientation affect the spectrum of the FBG and see if there is a limit where the spectrum gets deformed to a point that a reading cannot be reliably obtained for accurate measurements. One limitation the FBG has is that its readings gets less accurate the more misaligned fibers are to the direction of strain. The presence of curvature in FBG may bring some unwanted effects when looking at the resultant wavelength spectrum. Higher radius of curvature means that there will be less portion of the FBG that experiences stress parallel to the tension of the coupon. For smaller stress measurements, this is can be detrimental as an accurate determination of the shifted wavelength will be harder to detect. Thus, it is hypothesized that the greater the curvature of the FBG, there will be a decrease in the resolution.

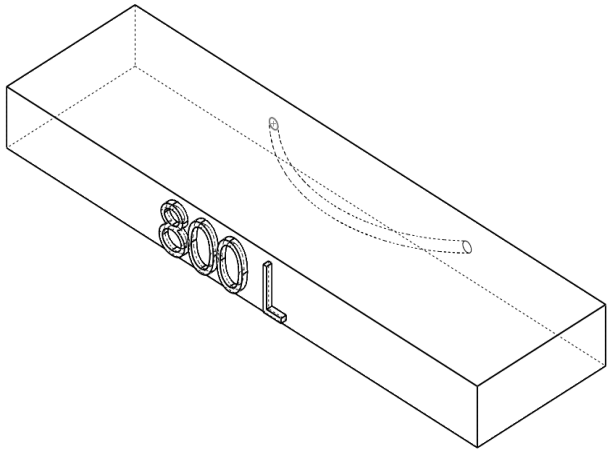

Figure 3.10 Rectangular Coupon with Curved Channel

For this test, curved channels were to be created inside of rectangular test coupons to embed the fiber. The design of the coupon can be seen in Figure 3.10. The coupons will vary regarding the diameter of the channel and the radius of the curvature for the channels. It was thought that the biggest challenge for this experiment would be the fabrication of the curved coupons with a channel big enough to accommodate for the fiber while still small enough that the fiber can be embedded securely with the epoxy. Even with the utilization of AM and LPBF, creation of such small channels in a curved orientation was thought to be challenging. With the optimization parameters obtained prior, the coupon was to be printed in the orientation as seen in Figure 3.11. This printing orientation was chosen as it minimizes the overhang steepness throughout the channel during the fabrication. Less steep overhangs that are below 45 degrees is ideal to create a part with such channel design.

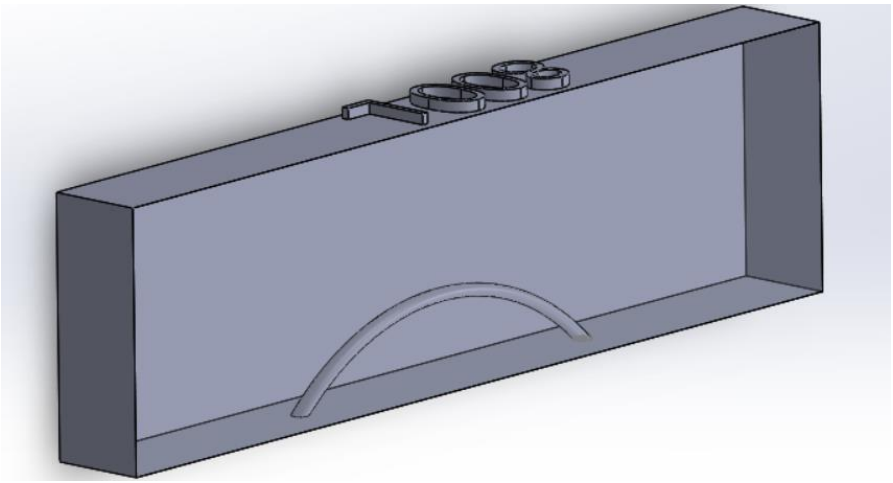

Figure 3.11 Rectangular Coupon Printing Orientation

The sample geometry and parameters can be seen in Figure 3.12. The length of the grating section in the fiber is 10mm. Longer the channel is, it is more likely that there will be defects in the channel when printing it. The portion of the length where the gratings are should ideally be kept away from the edge of the coupon by at least 1mm. Accounting for these factors, the arc length of the channel were all kept at a constant length of 20mm. The FBGs was to be inserted via side of the coupon at an angle to prevent problems from overhanging during the printing process. The hole size at the entrance can be bigger as most of the stress will be experienced by the portion of the FBG along the narrow part of the coupon.

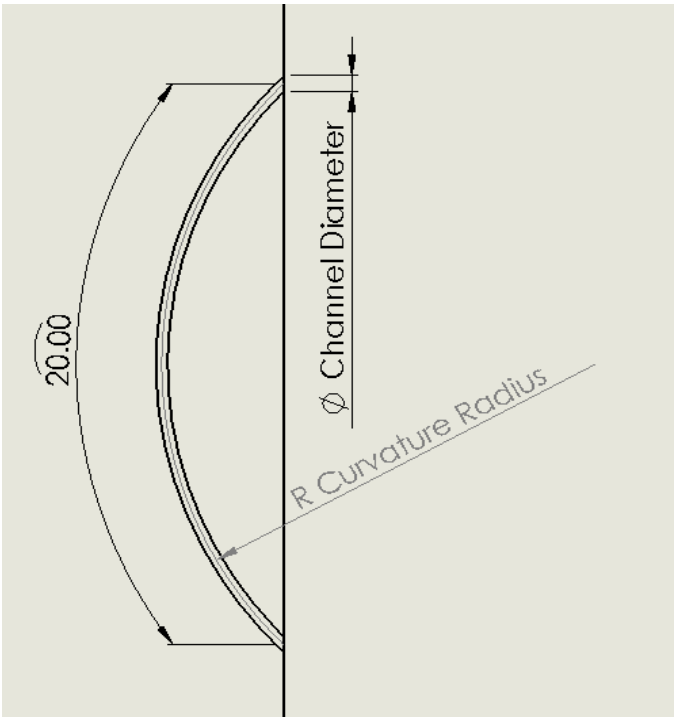

Figure 3.12 Curvature Geometry

A total of 3 curvature radius values were to be tested. Each curvature radius also has variations in channel diameter; thus, a total of 9 types of coupons were printed as seen in Table 3.7.

Table 3.7 Coupon Configuration Combinations for Curvature Test

Curvature Radius								
7mm			10mm			13mm		
Channel Diameter (Microns)			**Channel Diameter (Microns)**			**Channel Diameter (Microns)**		
600	700	800	600	700	800	600	700	800

With the successfully printed coupons, the assemblies were to be connected to the optical interrogator to get the corresponding wavelength spectrums and the spectrums were to be characterized. Finally, the stress and temperature test from the previous sections with the straight channels were to be replicated with the curved channels to model and observe their behaviour based on its curvature. It was hypothesized that the sensors themselves would not be as efficient when they are tilted from the angle of the stress. This is thought due to the difference in the distribution of strain along the gauge length of the sensor.

3.4 Simulation Model

Due to the developments of COVID-19 during the testing phase, further fabrication and in-person testing of the curved coupons proved to be challenging to complete within the timeline of this project. As a substitute, CMC's COMSOL simulation software was chosen as an alternative method to see how the FBG embedded in a coupon would behave under varying channel radius. COMSOL is a powerful Multiphysics software that is utilized for finite element analysis. It is commonly used to simulate systems in areas of mechanical, electrical, and fluid dynamics. With COMSOL it is possible to replicate the FBG sensors within the simulation.

The model was set up as a 2D model as the main interest was to see how the spectrum changes depending on the curvature of the channel - which only varies in a 2D setting. There were two physics studies used for this simulation: solid mechanics for stress and strain of the FBG-Coupon assembly and electromagnetic frequency domain study for modelling the reflection of the Bragg wavelength. Four main components of the FBG-Coupon assembly was simulated: stainless steel coupon, fiber cladding, fiber core, and core grating. The geometry of the 4 main components was built in COMSOL where the core was first generated with the grating generated in a periodic fashion. The cladding encased the core with the coupon encompassing the entire build. Example of the setup can be seen in Figure 3.13 and Figure 3.14.

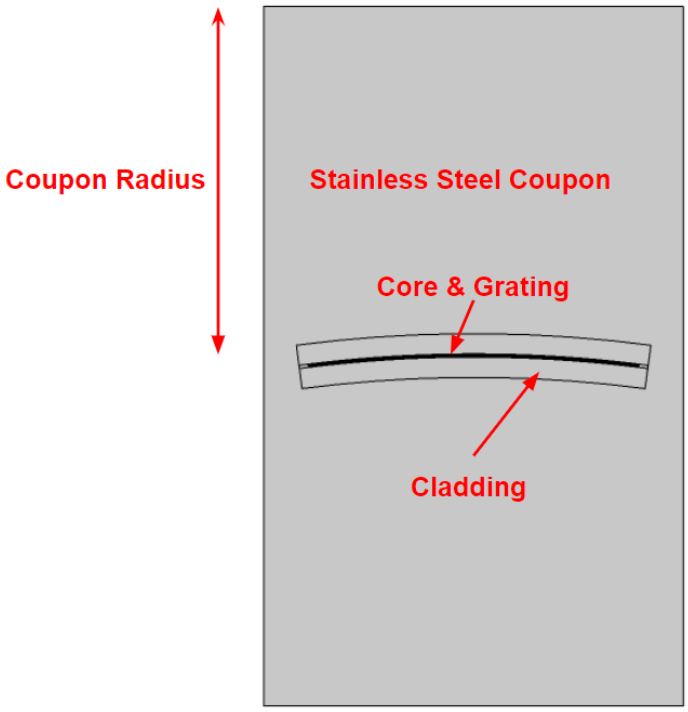

Figure 3.13 COMSOL FBG Assembly Setup

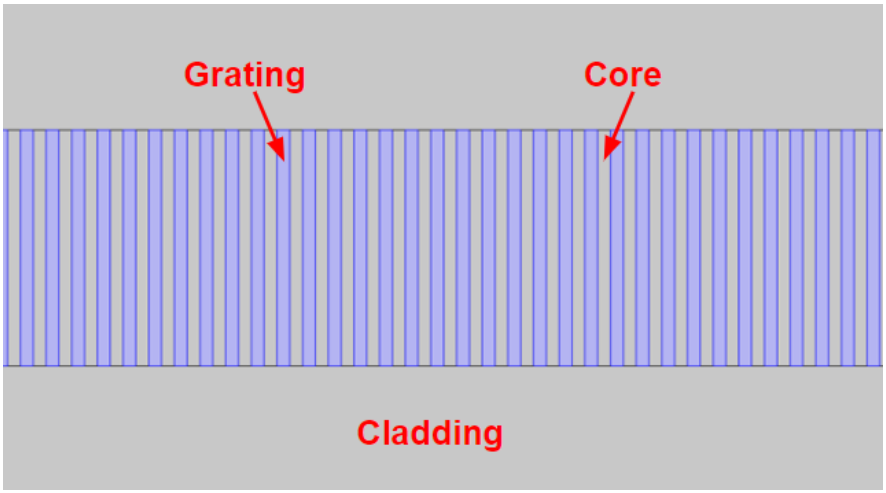

Figure 3.14 COMSOL FBG Assembly Setup Zoomed

The key variables for the simulations can be seen in Table 3.8. For this simulation, the angle of curvature and coupon radius will be varied to see how it affects the reflection spectrum. All other variables were controlled and kept constant throughout the tests. It was of interest to see how the curvature of the fiber inside the coupon affects the reading when constant axial tensile stress is applied on the stainless steel coupons. Fiber was embedded at various angles from 0° (straight fiber) to 90°. Curvature angle θ's geometry can be seen in Figure 3.15. The length of the FBG-Coupon assembly was

limited by the processing power of the computer used to run COMSOL as longer fiber meant a longer computational time. To make the simulation time feasible, the arc length of the fiber was chosen to be 1 mm for all the fiber orientation angles. The spectrum was expected to get more accurate as more gratings were used. This is because the reflection of the peak wavelength becomes more apparent as grating count increases. For such reasons, majority of the fiber core section contained gratings to increase the accuracy of the simulation.

Table 3.8 COMSOL Simulation Variables

Variable	Value
Arc length of the fiber	1000 μm
Angle of curvature (Test Variable 1)	0° $(straight)$, 15°, 30°, 45°, 90°,
Cladding index of refraction	1.546
Core index of refraction	1.554
Grating index of refraction	1.56
Grating Thickness	0.50 μm
Core Radius	4.5 μm
Cladding Radius	65 μm
Stainless Steel Radius (Test Variable 2)	1mm, 2mm, 3mm
Grating Period	0.50 μm
Effective index of refraction	1.554
Max mesh size for core & grating	0.28 μm
Max mesh size for cladding	1.1 μm
Min mesh size for all parts	0.0375 μm
Wavelength spectrum range	1.554 μm ~ 1.556 μm (in intervals of 0.02 nm)

For the solid mechanics part of the simulation, the stress applied on the simulated coupon was to be the value of the elastic stress limit determined from the earlier section at 140 MPa. The radius of the stainless steel coupon was altered to see how the thickness of the host material affects the stress translation to the fiber. As stress applied will be constant at 140 MPa, higher radius coupons will experience overall less force and strain compared to the coupons with lower radius values. The stress was applied evenly on one side of the coupon with the opposite side being fixed to subject the coupon under tension.

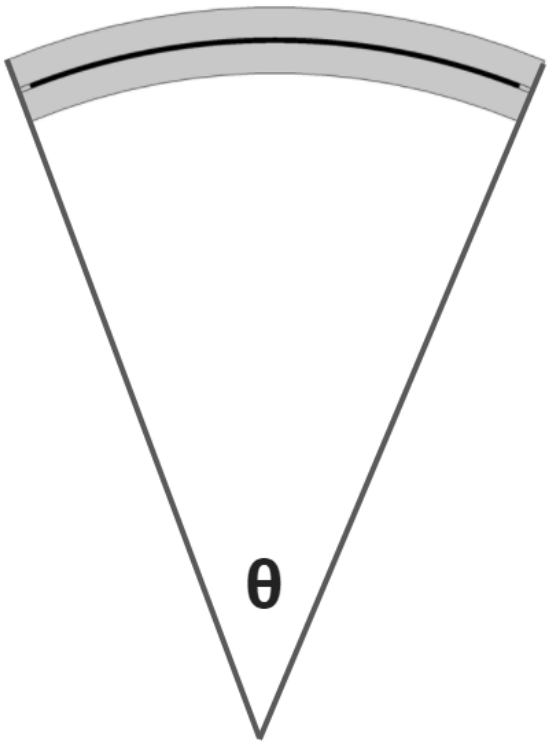

Figure 3.15 Curvature Angle of Fiber

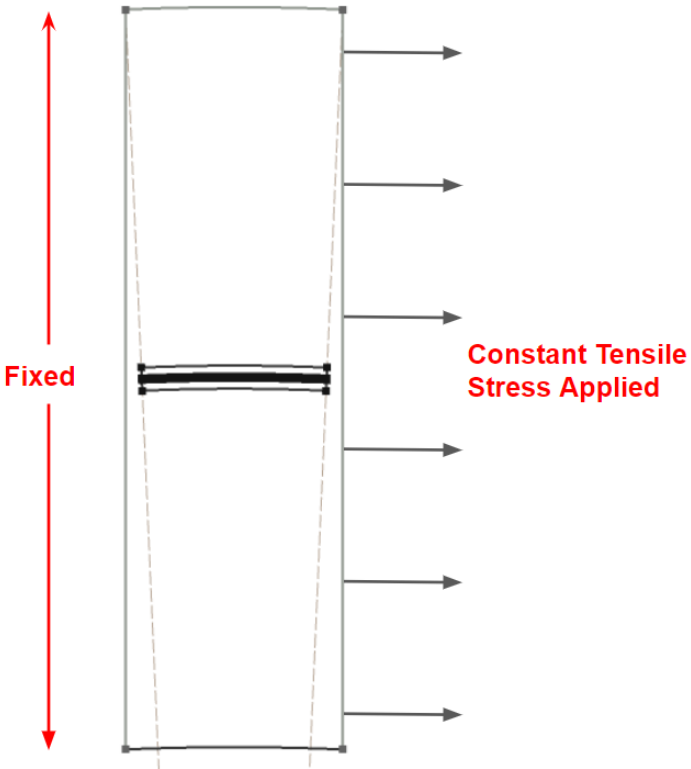

Figure 3.16 Stress Loading on the Coupon

Table 3.9 All Simulation Configuration Combinations

Curvature Angle (°)														
0			15			30			45			90		
Coupon Radius (mm)			**Coupon Radius (mm)**			**Coupon Radius (mm)**			**Coupon Radius (mm)**			**Coupon Radius (mm)**		
1	2	3	1	2	3	1	2	3	1	2	3	1	2	3

To setup the physics for the electromagnetic wave to find the Bragg wavelength, boundary mode analysis was conducted at the point of entry and exit for light along the core of the fiber. The boundary mode analysis was utilized to find the propagation constant for the range of wavelength observed for this study. The wavelength range was as seen in Table 3.8 and it was based off of Bragg's law and the index of refraction of the grating, core, and cladding. The frequency domain study step on COMSOL was utilized to find the data points for the reflection spectrum. The peak of the reflection spectrum would be the value that is observed and recorded. Port location were set up at both ends of the fiber core as seen in Figure 3.17.

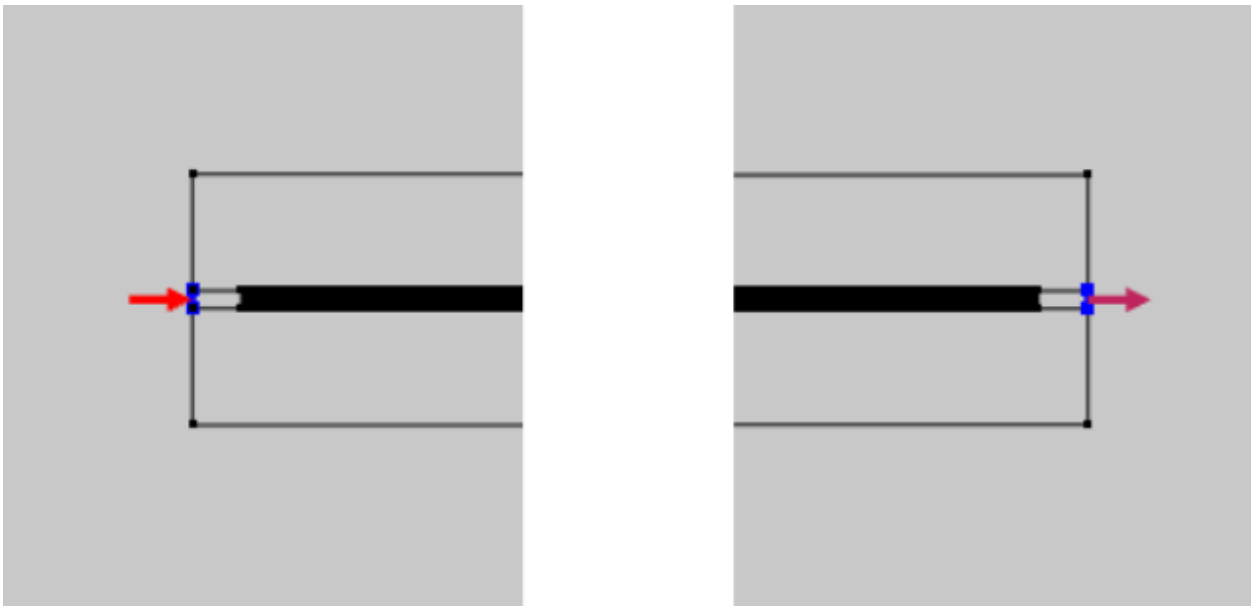

Figure 3.17 Entry Port and Exit Port Locations

Proper meshing is crucial in determining the outcome/accuracy of the simulation as meshing cuts up the geometrical design of the part into numerous elements when finding a solution. These small, fine elements are used to calculate local approximations of the whole geometry and eventually pieced together to solve for the entire geometry. As a result, the parameters of the meshing determines the overall speed

and accuracy of the simulation. Generally, the more elements the mesh has, the higher its accuracy, but lower the simulation speed. Due to time constraints and memory limitations of the computer used to run the simulation, it was crucial to determine mesh parameters that can provide accurate results to derive conclusions from but still fast enough to run the simulation in a realistic time. The values of index of refraction of the three components vary more than they would be for standard FBG sensors. This is because if the index of refraction sizes are too close, the simulation does not reflect the light properly. If the index of refraction values are too similar, some parts of the initial light beam seeps out of the core into the cladding, leading to less accurate results. The maximum mesh sizes were determined so that they would be a fraction of the wavelength. It was thought that by having mesh sizes be smaller than the wavelength of the incoming light, the results would still accurately graph the reflection spectrum. For such results, the largest mesh value of the core and grating was set to be 0.28 microns and the largest mesh value of the cladding and coupon was set to be 1.1 microns. The core was made to be more accurate and computation intensive than the cladding as most of the light reflection and activity occurs in the core. Smallest mesh sizes for all the components were 0.0375 microns as used by the 'finer' setting for meshing in COMSOL. The meshing used can be seen in Figure 3.18. With all the physics and mesh setup, the COMSOL simulation was conducted to understand the spectrum behaviour for the various test variables.

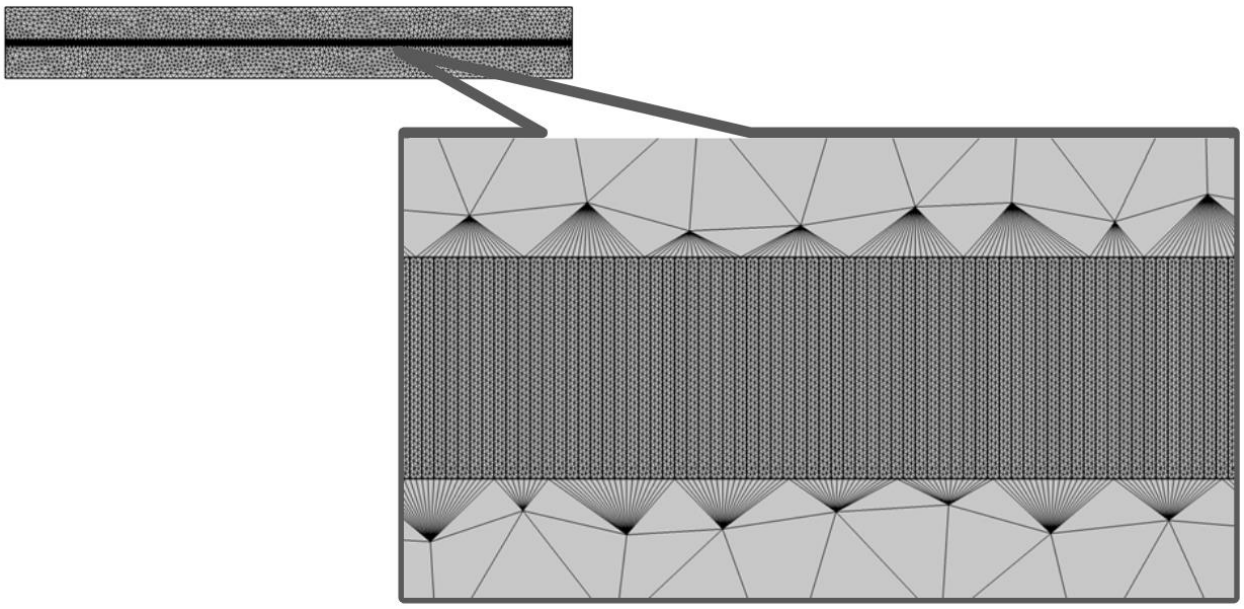

Figure 3.18 COMSOL Mesh Generation of Core and Cladding

Chapter 4
Results and Discussions

4.1 Coupon Fabrication Results

For the first batch of the printed coupons, the default machine parameters for the AM 400 machine were utilized. Its results of channel clearance for various channel diameters can be seen in Table 4.1. Channel diameter size of 600 microns and below were not able to achieve full clearance. Some post-processing was done to see if it would be able to clear a hole for the channels with blockage. Ultrasonic bathing was conducted for two hours by submerging the coupons in ethanol solution and the channel was blown with compressed air afterwards. However, the effects were subpar as only one 700 micron coupon showed any difference after the post-processing.

Table 4.1 First Channel Diameter Printability Test

Hole Diameter (Microns)	400	500	600	700	800
Number of Samples with Full Channel Clearance	0/3	0/3	0/3	1/3	3/3
Number of Samples with Full Channel Clearance After Post Processing	0/3	0/3	0/3	2/3	3/3

As the 400 micron variation had the smallest channel size, it was the first sample to use computed tomography (CT) scan to examine the channel clearance. The severity of the blockage and the shape of the channel was desired to be examined to understand what parameters required to be altered. It can be seen from Figure 4.1 that the channel was not completely cleared throughout and has a lot of blockages throughout its length. The blockages are hypothesized to have been caused by the formation of meltpools along the inside surface of the channel during the fabrication.

Figure 4.1 CT Scan of 400 Micron Channel in Tensile Coupons

From the CT scan, various cross-section layers were observed to see if there were any shrinkage or expansion that made the size of the channel be greater or less than 400 microns. Two of the layers can be seen as an example in Figure 4.2. It was found that the channels formation from the various layers are all around 400 microns in diameter, meaning that the printing yielded an accurate dimension for the channel diameter size.

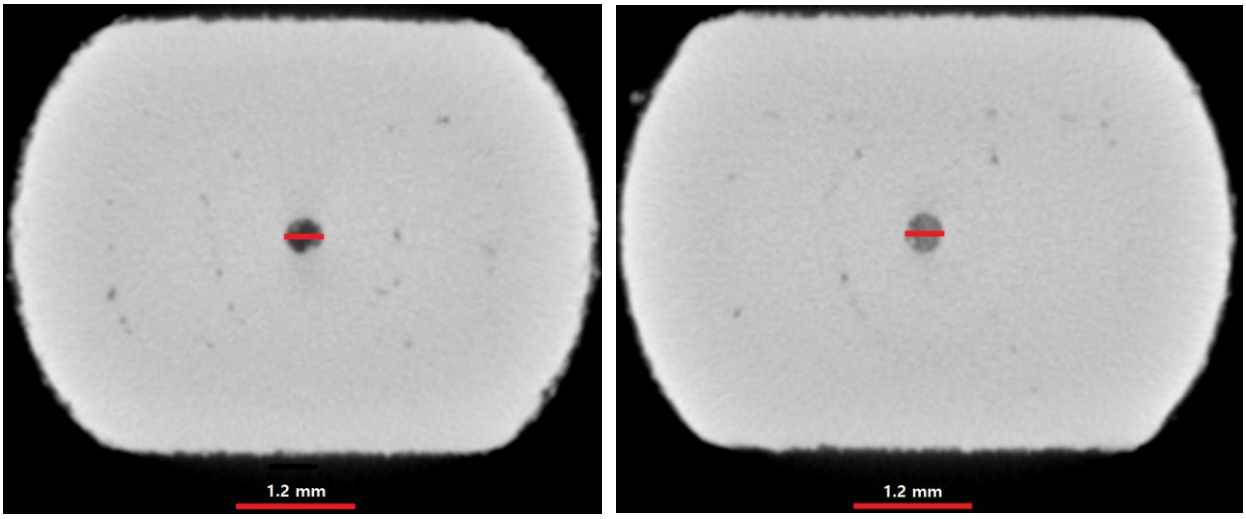

Figure 4.2 CT Scan 400 Micron Cross Sections at 1/3rd of coupon length (left) and 2/3rd of coupon length (right).

Although the channel was not formed perfectly circular, there was no shrinkage or expansion observed throughout the channel. For the next iteration of the design, the hatch offset parameter was given more attention to as it affects the porosity and the surface quality of the channel walls. Along with hatch offset, laser power and printing orientation was altered. This iteration also involved altered laser parameters by varying the laser power to be +/- 30% of the initial laser power. The results of the lower laser power at 133W, higher laser power of at 247W, and horizontal printing orientation at 190W can be seen in Figure 4.3. Horizontal printing orientation was utilized to see what effects the orientation would have on the printing quality of the inside channels.

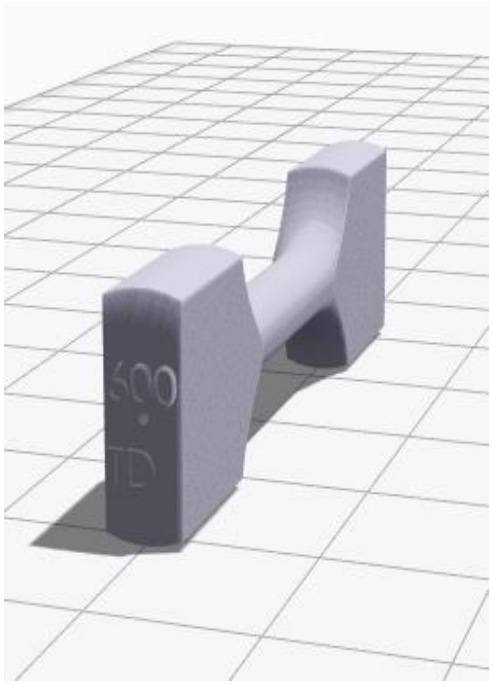

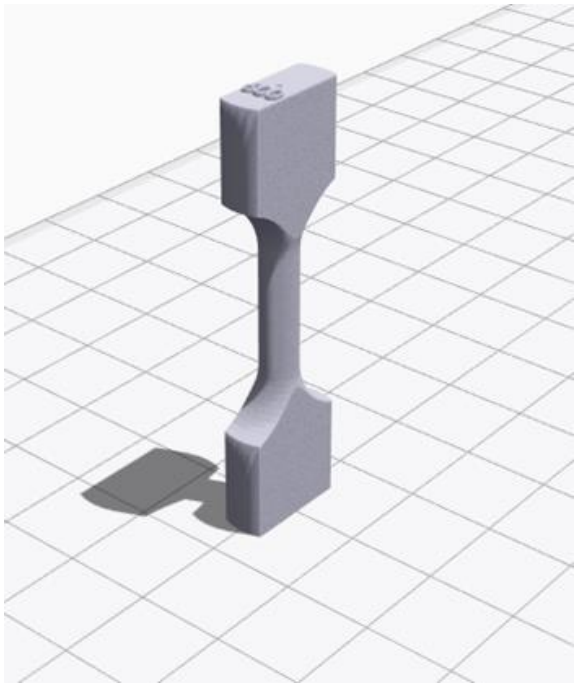

Figure 4.3 Horizontal Printing Orientation

Figure 4.4 Vertical Printing Orientation

The lower and higher laser power coupons were printed vertically just like in the first testing as seen in Figure 4.4. The successful and failed coupon count for the varying laser power and horizontal printing orientation can be seen in the following tables.

Table 4.2 Second Channel Diameter Printability Test - Low Laser Power

Low Laser Power (133W)			
Hole Diameter Size (Microns)	400	500	600
Number of Samples with Full Channel Clearance	0/3	3/3	3/3
Number of Samples with Full Channel Clearance After Post Processing	0/3	3/3	3/3

Table 4.3 Second Channel Diameter Printability Test - High Laser Power

High Laser Power (247W)			
Hole Diameter Size (Microns)	400	500	600
Number of Samples with Full Channel Clearance	0/3	3/3	3/3
Number of Samples with Full Channel Clearance After Post Processing	0/3	3/3	3/3

Table 4.4 Second Channel Diameter Printability Test - Horizontal Orientation

Horizontal Print Orientation			
Hole Diameter Size (Microns)	400	500	600
Number of Samples with Full Channel Clearance	0/3	0/3	3/3
Number of Samples with Full Channel Clearance After Post Processing	0/3	1/3	3/3

The horizontal printing orientation and high-power lasers did not yield optimal results. For the ideal creation of channels, coupons had to be printed upright. This was hypothesized as for the horizontal printing orientation, the temperature of the melt pool caused by the laser would warp the topside of the channel, giving lower accuracy for the overall formation of the channel [92]. From these results, it was determined that the coupons were to be printed at a 30% laser power reduction at 133W. Further iterations with altered hatch offset parameters was attempted; however, 400 micron hole diameter was still unable to be achieved, thus; channel diameter of 500 micron was determined to be the smallest channel diameter achievable. Final printing parameter for the AM 400 machine can be seen below

Table 4.5 Optimal Coupon Parameters for 316 Stainless Steel Coupons

Parameters	Value
Laser Power	133 W
Volume Hatch Distance	0.110 Microns
Volume Hatch Offset	-0.100 Microns
Volume Fill Contour Distance	0.124 Microns
Volume Fill Contour Offset	0.050 Microns
Volume Border Distance	0.100 Microns
Downskin Hatch Offset	0.025 Microns
Downskin Hatch Distance	0.060 Microns
Upskin Hatch Offset	-0.060 Microns
Upskin Hatch Distance	0.11 Microns
Upskin Border Offset	-0.06 Microns

The final coupons printed on the AM400 machine can be seen in Figure 4.5. The resultant coupons were consistant from one another in their dimensions and porosity. These coupons were to be used for the tensile and temperature tests.

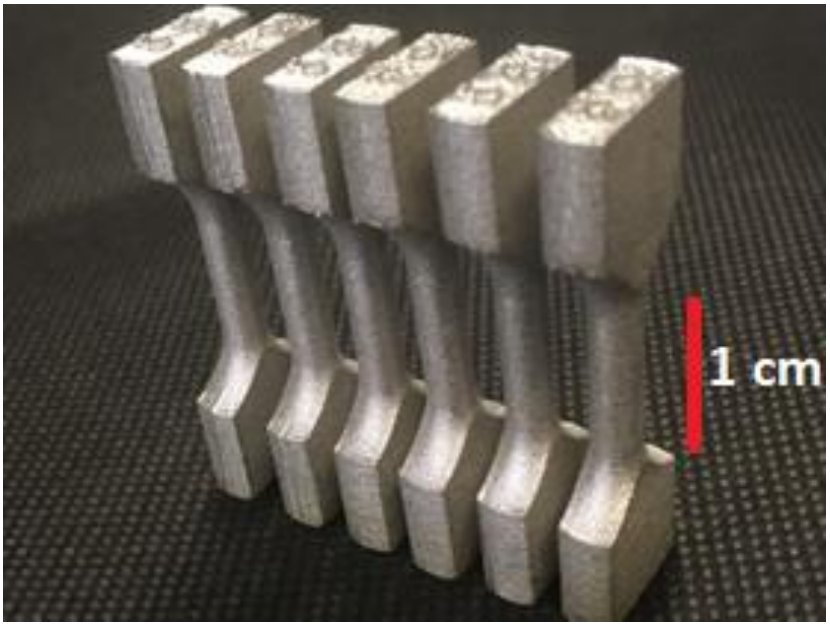

Figure 4.5 Successfully Printed Coupons

A coupon with a 500 micron channel diameter that was fabricated with the optimized parameter was once again observed via a CT scan and it can be seen in Figure 4.6 that the channel is much more clean compared to the previous CT scan of 400 microns.

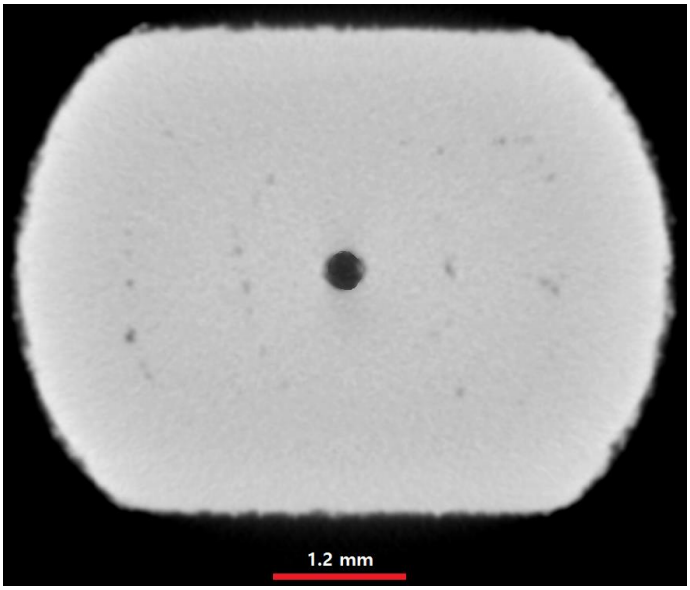

Figure 4.6 CT Scan 500 Micron Cross Section with Optimized Parameters

4.2 Sensor Embedding Results

Since the ideal coupon has been generated, the fiber was then to be embedded inside of the coupon. 353ND Optical Epoxy by Paisley was chosen as the bonding mechanism as discussed prior. Although the optimal coupon channel diameter of 500 micron was determined from the previous section, it was found out that due to the thick viscosity of the epoxy, a larger channel diameter was required. This is because if not enough room is allocated for the epoxy, it would cause internal strain and even potentially damage the FBG when the epoxy thermally cures and expands [87][90]. The fiber was slid into the coupon and the epoxy was injected via a syringe as discussed in the procedure section.

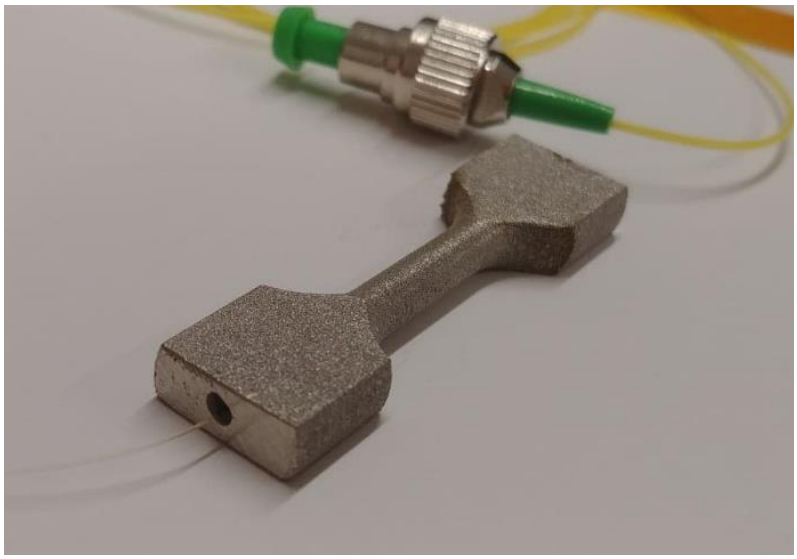

Figure 4.7 Coupon with Embedded FBG Sensor

It can be seen in Figure 4.7 of the embedded coupon which was successful. The fiber sticks out the bottom of the coupon and the black residue is from the cured epoxy. Figure 4.8 shows the spectrum right after the coupon was cured at 150 ^{o}C for one hour. Its distinct peak can be located and monitored.

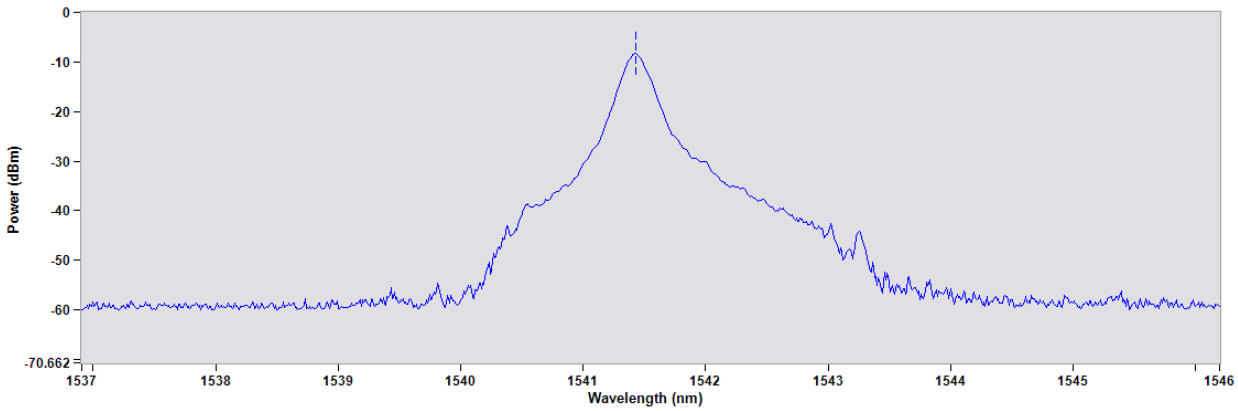

Figure 4.8 FBG Spectrum Just After Curing Process

However, the spectrum broadened and shifted lower after a day as seen in Figure 4.9. This was thought to occur due to the cooling of the coupon and the effects of residual stress from the cured epoxy.

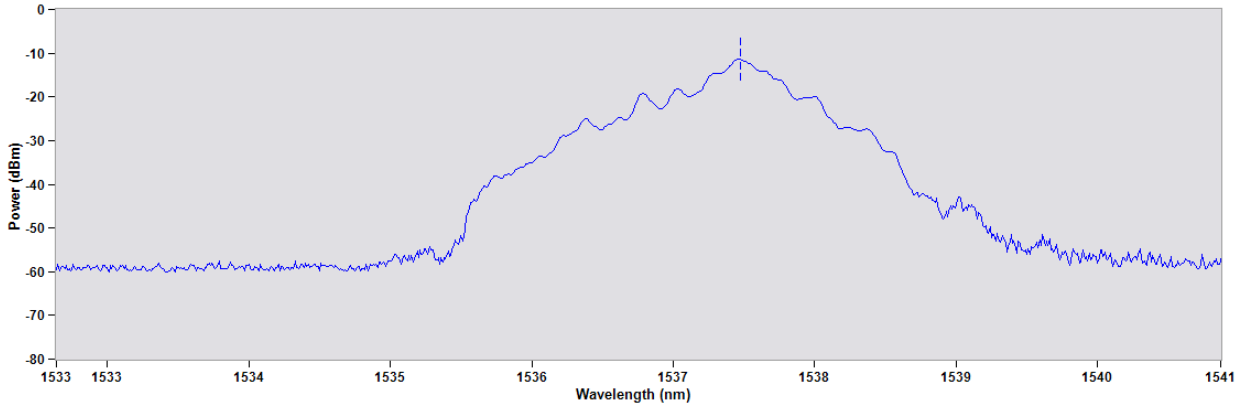

Figure 4.9 FBG Spectrum Day After Curing Process

This degree of alteration was deemed acceptable as the distinct peak was still identifiable. For the sake of research's interest, peak identification is the only requirement needed to determine the tensile and thermal stress change.

4.3 Sensor Characterization Results

4.3.1 Elastic Limit Test Results

The results from the elastic limit test was graphed on a stress-strain curve as seen in Figure 4.10 for the 400 micron variation. Even though a 400 micron channel diameter was not able to be fabricated, it was of interest to see what its elastic limit wold be as a comparison to other coupons with different channel diameters. The zoomed in version of the graph along with the 500, 600 micron variations can be seen in Figure 4.11, Figure 4.12, and Figure 4.13. For all three channel variations, the stress-strain relationship is linear until around 0.1%. Although up until 0.2% could potentially be classified as part of the elastic limit, a more conservative value was utilized as it could affect the cyclic test.

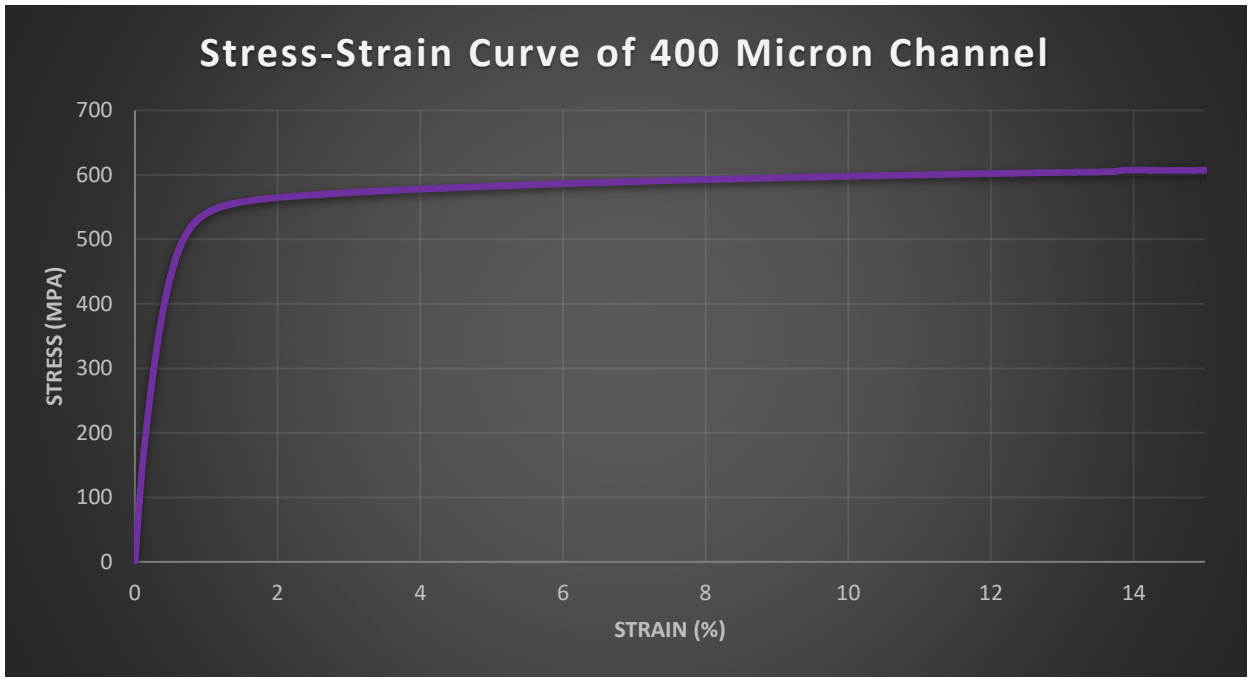

Figure 4.10 Stress-Strain Curve of 400-Micron Coupon

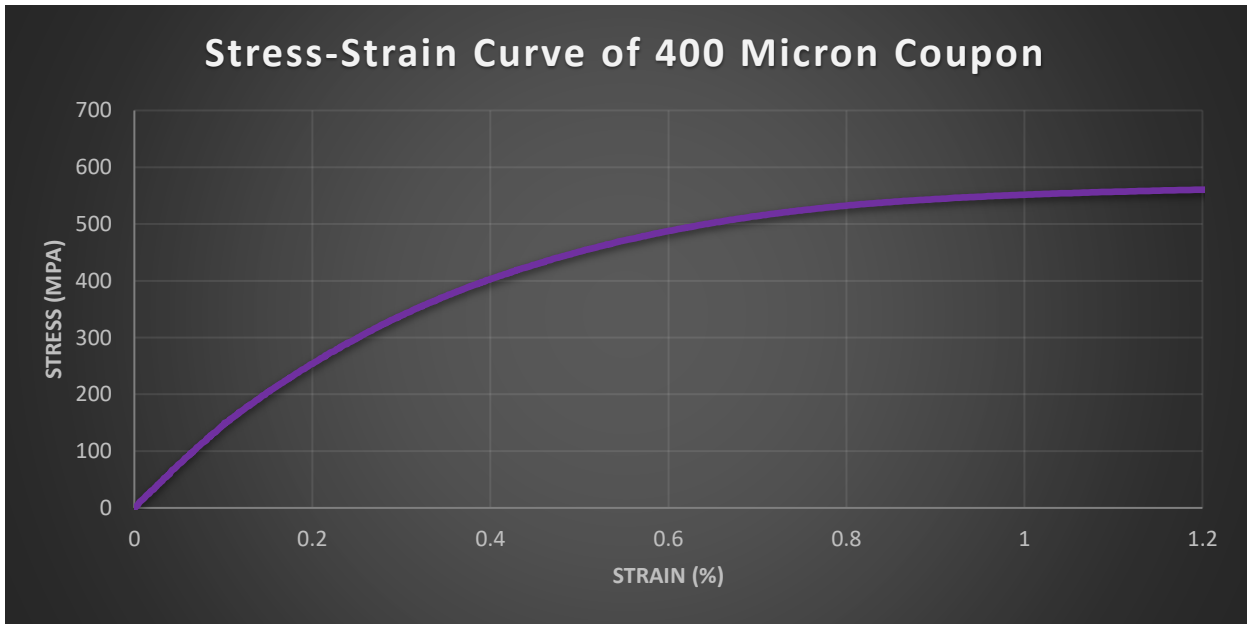

Figure 4.11 Stress-Strain Curve of 400 Micron Coupon Zoomed in

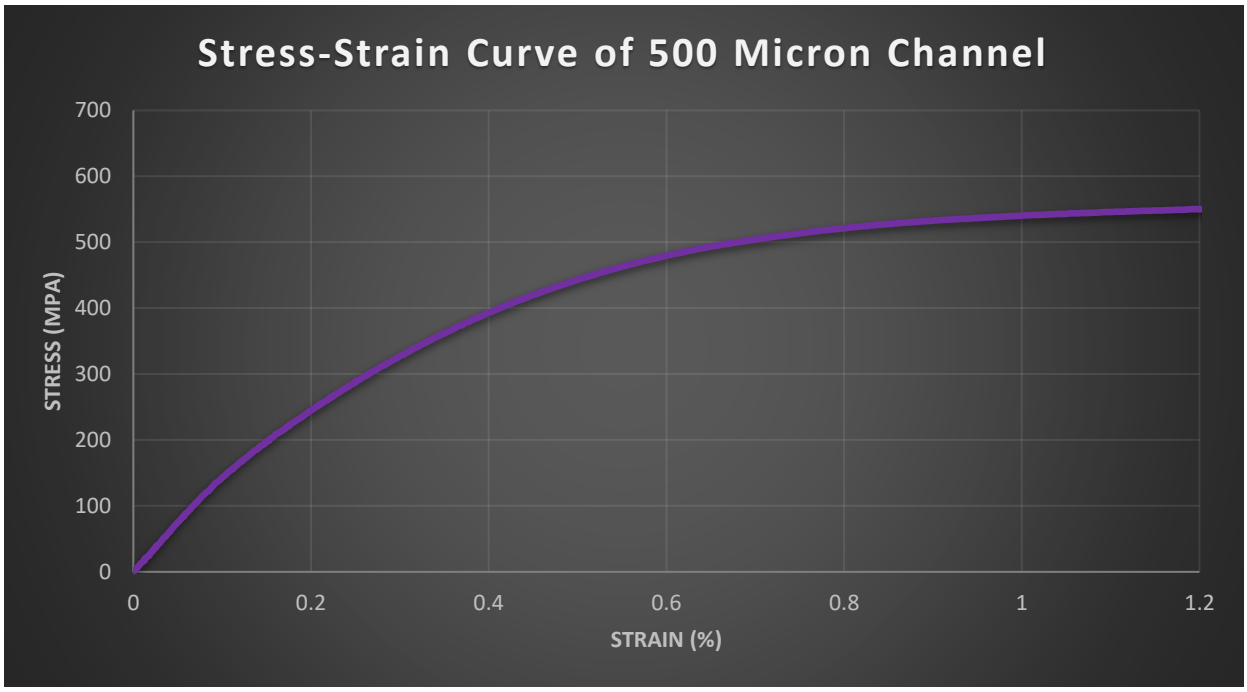

Figure 4.12 Stress-Strain Curve of 500 Micron Coupon Zoomed in

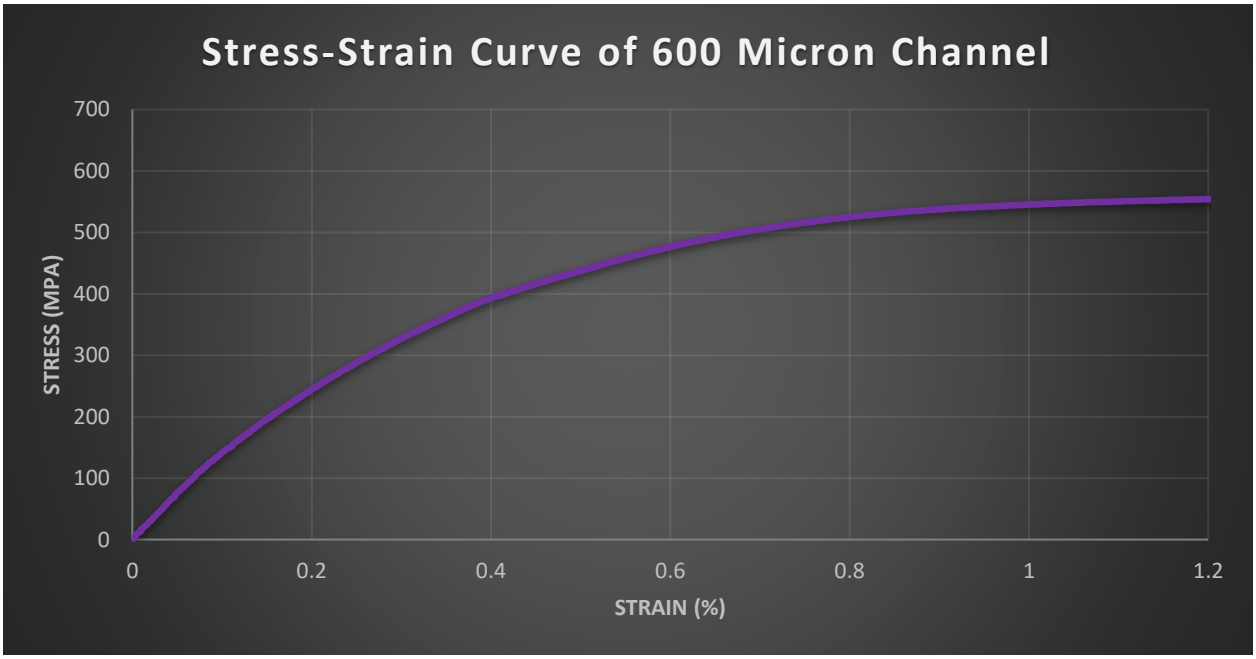

Figure 4.13 Stress-Strain Curve of 600 Micron Coupon Zoomed in

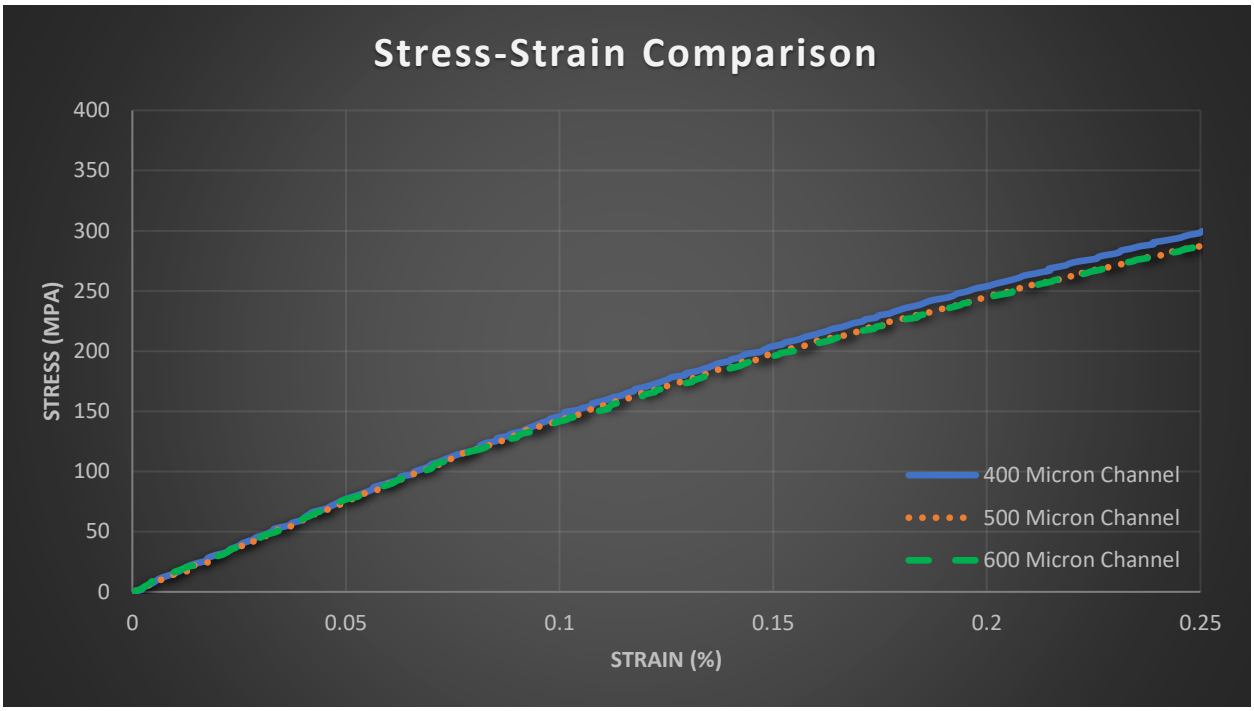

Figure 4.14 Elastic Limit Comparison

For this research, the proportional limit was utilized as the elastic limit with the premise that proportional limit occurs at 0.1% strain, the elastic limit stress results of the test for the various channel sizes can be seen in Table 4.6. The 700-micron elastic limit was unable to be found as the samples were printed with different printing parameters compared to the other channel sizes and would yield an uneven testing condition. The difference in the elastic limit values were miniscule for the 3 different channel sizes. This was expected as the variance in channel diameter is too small to see significant changes in the elastic limit. However, despite the minuscule changes, the coupons with smaller channels required higher stress values for equivalent strain. There was more distinction in the graphs after the elastic limit, where the 400 micron channel variation having the higher stress value. The characteristic can be explained by the more abundant materials in the smaller channel diameter variation. The smaller diameter means that there is less material missing in the core compared the coupons with a larger channel. Excess material in the lower diameter variation would require higher stress values to achieve equivalent strain.

Table 4.6 Elastic Limit for Coupons

Elastic Limit Test Results				
Channel Diameter (Microns)	400	500	600	700
Elastic Limit (MPa)	145.89	142.73	141.52	N/A

4.3.2 Cyclic and Breakage Test Results

Although the elastic limit determined from the previous section was 0.1%, 0.03% was chosen for the tensile test to be cautious about any to the components. The sensitivity of the FBG sensors would have no problems detecting strain of 0.03%. After the successful embedding of the fibers into the coupons, two more FBG-Coupon assemblies have been produced. Thus, a total of 3 assemblies were put under cyclic loading for analysis. The loading was limited to the elastic limit so that the coupon would only operate in the elastic strain region and not deform permanently. It was found that the FBG readings gave a constant periodic readings with uniform amplitude during cyclic tensile loading as seen in Figure 4.15, Figure 4.16, and Figure 4.17. For each cycle, the readings would always start at a constant wavelength and reach the same peaks.

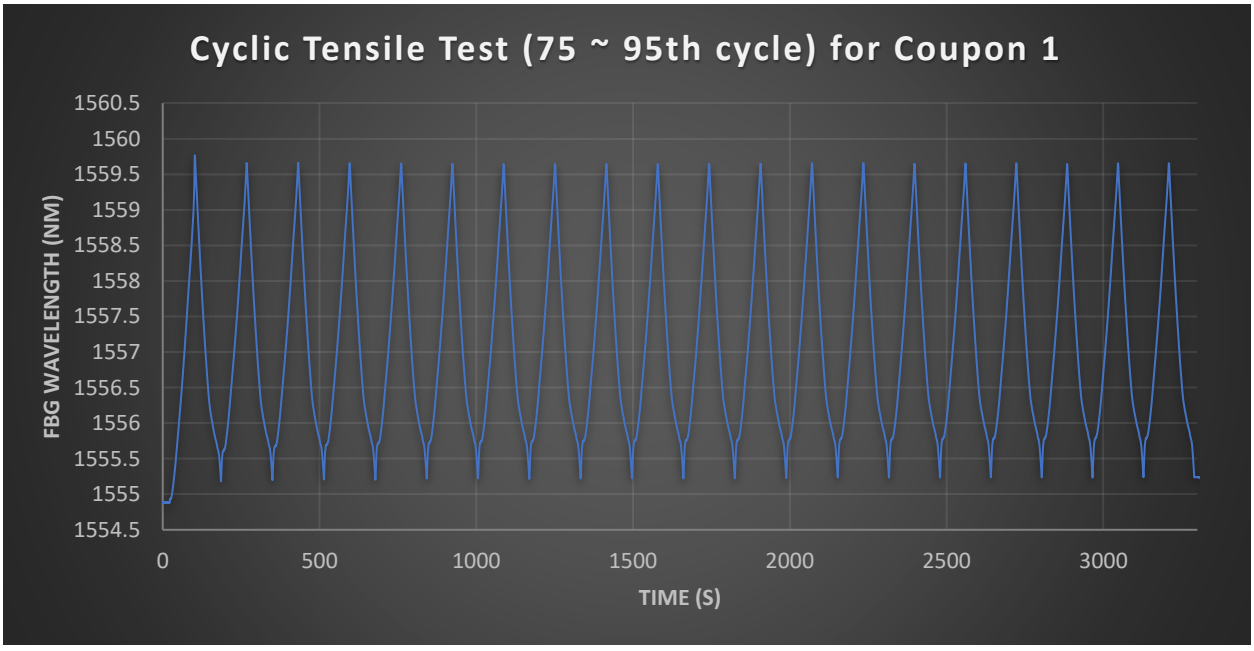

Figure 4.15 Cyclic Tensile Test for Coupon 1

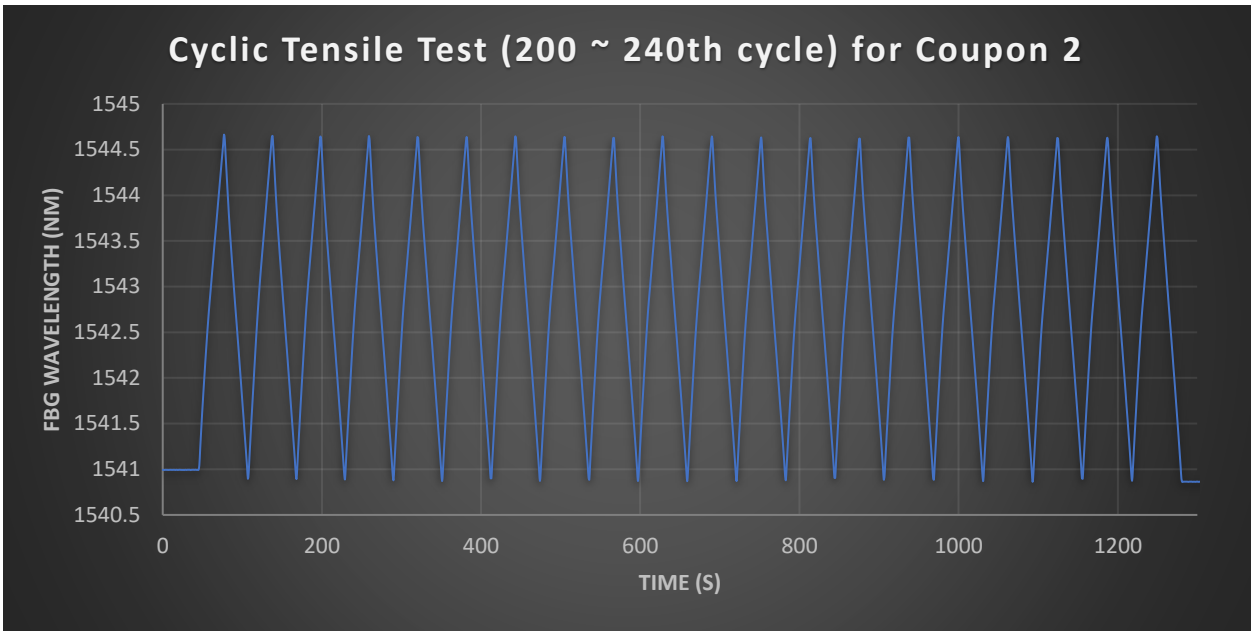

Figure 4.16 Cyclic Tensile Test for Coupon 2

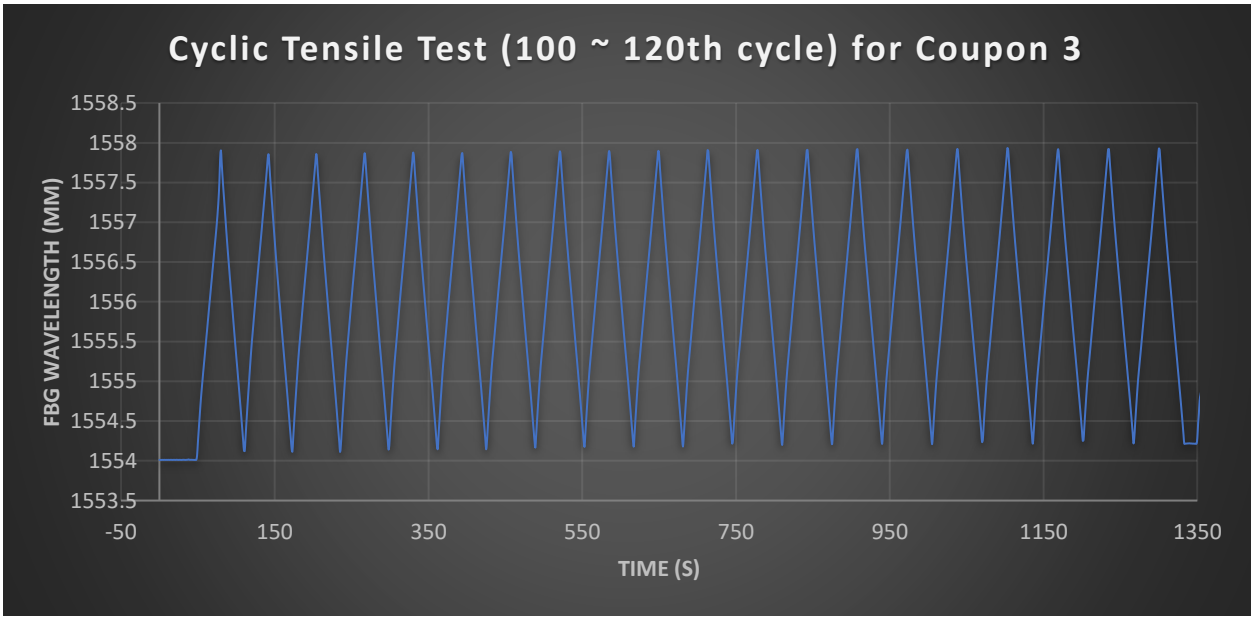

Figure 4.17 Cyclic Tensile Test for Coupon 3

The cyclic tests were conducted in batches of 5, 10, and 20 cycles for a total of 120 cycles. For each cycle batch, the period and amplitude were consistent. However, after each batch of testing, it started at a higher wavelength value compared to the prior cycle batch. The cyclic behaviour in Figure 4.15, shows an extra wedge pattern at the bottom of each cycle compared to a more natural V-shape cycle from the other two samples. This indicates that the coupons were slipping in the tensile machine grips. For such

reasons precaution was taken to ensure the following two samples were adequately tightened. More assemblies are to be made in the future to further test the reliability; however, the behavior similarity between the first three coupons are a good indication that this is a repeatable and replicable design. The only difference between the three coupons are the starting value of the FBG wavelength. However, this is due to the different FBG sensors have varying initial spectrum values [93]. This variance can be accounted for with proper calibration in the future. The wavelength shift after 120 cycles for each coupon can be seen in Figure 4.18, Figure 4.19, and Figure 4.20 respectively. The red and green vertical lines indicate the location of the peak identified by the ENLIGHT software.

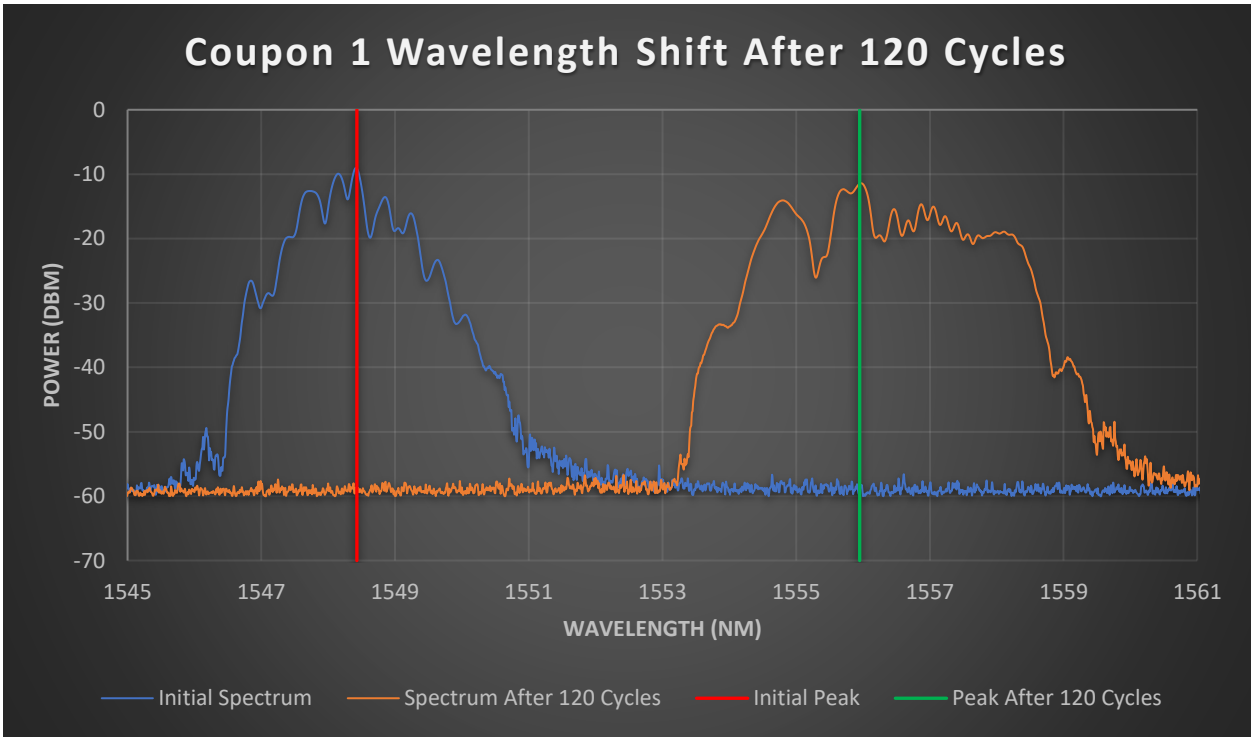

Figure 4.18 Coupon 1 Wavelength Shift After 120 Cycles

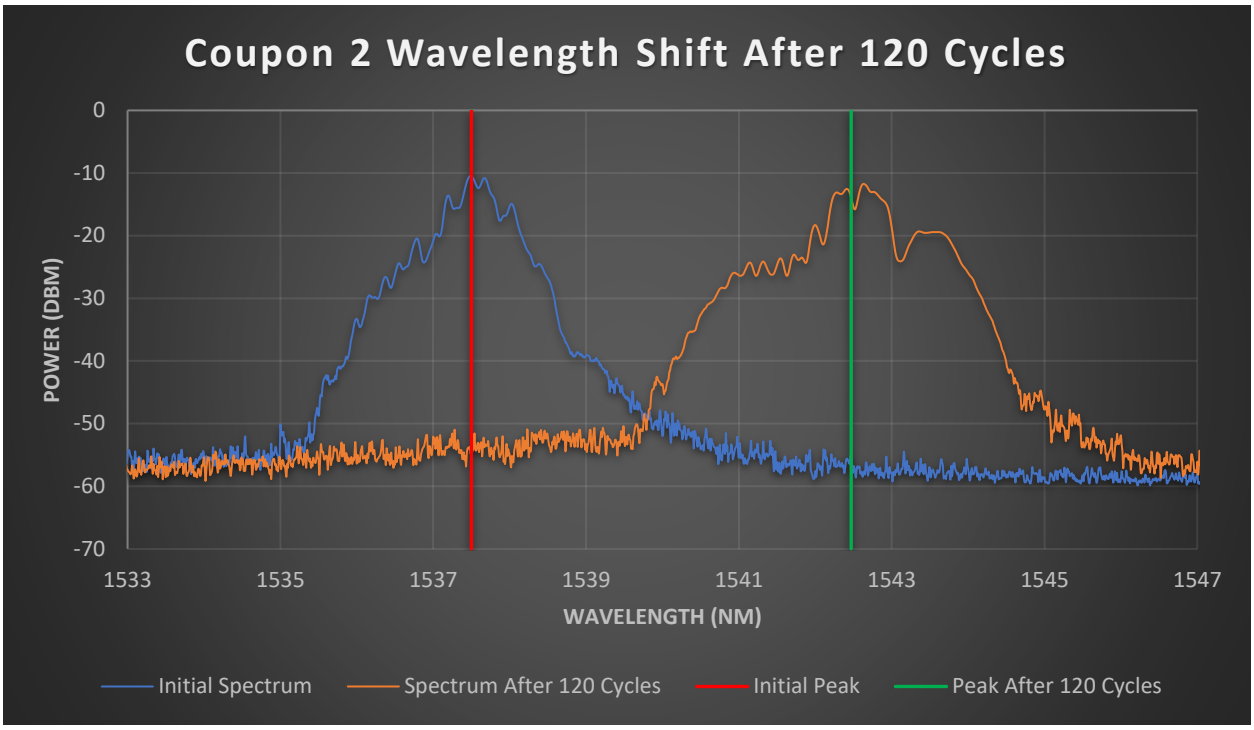

Figure 4.19 Coupon 2 Wavelength Shift After 120 Cycles

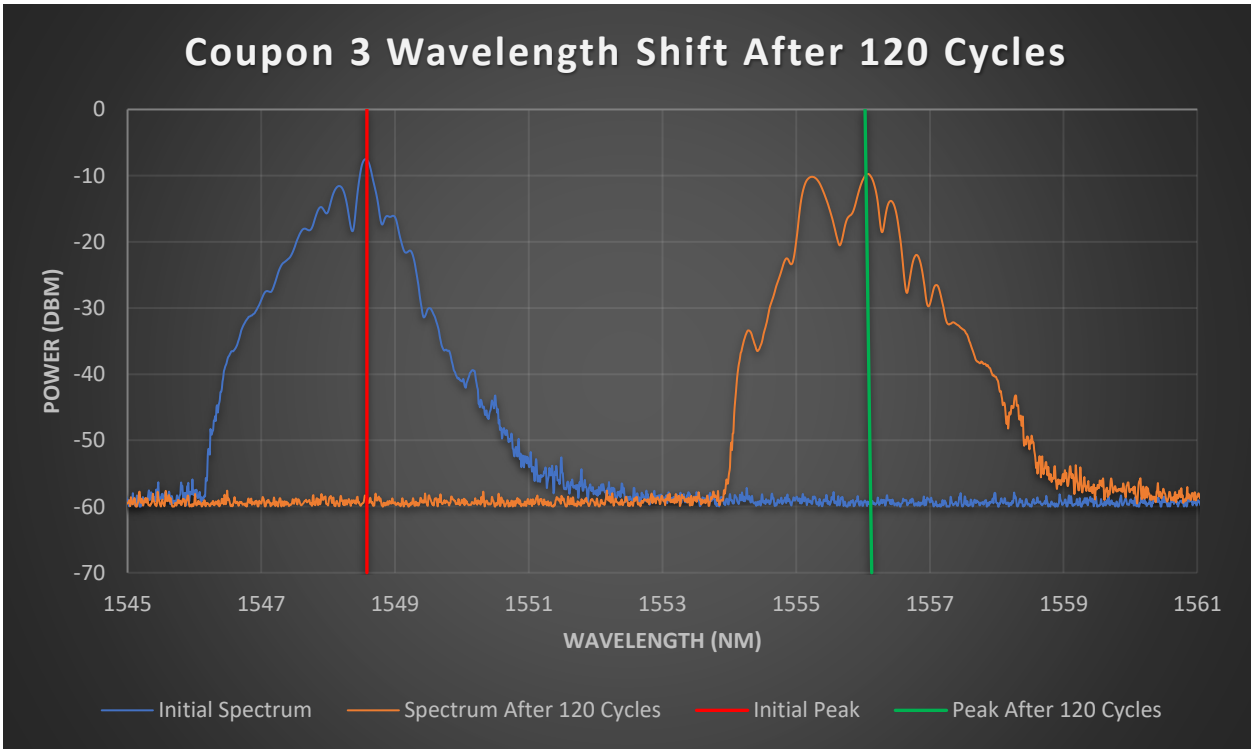

Figure 4.20 Coupon 3 Wavelength Shift After 120 Cycles

Various wavelength property changes between initial spectrum and spectrum after 120 cycles can be seen in Table 4.7 for all 3 coupons. After 120 cycles, all 3 wavelength readings shifted up substantially. This was an expected behaviour as it was hypothesized that the presence of the cured epoxy caused unwanted residual stress to enact on the fiber. In an application scenario, cyclic loading is necessary to allow the FBG-Coupon assembly to reach an equilibrium where the epoxy's residual stress does not change after each cycle and stays consistent. The table also shows that the spectrum's amplitude stays mostly unchanged with only a 1~2 dBm change after 120 cycles. By observing the changed spectrum, a clear-cut peak is hard to determine without the help peak detection software. The default peak detection algorithm used by the ENLIGHT software detected 3 peaks for coupon 1 and 2 peaks for the other two coupons after 120 cycles. The increase in number of peaks detected is due the deformity in the spectrum. The peak detection can be limited to only one by altering to software and to increase its accuracy, prior peak before the deformation can be utilized as a reference to monitor the new peak. By looking at the initial spectrum, it is possible to still trace the shifted location of that peak as the shape is still identifiable as seen by green line in Figure 4.18, Figure 4.19, and Figure 4.20.

Table 4.7 Spectrum Datasheet Before and After 120 Cycles

	Coupon 1	Coupon 2	Coupon 3
Initial Wavelength	1548.43 nm	1537.56 nm	1548.52 nm
Wavelength After 120 Cycles	1555.95 nm	1542.47 nm	1556.11 nm
Total Wavelength Shift	7.52 nm	4.91 nm	7.59 nm
Initial Peak Amplitude	50.90 dBm	49.94 dBm	52.11 dBm
Peak Amplitude After 120 Cycles	48.13 dBm	47.13 dBm	51.25 dBm
Initial Spectrum Width	4.5 nm	4.1 nm	4.4 nm
Spectrum Width After 120 Cycles	6.2 nm	5.9 nm	4.7 nm

As the value of the peak was still increasing at 120 cycles, it was desired to find at what point the spectrum stopped shifting. Coupon 2 was submitted to 120 extra cycles with a cumulative total of 240 cycles. It was found that the value stabilized after around 200 cycles at 1543.16 nm. This stabilization is thought to occur when residual stress inside the coupon gets fully relieved after multiple tension cycles and this was thought to be as the "initial calibration point" for the FBG-Coupon assembly. After the cyclic test, the coupon assembly was subjected to a breakage test to see how the spectrum behaves during breakage. The strain rate was kept as same as the cyclic tests and the change in wavelength at various points in the failure test can be seen in Figure 4.21.

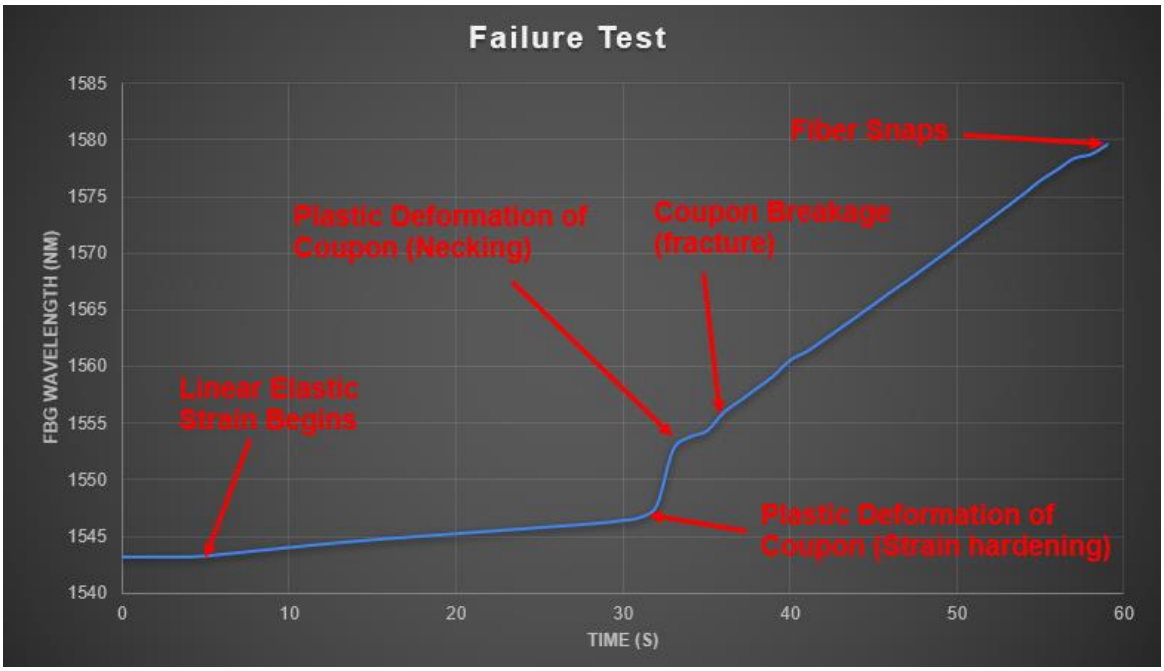

Figure 4.21 Coupon Failure Test

The tensile machine was activated 5 seconds into the testing where the elastic strain starts to occur due to the presence of tensile stress. The coupon's status was monitored to identify at which point on the graph the various stages of strain occurs. The linear increase in the FBG wavelength during the elastic region is a good indicator that the FBG readings reflect a valid and accurate reading of what is happening to the coupon. Once strain hardening occurs, the wavelength goes up rapidly until it enters the necking stage. What is interesting is that the fiber stays operational even after the coupon itself breaks. In a realistic scenario of smart product applications, there would be a warning to stop the product's operations once the FBG wavelength starts reaching the strain hardening section. Since the fiber still is operational and measures the wavelength long after fracture, the fiber could potentially be retrieved and reused again for future assemblies.

Table 4.8 Strain Stages at Failure

Strain Stage	Wavelength (nm)	Difference w/ Respect to Original Wavelength (nm)
Start of Elastic Strain	1543.16	0
Start of Strain Hardening	1546.65	3.49
Start of Necking	1552.69	9.53
Fracture	1555.09	11.93
Fiber Breaks	1579.60	36.44

4.3.3 Thermal Testing Results

During the duration of the epoxy curing for FBG installation and thermal testing of the coupon, the FBG peak wavelength was monitored as seen in Figure 4.22 and Figure 4.23 as an example for coupon 2. From the graph, it is easy to distinguish what curing stage the fiber is at during the process. The epoxy filled coupon was elevated to curing temperature and held for an hour and was cooled until it was at room temperature again. The discrepancy between the wavelength before and after curing shows that the cured fiber indeed introduces further residual stress to enact on the fiber. The fiber was able to accurately show the status of the coupon during the curing process. For the thermal testing, the details of the test can also be observed from the wavelength graph. Because of the analogue design of the thermal plate, the plate overshoots when reaching the target temperature. This overshoot is represented on the graph as the fiber wavelength exceeds its target when heating up. After each target temperature was reached and overshot, the plate turned off to cool the coupon to the determined target temperature, causing the wavelength to decrease. The plate heats up again as it undershoots beneath the specified temperature while cooling. This process was repeated until the plate stabilizes at its specified temperature. After reaching the final temperature, the wavelength drops as hotplate was turned off and the coupon starts to cool.

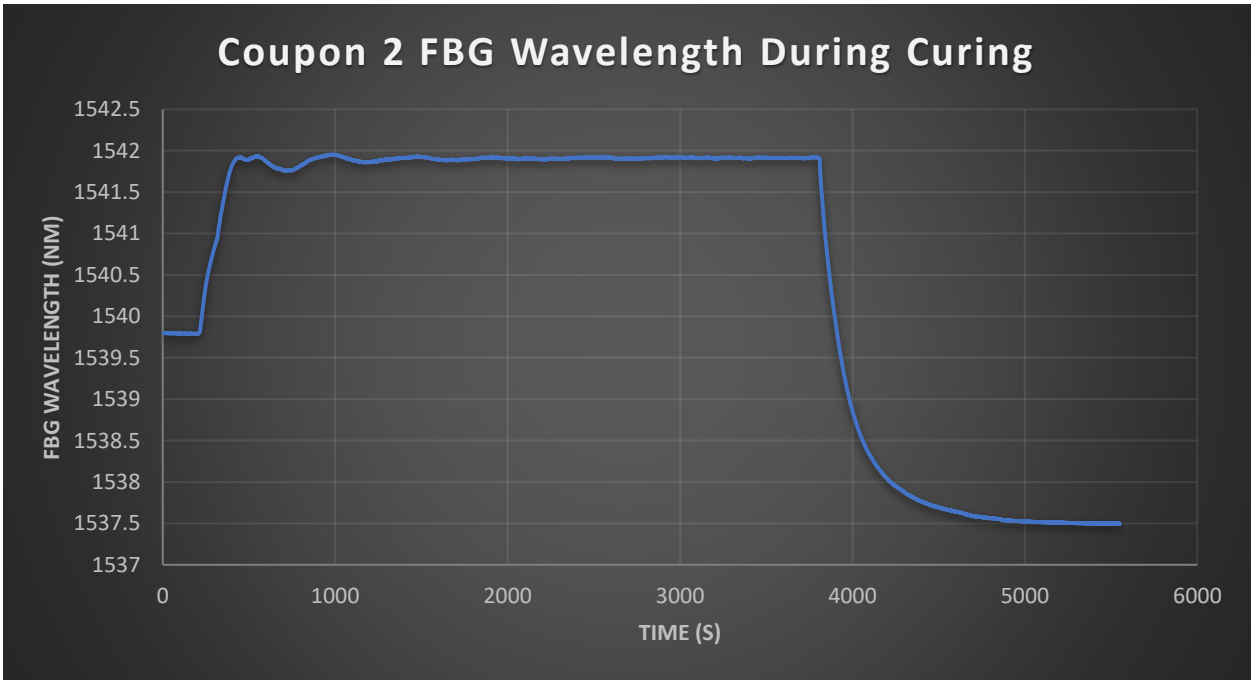

Figure 4.22 FBG Wavelength During Curing

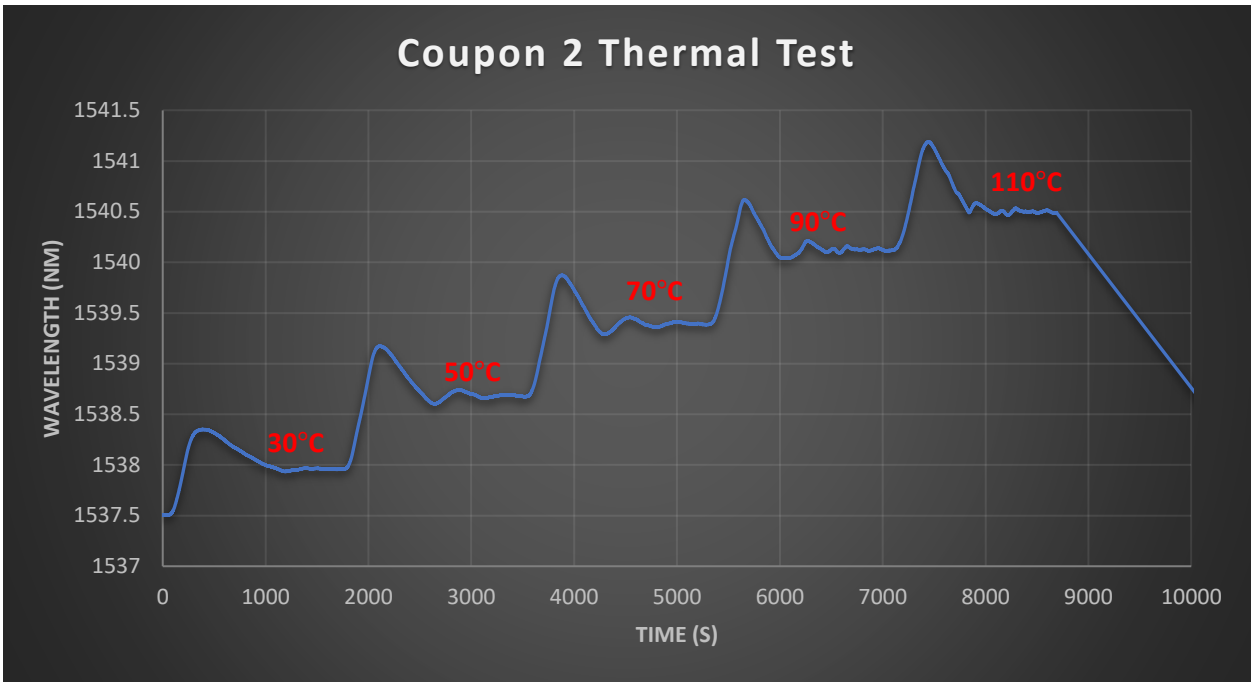

Figure 4.23 FBG Wavelength During Thermal Testing

Figure 4.24, Figure 4.25, and Figure 4.26 shows the compiled results from the temperature testing. The FBG wavelength changes depending on the ambient temperature of the hotplate that is heating up the coupon with the embedded FBG of the coupon. For coupon 1's behaviour seen in Figure 4.24 , for an increase in ambient temperature of 10°C, the FBG wavelength was increased by around 0.35 nm. Thus, the sensitivity of the embedded sensor was 0.0351 nm/°C. This is a value to note as bare FBG's temperature sensitivity is ~ 0.01 nm/°C. This means temperature sensitivity (slope) of the embedded FBG is about 3.5 times more sensitive than a bare FBG. Influence of the host material and the epoxy is expected to cause this differential and this discrepancy is a characterization/guideline that will need to be accounted for when making thermal readings using FBG sensors in thermal applications. For FBGs, increase in wavelength is proportional to the strain (caused by temperature in this test). Since the fitted line for the embedded FBG shows a linear relationship between the data points, this indicates that the sensor is having a constant/proper reading of the increase in temperature as the temperature values are linear to one another. Results for coupon 2 and 3 seen in Figure 4.25 and Figure 4.26 indicates that this is a repeatable result as it has showcased a similar trend and behaviour. The sensitivity values of the embedded sensors inside coupon 2 and coupon 3 were 0.0326 nm/°C and 0.0343 nm/°C respectively. Considering how sensitive FBGs are to slightest bit of tension or temperature change, the low variance of the sensitivity values are a good indication that a guideline based on the thermal test can be compiled.

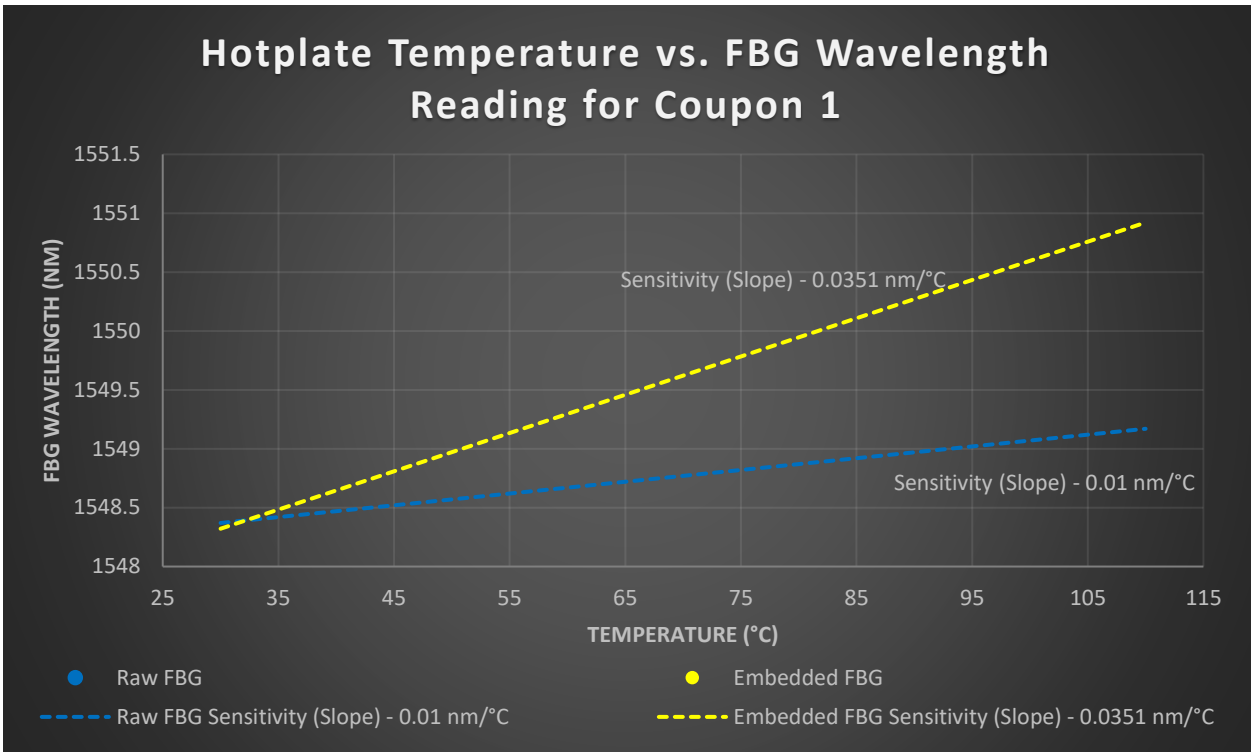

Figure 4.24 Temperature Characterization Data for Coupon 1

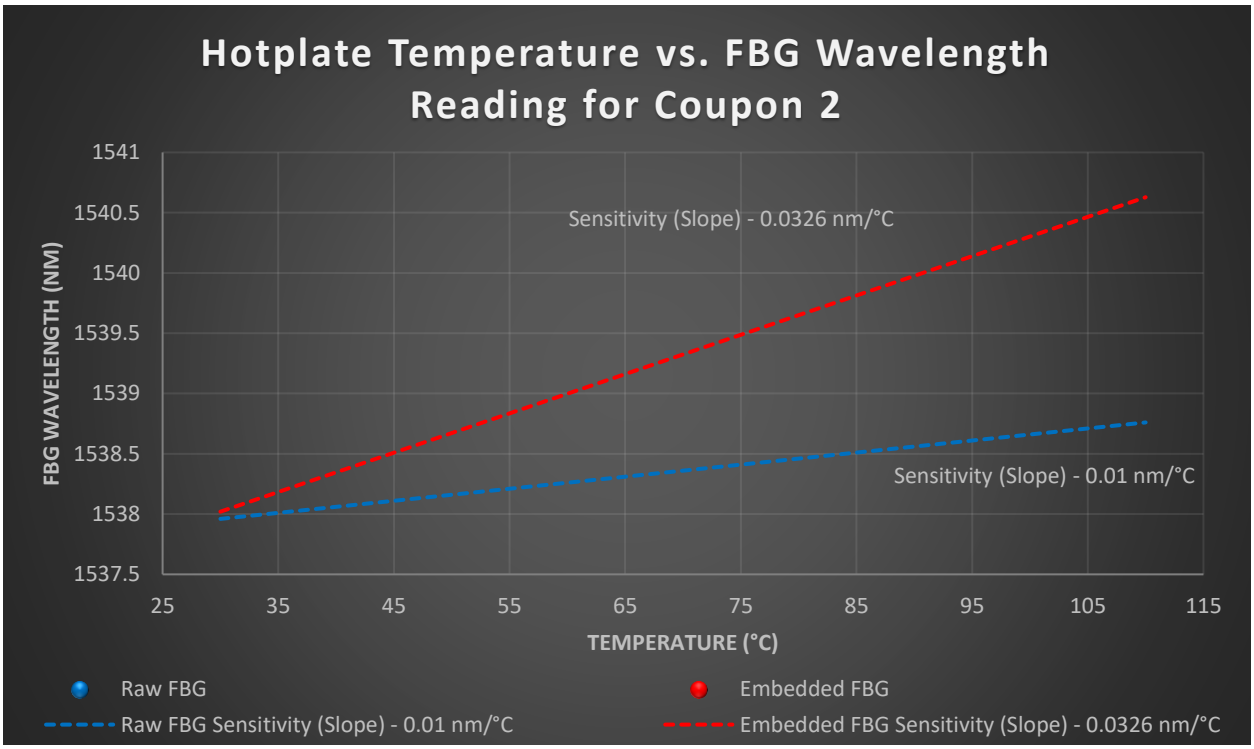

Figure 4.25 Temperature Characterization Data for Coupon 2

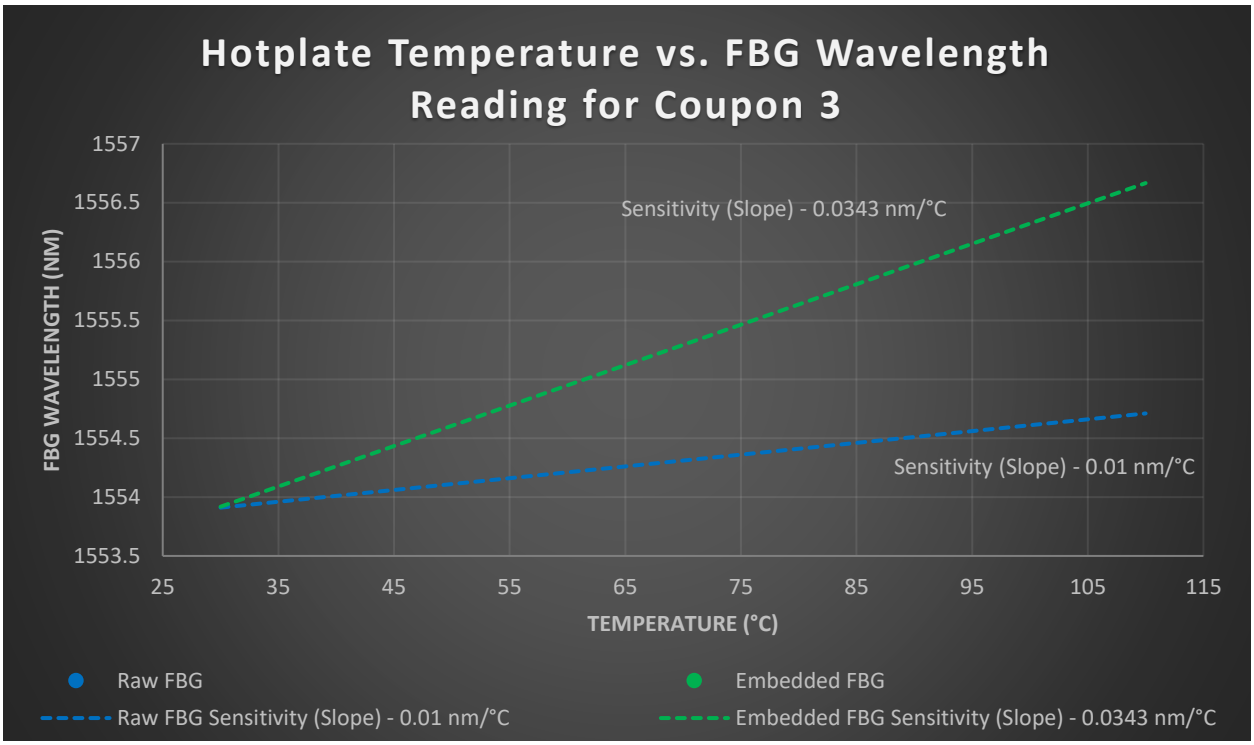

Figure 4.26 Temperature Characterization Data for Coupon 3

After combining the data from all 3 of the FBG-Coupon assemblies and calibrating the starting point of the sensors, it was found that FBG-Coupon assemblies are about 3.3 times more temperature sensitive compared to raw FBG. The combined graph can be seen in Figure 4.27 with the trendline and the error bars for each temperature point.

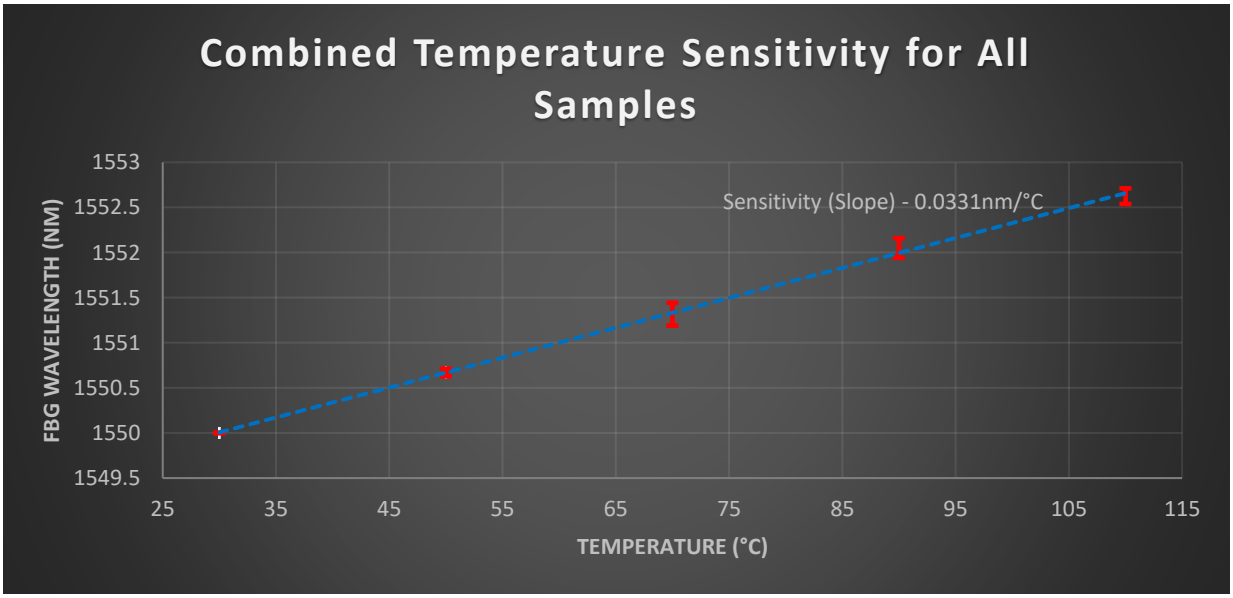

Figure 4.27 Combined Temperature Characterization Data

4.3.4 Curved Channels

As mentioned in the procedures section, coupons with curved channels were not able to be fully fabricated and tested due to the COVID-19 pandemic. However, some preliminary coupons were able to be fabricated as seen in Figure 4.28.

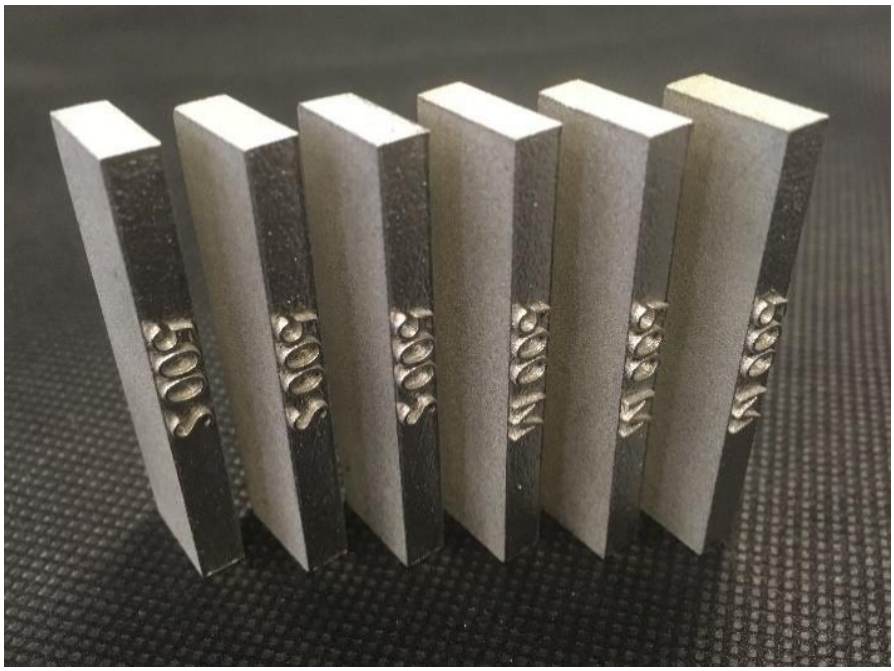

Figure 4.28 Curved Channel Coupons

Fabrication of a through channel within the coupons proved to be difficult as no through channel was formed even on the largest 800 micron channels as seen in Figure 4.29 and Figure 4.30. None of the coupons were able to yield a channel where the fiber could be passed through even with the shallowest curvature configurations. It can be seen in the CT scans that the rough geometry of the channel was formed but the outer edges of the channel ended up becoming rough and incomplete. It is hypothesized, just like with the straight channels, a through channel can be achieved by further optimizing the printing parameters. In future studies, finding the set of parameters for the curved channels should be the top priority to be able to embed and further test the FBG sensors. If optimized parameters cannot be obtained, the channel size can be increased to ~1mm diameter to allow the fiber to pass. However, such a large channel size would require the utilization of more epoxy which would increase the presence of residual stress and poorer stress translation from the coupon to the fiber.

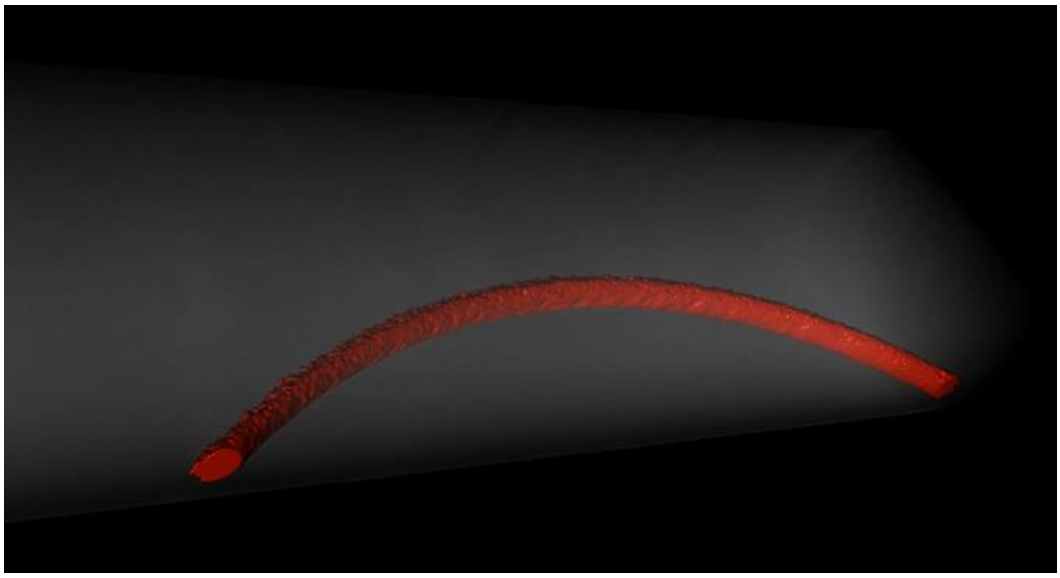

Figure 4.29 3D Isometric CT Scan View of Curved Channel Coupon (800 Micron)

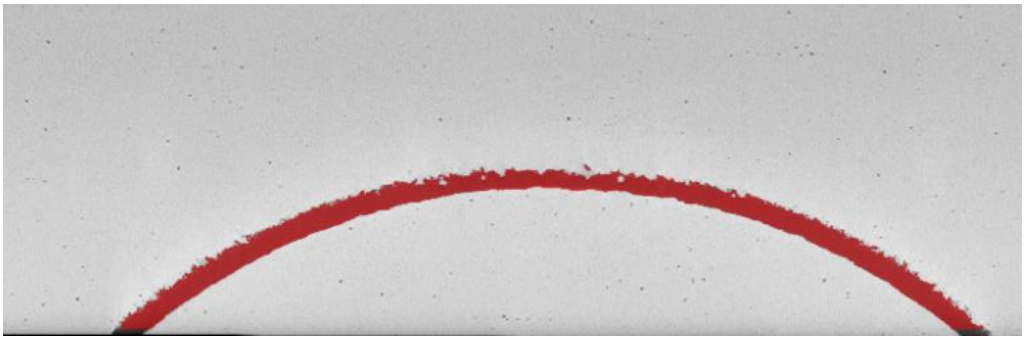

Figure 4.30 2D CT Scan View of Curved Channel Coupon (800 Micron)

4.4 Simulation Model Results

With the corresponding physics and mesh setup outlined in the procedures section, COMSOL simulation yielded a mechanical stress deformation and electric field norm figure as seen in Figure 4.31 and Figure 4.32 respectively. The deformation figure is overexaggerated to show a visual representative as in reality, the stress yielded in an elongation of around ~0.7 microns which would be difficult to observe by naked eye. Such a deformation was expected based on the tensile loading scenario and the amount of stress applied. Figure 4.32 looks at the electric field activity for the fiber's core and cladding. The shined light travelled within the core as seen by the high electrical field. The cladding was able to keep majority of the light within the core as the cladding had near zero electrical activity for most of its section. Some of the light leaked into the cladding as seen by the green propagation pattern near the core-cladding boundary. However, this is a phenomenon that also occurs in actual FBG sensors. Since the loss

of light is minimal, it will not be an issue when detecting the Bragg wavelength. This electrical activity hints that the simulation was setup properly as the FBG sensor and the shined light behaves as they would for actual physical testing scenarios. Other FBG simulation studies all showed similar behaviour where most of the electrical activity occurred only at the core of the fiber [94].

Figure 4.31 Overexaggerated Stress Deformation from Tensile Stress

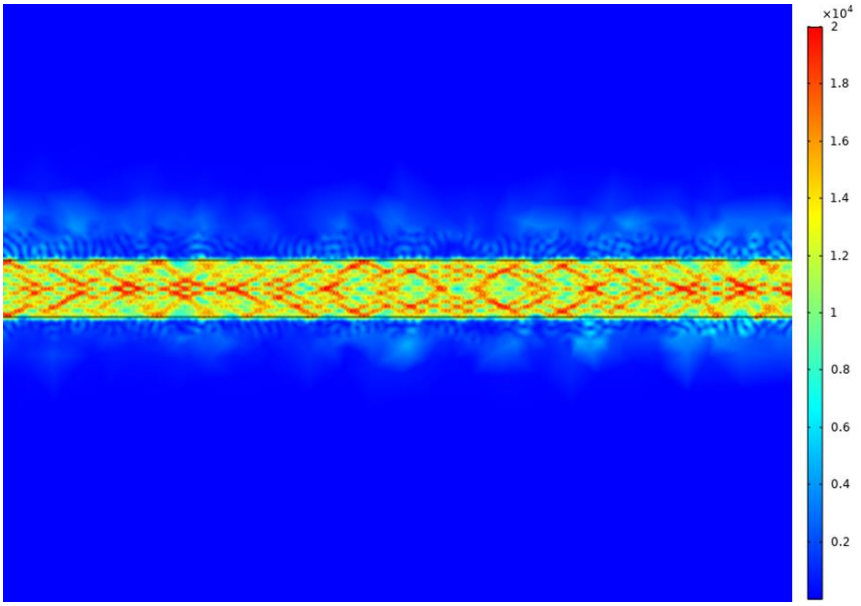

Figure 4.32 Electric Field Norm for Fiber's Core and Cladding (V/m)

The reflection spectrum for each of the fiber angles and coupon sizes were graphed as seen on Figure 4.33, Figure 4.34, and Figure 4.35. Regardless of the coupon size, Bragg wavelength of the straight coupon was the highest and its wavelength decreases as the fiber is bent more. The fiber with 15° bend only slightly decreases the Bragg wavelength while at 90°, the effects are more pronounced as the wavelength is drastically lower. In other studies where spectrum readings were monitored with varying bend radius, it was found that a higher bend angle resulted in a decreased Bragg wavelength just like with the obtained results [95]. This was thought to have been caused by less efficient stress transfer along the direction of the applied stress for fibers embedded at greater angles. As a result, the stress readings are not as high which leads to a lower Bragg wavelength. Bragg's wavelength on average is higher for the coupons with a larger radius/cross-section. This was an expected behaviour as the value of stress is kept constant for all 3 coupon size variations. As the value of the cross-section is bigger, the value of the force must increase to have a constant stress value as Stress $= \frac{\text{Force}}{Area}$. Higher force results in greater tension applied on the coupon, raising the peak value of the spectrum as the coupon sizes were increased. The amplitude of the peaks are consistent throughout the varying coupon sizes and curvatures. The range of peak value obtained is reasonable based on the parameters of the grating period and index of refraction values used in the simulation. Based on Bragg's equation of $\lambda_B = 2\eta_{eff}\Lambda$, the peak was expected to occur in the 1554~1556 nm range and all the peaks occurred within the range. Table 4.9 shows all of the peak values obtained in the simulation and Table 4.10 shows how much the Bragg wavelength decreased by for each fiber angle orientation.

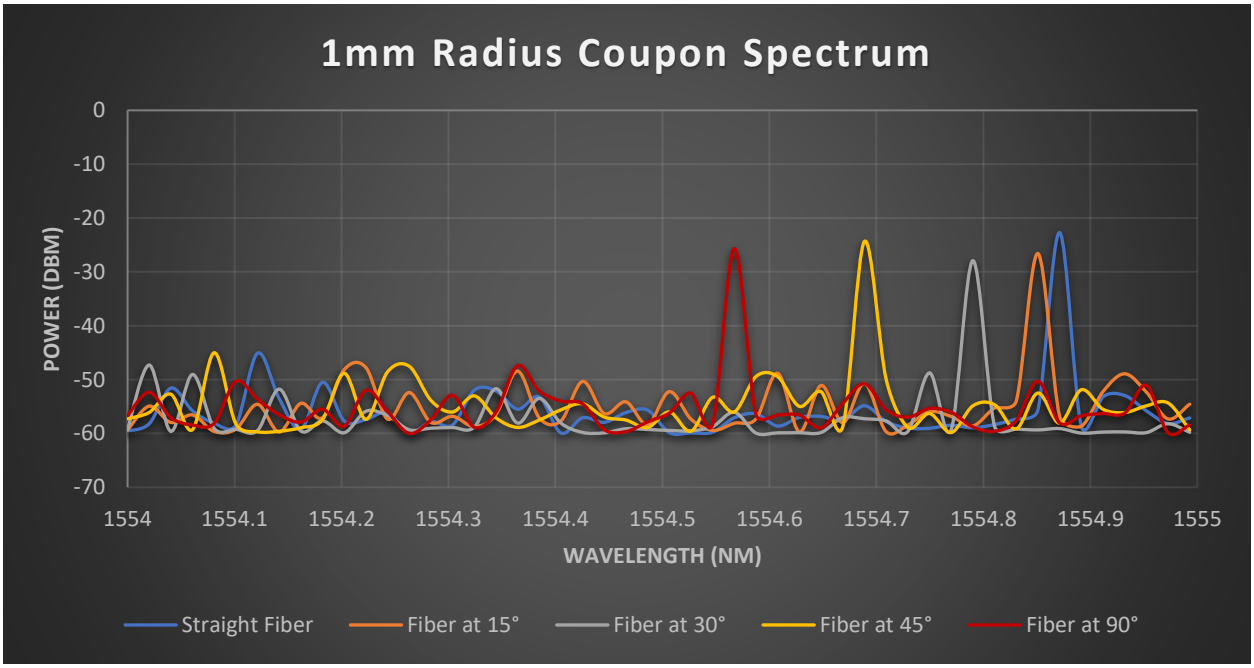

Figure 4.33 Simulated FBG Spectrum for 2mm Curved Coupon

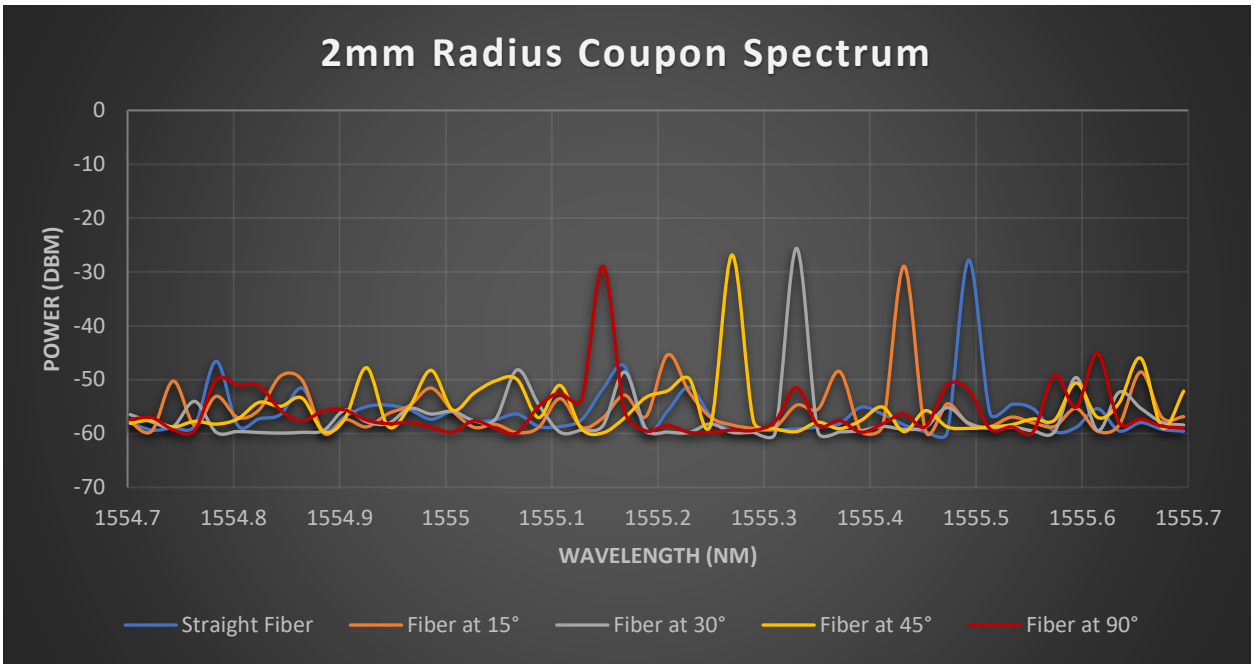

Figure 4.34 Simulated FBG Spectrum for 4mm Curved Coupon

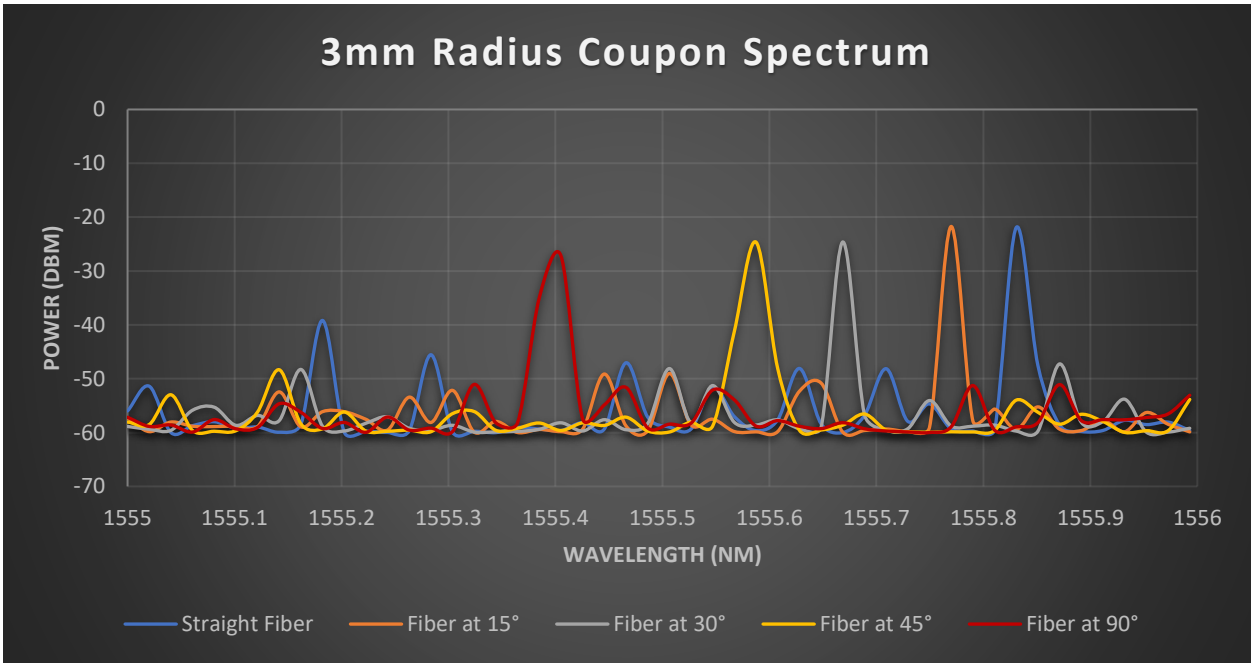

Figure 4.35 Simulated FBG Spectrum for 6mm Curved Coupon

Table 4.9 COMSOL Simulation Peak Values

	Straight Fiber	Fiber at 15º	Fiber at 30º	Fiber at 45º	Fiber at 90º
1mm Rad. Coupon	1554.87	1554.85	1554.79	1554.69	1554.57
2mm Rad. Coupon	1555.49	1555.43	1555.33	1555.28	1555.15
3mm Rad. Coupon	1555.83	1555.77	1555.67	1555.59	1555.41

Table 4.10 Decrease in Bragg Wavelength Relative to Straight Fiber

	Fiber at 15º	Fiber at 30º	Fiber at 45º	Fiber at 90º
1mm Rad. Coupon	0.02	0.08	0.18	0.3
2mm Rad. Coupon	0.06	0.16	0.21	0.34
3mm Rad. Coupon	0.06	0.16	0.24	0.42

With the obtained peak values, the characterization of the shift was compiled as seen in Figure 4.36. The peak decrease for angle orientations were in a similar range for each angle. With the discrepancy being the smallest at 0.03nm at 45º and 0.12nm at 90º. A linear relationship can be argued for the sensitivity of the fiber from varying fiber orientation angle. From the data points, a trendline showed a linear pattern for decreasing wavelength in relation to fiber angle. Although the line could be fitted better, it still yields a sensitivity (slope) value that can be applied to all the data points with general accuracy. From the data, the sensitivity is around 0.004nm decrease in wavelength per degree increase of the fiber angle. However, further datapoints are recommended to be generated to conclusively state that the relationship is indeed linear.

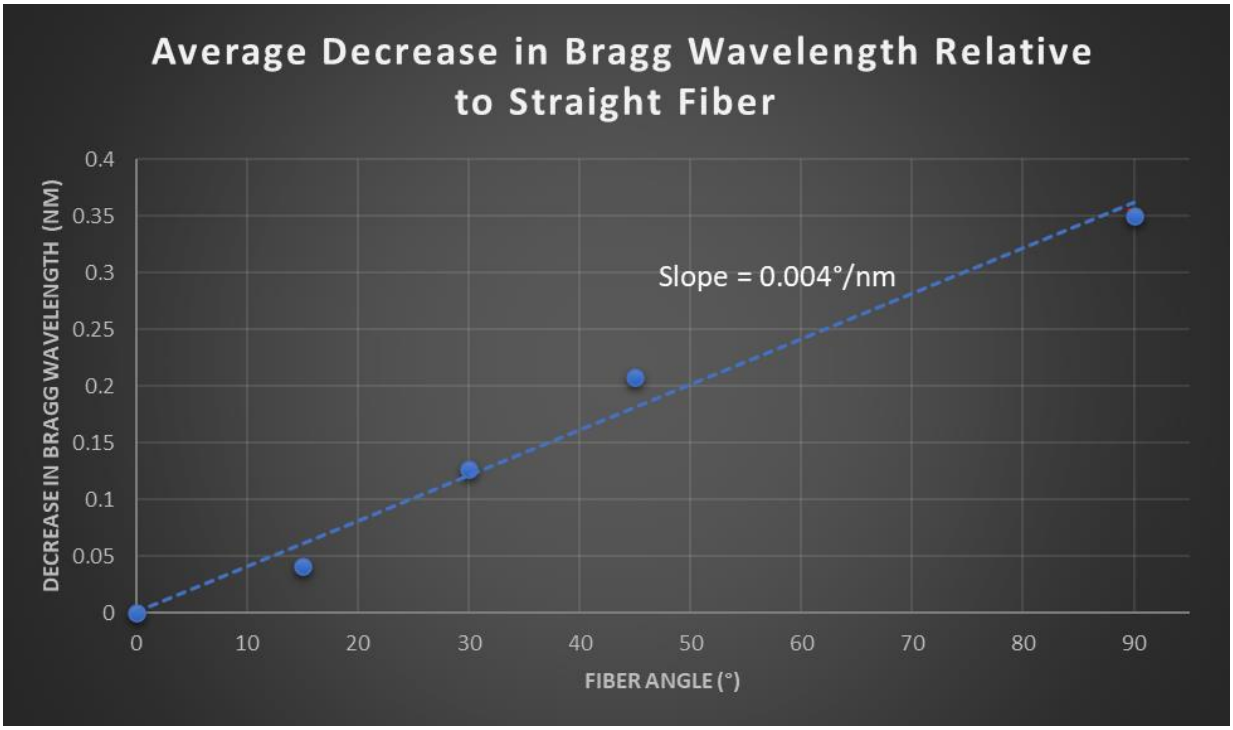

Figure 4.36 Average Decrease in Bragg Wavelength Relative to Straight Fiber

4.5 Summary of Results

To create coupons capable of accommodating FBG sensors, LPBF printing parameters needed to be optimized. Such optimized values were seen in Table 14. The process required the usage of a 133W laser and a vertical printing orientation. The smallest possible channel diameter achievable was 500 microns for a channel length of around 4.3cm, which was the shortest possible length of the coupon for it to successfully accommodate for the sensor and being able to conduct a tensile test.

The embedding of the fiber into the coupon was done by sliding the fiber into the channel and injecting 353ND Optical Epoxy made by Paisley. Due to the presence of the epoxy, 600 micron channel diameter was used for the final assembly. The assembly was cured at 150^{o}C for one hour and the spectrum still maintained its distinct peak after embedding.

The elastic limit of the coupons ranged from 141.52MPa to 145.89MPa with the 600 micron channel variation having an elastic limit of 141.52 MPa. Using the elastic limit, cyclic tests were conducted in batches for 3 separate assemblies. Each batch of cyclic test gave consistent period/amplitude readings and it took around 200 cycles to relieve the residual stress. Such cyclic loading procedure is highly recommended for any future embedding as it will stabilize and calibrate the FBG peak readings.

It was found possible to identify the general stages of fracture the material is under by monitoring the FBG spectrum. The spectrum peak readings were linearly increasing during the elastic region. The elastic strain region should be the focus for monitoring as once the material enters strain hardening section, it would likely not be reusable for future operations due to damage. Strain hardening occurs at a Bragg wavelength increase of ~3.5 nm and its values dramatically increased linearly during the phase. It was found that the FBG sensors are still operational even after the fracture of the host material which occurs after Bragg wavelength increase of about 12 nm.

During its curing and thermal testing, the spectrum behaved as anticipated, accurately measuring the temperature status of the host coupon. On average, the sensors had a thermal sensitivity of 0.0331 nm/^{o}C compared to a sensitivity of 0.01 nm/^{o}C of a bare fiber with minimal discrepancy in value between the various assemblies.

As the size of the coupon was increased, peak wavelength of the fiber increased as the tensile stress applied on the coupon increases as well. Also, as the fiber was more curved inside the coupon, the peak wavelength value decreases as well as stress translation along direction of stress gets more inefficient. A linear fit can be seen in relation to the fiber angle and decrease in wavelength with its sensitivity being around 0.004nm decrease in wavelength per degree increase of the fiber angle.

Chapter 5
Conclusions and Future Work

5.1 Conclusions

This thesis set out to explore the feasibility of creating smart products by utilizing FBG sensors and additive manufacturing process of LPBF. After successful creation of the coupons and embedding of the fiber, various tests were conducted to understand its characteristics. Utilizing the observed data and behaviour from the tests, future designers can design FBG embedded smart products with the established baseline and parameters. Following are the conclusions drawn from this thesis:

- To create the ideal coupons to be used as a smart product proof of concept, 316 Stainless Steel coupons were created via LPBF using the Renishaw AM400 machine. To create channels small enough to effectively accommodate the fiber, the printing parameters requires optimization.
- Spectrum peak readings during cyclic testing yielded consistent and accurate values for its period and amplitude, indicating FBG sensor's accuracy for tensile stress monitoring. However, after each test batch, the value of the wavelength increased due to the relief in residual stress. The spectrum broadened as the residual stress got relieved, but the peak amplitude stayed consistent.
- The thermal testing showed that FBG sensors were able to properly measure temperature changes and found that its temperature sensitivity was linear. These factors and the obtained thermal sensitivity value can be utilized to create or calibrate future designs.
- Due to lack of access to AM400 machine and physical testing equipment during the pandemic, a completed version of the curved channel coupon could not be fabricated. Even at an 800 micron channel diameter, a fully through channel was unable to be achieved. To achieve clearance, a larger channel diameter of 1mm or attempting to further optimize the printing parameter is recommended.
- COMSOL simulation was successfully able to replicate the behaviour of FBG-Coupon assembly by incorporating physics of mechanics and electromagnetism. The coupon was successfully simulated with elastic stress applying tension of the coupon with the reflectivity spectrum of the FBG sensor being generated concurrently.
- Wavelength peak increased with increased force and decreased as angle of bent fiber inside was increased. These were all expected behaviors for the wavelength, indicating its feasibility in smart product applications. Depending on the application of the smart product and how precise the measurements must be, the designer can determine their max embedding angles to have more flexibility on their design geometry while sacrificing accuracy as compensation.

5.2 Future Work

For future work, working with different materials for the coupon and epoxy is recommended. This way a more extensive guideline and knowledge for designing smart product concepts can be obtained. With a more extensive guideline, the designer can have more alternatives to refer to in their material choice and epoxy when designing their product. Also, conducting more curvature tests at various angles will give an even fuller picture on a curvature's effects on peak wavelength reading.

Since FBG sensors can detect parameters outside of tensile and thermal stress, its functionality on other measurands is desirable to find out. Also, as FBG sensors can be multiplexed to have one fiber detect various types of data, one fiber could be set up to detect both temperature and tensile stress. However, as this is a field that is still in development, more extensive background research is recommended.

As discussed in the results section, being able to fabricate the curved coupon to add further analysis in addition to the COMSOL simulation is highly desired. This would also lead to understanding appropriate channel size and/or printing parameters for channels with curvature. With the curved channel, the tensile and thermal tests should be duplicated to characterize its behaviour compared to normal coupons.

References

1. Mihailov, S. J. (2012a). Fiber bragg grating sensors for harsh environments. *Sensors*, *12*(2), 1898–1918. https://doi.org/10.3390/s120201898
2. Mrad, N., Sparling, S., & Laliberte, J. (1999b). Strain Monitoring and Fatigue Life of Bragg Grating Fiber Optic Sensors. *Smart Structures and Materials 1999: Sensory Phenomena and Measurement Instrumentation for Smart Structures and Materials*, *3670*(May 1999), 82–91. https://doi.org/10.1117/12.349717
3. Kreuzer, M. (2006c). Strain Measurement with Fiber Bragg Grating Sensors. *HBM, Darmstadt, S2338-1.0 e*, 1–9. https://doi.org/10.1097/ACO.0b013e3282fe6e70
4. Jin, L., Zhang, W., Zhang, H., Liu, B., Zhao, J., Tu, Q., Kai, G., & Dong, X. (2006d). An embedded FBG sensor for simultaneous measurement of stress and temperature. *IEEE Photonics Technology Letters*, *18*(1), 154–156. https://doi.org/10.1109/LPT.2005.860046
5. Liang, W., Huang, Y., Xu, Y., Lee, R. K., & Yariv, A. (2005e). Highly sensitive fiber Bragg grating refractive index sensors. *Applied Physics Letters*, *86*(15), 1–3. https://doi.org/10.1063/1.1904716
6. Morey, W. W., Dunphy, J. R., & Meltz, G. (1991f). Multiplexing fiber bragg grating sensors. *Fiber and Integrated Optics*, *10*(4), 351–360. https://doi.org/10.1080/01468039108201715
7. Adam, G. A. O., & Zimmer, D. (2015g). On design for additive manufacturing: evaluating geometrical limitations. *Rapid Prototyping Journal*, *21*(6).
8. Vicente, M. F., Canyada, M., & Conejero, A. (2015h). Identifying limitations for design for manufacturing with desktop FFF 3D printers. *International Journal of Rapid Manufacturing*, *5*(1), 116. https://doi.org/10.1504/ijrapidm.2015.073551
9. Feng, D., Zhou, W., Qiao, X., & Albert, J. (2015i). Compact optical fiber 3D shape sensor based on a pair of orthogonal tilted fiber bragg gratings. *Scientific Reports*, *5*(October), 1–7. https://doi.org/10.1038/srep17415
10. Li, H.-N. (2007j). Strain transfer analysis of embedded fiber Bragg grating sensor under nonaxial stress. *Optical Engineering*, *46*(5), 054402. https://doi.org/10.1117/1.2739554
11. Kashyap, R. (2010k). Fiber Bragg Gratings. *Fiber Bragg Gratings*, *4309*(March 1997). https://doi.org/10.1016/C2009-0-16830-7
12. Uozu, Y., Sikes, P. E. L., Healy, A. E. M., Application, F., & Data, P. (1989l). *Cladding Material for Optical Fiber*.
13. Hill, K. O., & Meltz, G. (1997m). Fiber Bragg grating technology fundamentals and overview. *Journal of Lightwave Technology*, *15*(8), 1263–1276. https://doi.org/10.1109/50.618320

14. Friebele, E. J. (1998n). Fiber Bragg grating strain sensors: present and future applications in smart structures. *Optics and Photonics News*, *33*(August), 33–37.
15. Meszaros, P. (2017o). *Single and Dual-Parameter Fiber Bragg Grating Sensors Embedded in Metallic Structures by*.
16. Giurgiutiu, V. (2015p). Structural health monitoring (SHM) of aerospace composites. In *Polymer Composites in the Aerospace Industry*. https://doi.org/10.1016/B978-0-85709-523-7.00016-5
17. Chen, J., Liu, B., & Zhang, H. (2011q). Review of fiber Bragg grating sensor technology. *Frontiers of Optoelectronics in China*, *4*(2), 204–212. https://doi.org/10.1007/s12200-011-0130-4
18. Patrick, H. J., Williams, G. M., Kersey, A. D., Pedrazzani, J. R., & Vengsarkar, A. M. (1996r). Hybrid fiber Bragg grating/long period fiber grating sensor for strain/temperature discrimination. *IEEE Photonics Technology Letters*, *8*(9), 1223–1225. https://doi.org/10.1109/68.531843
19. Kersey, A. D., Davis, M. A., Patrick, H. J., LeBlanc, M., Koo, K. P., Askins, C. G., Putnam, M. A., & Friebele, E. J. (1997s). Fiber grating sensors. *Journal of Lightwave Technology*, *15*(8), 1442–1462. https://doi.org/10.1109/50.618377
20. Peters, K., Pattis, P., Botsis, J., & Giaccari, P. (2000t). Experimental verification of response of embedded optical fiber Bragg grating sensors in non-homogeneous strain fields. *Optics and Lasers in Engineering*, *33*(2), 107–119. https://doi.org/10.1016/S0143-8166(00)00033-6
21. Kashyap, R. (2009u). Fiber bragg gratings. In *Academic press*.
22. Giallorenzi, T. G., Bucaro, J. A., Dandridge, A., Sigel, G. H., Cole, J. H., Rashleigh, S. C., & Priest, R. G. (1982v). Optical Fiber Sensor Technology. *IEEE Transactions on Microwave Theory and Techniques*, *30*(4), 472–511. https://doi.org/10.1109/TMTT.1982.1131089
23. Culshaw, B. (2004w). Optical Fiber Sensor Technologies: Opportunities and - Perhaps - Pitfalls. *Journal of Lightwave Technology*, *22*(1), 39–50. https://doi.org/10.1109/JLT.2003.822139
24. Marzbanrad, B., Ahmed, F., Jahed, H., & Toyserkani, E. (2018x). *Application Of FBG Optical Sensors To In-Situ Monitoring The Thermo-Mechanical Behaviour Of Cold Spray Coated Samples*. 1–5. https://doi.org/10.25071/10315/35388
25. Pahlevanpour, A., Marzbanrad, B., Behravesh, S. B., & Jahed, H. (2018y). *Application Of Fiber Bragg Grating Sensor For Strain Measurement At The Notch Tip Under Cyclic Loading*. 1–5. https://doi.org/10.25071/10315/35396
26. Havermann, D., Mathew, J., MacPherson, W. N., Maier, R. R. J., & Hand, D. P. (2015z). Temperature and Strain Measurements With Fiber Bragg Gratings Embedded in Stainless Steel 316. *Journal of Lightwave Technology*, *33*(12), 2474–2479. https://doi.org/10.1109/JLT.2014.2366835

27. Marzbanrad, B., Jahed, H., & Toyserkani, E. (2018aa). On the evolution of substrate's residual stress during cold spray process: A parametric study. *Materials and Design*, *138*, 90–102. https://doi.org/10.1016/j.matdes.2017.10.062

28. Xie, F., Chen, X., Zhang, L., & Song, M. (2006ab). Realisation of an effective dual-parameter sensor employing a single fibre Bragg grating structure. *Optics and Lasers in Engineering*, *44*(10), 1088–1095. https://doi.org/10.1016/j.optlaseng.2005.08.004

29. Casas, J. R., & Cruz, P. J. S. (2003ac). Fiber optic sensors for bridge monitoring. *Journal of Bridge Engineering*, *8*(6), 362–373. https://doi.org/10.1061/(ASCE)1084-0702(2003)8:6(362)

30. Marzbanrad, B., Jahed, H., & Toyserkani, E. (2016ad). On the sensitivity and repeatability of fiber Bragg grating sensors used in strain and material degradation measurement of magnesium alloys under cyclic loads. *International Journal of Advanced Manufacturing Technology*, *86*(9–12), 3453–3461. https://doi.org/10.1007/s00170-016-8485-8

31. Wang, J. N., & Tang, J. L. (2010ae). Feasibility of fiber bragg grating and long-period fiber grating sensors under different environmental conditions. *Sensors (Switzerland)*, *10*(11), 10105–10127. https://doi.org/10.3390/s101110105

32. Shen, W., Wang, X., Xu, L., & Zhao, Y. (2018af). Strain transferring mechanism analysis of the substrate-bonded FBG sensor. *Optik*, *154*, 441–452. https://doi.org/10.1016/j.ijleo.2017.10.097

33. Grant, J., Kaul, R. K., Taylor, S. L., Jackson, K. v., Osei, A. J., & Sharma, A. (2003ag). Investigation of structural properties of carbon-epoxy composites using fiber-Bragg gratings. *Applications of Photonic Technology 5*, *4833*(February 2003), 191. https://doi.org/10.1117/12.473813

34. Jewart, C., Chen, K. P., McMillen, B., Bails, M. M., Levitan, S. P., Canning, J., & Avdeev, I. v. (2006ah). Sensitivity enhancement of fiber Bragg gratings to transverse stress by using microstructural fibers. *Optics Letters*, *31*(15), 2260. https://doi.org/10.1364/ol.31.002260

35. Kang, S. G., Kang, D. H., & Kim, C. G. (2009ai). Real-time monitoring of transverse thermal strain of carbon fiber reinforced composites under long-term space environment using fiber optic sensors. *NDT and E International*, *42*(5), 361–368. https://doi.org/10.1016/j.ndteint.2009.01.001

36. Brambilla, G., & Rutt, H. (2002aj). Fiber Bragg gratings with enhanced thermal stability. *Applied Physics Letters*, *80*(18), 3259–3261. https://doi.org/10.1063/1.1475366

37. Harsch, Margit, Karger-Kocsis, J., & Herzog, F. (2008ak). Monitoring of Cure-Induced Strain of an Epoxy Resin by Fiber Bragg Grating Sensor. *Journal of Applied Polymer Science*, *107*(2), 719–725. https://doi.org/10.1002/app

38. Esposito, M., Buontempo, S., Petriccione, A., Zarrelli, M., Breglio, G., Saccomanno, A., Szillasi, Z., Makovec, A., Cusano, A., Chiuchiolo, A., Bajko, M., & Giordano, M. (2013al). Fiber Bragg Grating

sensors to measure the coefficient of thermal expansion of polymers at cryogenic temperatures. *Sensors and Actuators, A: Physical*, *189*, 195–203. https://doi.org/10.1016/j.sna.2012.09.016

39. Chiuchiolo, A., Bajko, M., Perez, J. C., Bajas, H., Consales, M., Giordano, M., Breglio, G., & Cusano, A. (2014am). Fiber bragg grating cryosensors for superconducting accelerator magnets. *IEEE Photonics Journal*, *6*(6). https://doi.org/10.1109/JPHOT.2014.2343994
40. Zawadzki, P., & Zywicki, K. (2016an). Smart product design and production control for effective mass customization in the industry 4.0 concept. *Management and Production Engineering Review*, *7*(3), 105–112. https://doi.org/10.1515/mper-2016-0030
41. Gutierrez, C., Garbajosa, J., Diaz, J., & Yague, A. (2013ao). Providing a consensus definition for the term "Smart Product." *Proceedings of the International Symposium and Workshop on Engineering of Computer Based Systems*, 203–211. https://doi.org/10.1109/ECBS.2013.26
42. Santos, K., Loures, E., Piechnicki, F., & Canciglieri, O. (2017ap). Opportunities Assessment of Product Development Process in Industry 4.0. *Procedia Manufacturing*, *11*(June), 1358–1365. https://doi.org/10.1016/j.promfg.2017.07.265
43. Murukeshan, V. M., Chan, P. Y., Ong, L. S., & Seah, L. K. (2000aq). Cure monitoring of smart composites using Fiber Bragg Grating based embedded sensors. *Sensors and Actuators, A: Physical*, *79*(2), 153–161. https://doi.org/10.1016/S0924-4247(99)00266-6
44. Ilgin, M. A., Ondemir, O., & Gupta, S. M. (2014ar). An approach to quantify the financial benefit of embedding sensors into products for end-of-life management: A case study. *Production Planning and Control*, *25*(1), 26–43. https://doi.org/10.1080/09537287.2012.655801
45. Giurgiutiu, Victor, & Cuc, A. (2005as). Embedded non-destructive evaluation for structural health monitoring, damage detection, and failure prevention. *Shock and Vibration Digest*, *37*(2), 83–105. https://doi.org/10.1177/0583102405052561
46. ASTM International. (2013at). F2792-12a - Standard Terminology for Additive Manufacturing Technologies. *Rapid Manufacturing Association*, 10–12. https://doi.org/10.1520/F2792-12A.2
47. Hegab, H. A. (2016au). Design for additive manufacturing of composite materials and potential alloys: A review. In *Manufacturing Review* (Vol. 3). https://doi.org/10.1051/mfreview/2016010
48. Huang, S. H., Liu, P., Mokasdar, A., & Hou, L. (2013av). Additive manufacturing and its societal impact: A literature review. *International Journal of Advanced Manufacturing Technology*, *67*(5–8), 1191–1203. https://doi.org/10.1007/s00170-012-4558-5
49. Wong, K. v., & Hernandez, A. (2012aw). A Review of Additive Manufacturing. *ISRN Mechanical Engineering*, *2012*, 1–10. https://doi.org/10.5402/2012/208760

50. Kruth, J. P., Leu, M. C., & Nakagawa, T. (1998ax). Progress in additive manufacturing and rapid prototyping. *CIRP Annals - Manufacturing Technology*, *47*(2), 525–540. https://doi.org/10.1016/S0007-8506(07)63240-5

51. Levy, G. N., Schindel, R., & Kruth, J. P. (2003ay). Rapid manufacturing and rapid tooling with layer manufacturing (LM) technologies, state of the art and future perspectives. *CIRP Annals - Manufacturing Technology*, *52*(2), 589–609. https://doi.org/10.1016/S0007-8506(07)60206-6

52. Yang, S., & Zhao, Y. F. (2015az). Additive manufacturing-enabled design theory and methodology: a critical review. *International Journal of Advanced Manufacturing Technology*, *80*(1–4), 327–342. https://doi.org/10.1007/s00170-015-6994-5

53. He, Y., Ye, M., & Wang, C. (2006ba). A method in the design and fabrication of exact-fit customized implant based on sectional medical images and rapid prototyping technology. *International Journal of Advanced Manufacturing Technology*, *28*(5–6), 504–508. https://doi.org/10.1007/s00170-004-2406-y

54. Brennan-Craddock, J., Brackett, D., Wildman, R., & Hague, R. (2012bb). The design of impact absorbing structures for additive manufacture. *Journal of Physics: Conference Series*, *382*(1), 2–9. https://doi.org/10.1088/1742-6596/382/1/012042

55. Dehoff, R. R., & Babu, S. S. (2010bc). Characterization of interfacial microstructures in 3003 aluminum alloy blocks fabricated by ultrasonic additive manufacturing. *Acta Materialia*, *58*(13), 4305–4315. https://doi.org/10.1016/j.actamat.2010.03.006

56. Hehr, A., Norfolk, M., Wenning, J., Sheridan, J., Leser, P., Leser, P., & Newman, J. A. (2018bd). Integrating Fiber Optic Strain Sensors into Metal Using Ultrasonic Additive Manufacturing. *Jom*, *70*(3), 315–320. https://doi.org/10.1007/s11837-017-2709-8

57. Hehr, A., Wenning, J., Norfolk, M., Sheridan, J., Newman, J. A., & Domack, M. (2019be). Selective Reinforcement of Aerospace Structures Using Ultrasonic Additive Manufacturing. *Journal of Materials Engineering and Performance*, *28*(2), 633–640. https://doi.org/10.1007/s11665-018-3614-1

58. Friel, R. J., & Harris, R. A. (2013bf). Ultrasonic additive manufacturing A hybrid production process for novel functional products. *Procedia CIRP*, *6*(1), 35–40. https://doi.org/10.1016/j.procir.2013.03.004

59. Gokuldoss, P. K., Kolla, S., & Eckert, J. (2017bg). Additive manufacturing processes: Selective laser melting, electron beam melting and binder jetting-selection guidelines. *Materials*, *10*(6). https://doi.org/10.3390/ma10060672

60. Miyanaji, H. (2018bh). *Binder jetting additive manufacturing process fundamentals and the resultant influences on part quality*. 204. https://doi.org/https://doi.org/10.18297/etd/3058

61. Bai, Y., & Williams, C. B. (2015bi). An exploration of binder jetting of copper. *Rapid Prototyping Journal*. https://doi.org/10.1108/RPJ-12-2014-0180

62. Varotsis, A. B. (2019bj). Introduction to Binder Jetting 3D printing. In *3D Hubs*.

63. National Institute of Standards and Technology. (2018bk). *Laser Powder Bed Fusion Thermography*. https://www.nist.gov/el/lpbf-thermography

64. Kusuma, C. (2016bl). *The Effect of Laser Power and Scan Speed on Melt Pool Characteristics of Pure Titanium and Ti-6Al-4V Alloy for Selective Laser Melting Repository Citation Kusuma, Chandrakanth, "The Effect of Laser Power and Scan Speed on Melt Pool Characteristics of*. https://corescholar.libraries.wright.edu/etd_all%22

65. Buchbinder, D., Schleifenbaum, H., Heidrich, S., Meiners, W., & Bültmann, J. (2011bm). High power Selective Laser Melting (HP SLM) of aluminum parts. *Physics Procedia*, *12*(PART 1), 271–278. https://doi.org/10.1016/j.phpro.2011.03.035

66. Aboulkhair, N. T., Everitt, N. M., Ashcroft, I., & Tuck, C. (2014bn). Reducing porosity in AlSi10Mg parts processed by selective laser melting. *Additive Manufacturing*, *1*, 77–86. https://doi.org/10.1016/j.addma.2014.08.001

67. Conner, B. P., Manogharan, G. P., Martof, A. N., Rodomsky, L. M., Rodomsky, C. M., Jordan, D. C., & Limperos, J. W. (2014bo). Making sense of 3-D printing: Creating a map of additive manufacturing products and services. *Additive Manufacturing*, *1*, 64–76. https://doi.org/10.1016/j.addma.2014.08.005

68. Mumtaz, K. A., & Hopkinson, N. (2010bp). Selective Laser Melting of thin wall parts using pulse shaping. *Journal of Materials Processing Technology*, *210*(2), 279–287. https://doi.org/10.1016/j.jmatprotec.2009.09.011

69. Rombouts, M., Kruth, J. P., Froyen, L., & Mercelis, P. (2006bq). Fundamentals of Selective Laser Melting of alloyed steel powders M. *CIRP Annals - Manufacturing Technology*, *55*(1), 187–192.

70. Song, B., Dong, S., Deng, S., Liao, H., & Coddet, C. (2014br). Microstructure and tensile properties of iron parts fabricated by selective laser melting. *Optics and Laser Technology*, *56*, 451–460. https://doi.org/10.1016/j.optlastec.2013.09.017

71. Guo, W., Zeng, Z., Zhang, X., Peng, P., & Tang, S. (2015bs). Low-temperature sintering bonding using silver nanoparticle paste for electronics packaging. *Journal of Nanomaterials*, *2015*. https://doi.org/10.1155/2015/897142

72. Bai, J. G., Zhang, Z. Z., Calata, J. N., & Lu, G. Q. (2006bt). Low-temperature sintered nanoscale silver as a novel semiconductor device-metallized substrate interconnect material. *IEEE Transactions on Components and Packaging Technologies*. https://doi.org/10.1109/TCAPT.2005.853167

73. Jakubowska, M., Jarosz, M., Kiełbasinski, K., & Młoniak, A. (2011bu). New conductive thick-film paste based on silver nanopowder for high power and high temperature applications. *Microelectronics Reliability*, *51*(7), 1235–1240. https://doi.org/10.1016/j.microrel.2011.04.015

74. Zhang, P., Wei, R., Zeng, J., Cai, M., Xiao, J., & Yang, D. (2016bv). Thermal Properties of Silver Nanoparticle Sintering Bonding Paste for High-Power LED Packaging. *Journal of Nanomaterials*, *2016*. https://doi.org/10.1155/2016/8681513

75. Okada, S., Nakahara, Y., Watanabe, M., Tamai, T., Kobayashi, Y., & Yajima, S. (2019bw). Roomerature Sintering of Tri- n-Octylphosphine-Oxide-Capped Silver Nanoparticle Paste by Dipping into an Organic Solvent Containing a Sintering Agent. *Journal of Physical Chemistry C*, *123*(23), 14118–14125. https://doi.org/10.1021/acs.jpcc.9b03378

76. Colpo, F., Humbert, L., Giaccari, P., & Botsis, J. (2006bx). Characterization of residual strains in an epoxy block using an embedded FBG sensor and the OLCR technique. *Composites Part A: Applied Science and Manufacturing*, *37*(4), 652–661. https://doi.org/10.1016/j.compositesa.2005.05.009

77. Botsis, J., Humbert, L., Colpo, F., & Giaccari, P. (2005by). Embedded fiber Bragg grating sensor for internal strain measurements in polymeric materials. *Optics and Lasers in Engineering*, *43*(3–5), 491–510. https://doi.org/10.1016/j.optlaseng.2004.04.009

78. Alemohammad, H., & Toyserkani, E. (2009bz). Simultaneous measurement of temperature and tensile loading using superstructure FBGs developed by laser direct writing of periodic on-fiber metallic films. *Smart Materials and Structures*, *18*(9). https://doi.org/10.1088/0964-1726/18/9/095048

79. Alemohammad, H., & Toyserkani, E. (2009ca). Modification of the Optical Performance of Fiber Bragg Gratings Using Femtosecond Laser Micromachining. *Journal of Laser Micro/Nanoengineering*, *4*(1), 61–65. https://doi.org/10.2961/jlmn.2009.01.0012

80. Alemohammad, H., Toyserkani, E., & Paul, C. P. (2007cb). Fabrication of smart cutting tools with embedded optical fiber sensors using combined laser solid freeform fabrication and moulding techniques. *Optics and Lasers in Engineering*, *45*(10), 1010–1017. https://doi.org/10.1016/j.optlaseng.2007.04.006

81. Alemohammad, H., & Toyserkani, E. (2011cc). Metal embedded optical fiber sensors: Laser-based layered manufacturing procedures. *Journal of Manufacturing Science and Engineering, Transactions of the ASME*, *133*(3), 1–12. https://doi.org/10.1115/1.4004203

82. Alemohammad, H. R., Foroozmehr, E., Cotten, B. S., & Toyserkani, E. (2013cd). A dual-parameter optical fiber sensor for concurrent strain and temperature measurement: Design, fabrication, packaging, and calibration. *Journal of Lightwave Technology*, *31*(8), 1198–1204. https://doi.org/10.1109/JLT.2013.2240374

83. Tang, Y., Zhou, Y., Hoff, T., Garon, M., & Zhao, Y. F. (2016ce). Elastic modulus of 316 stainless steel lattice structure fabricated via binder jetting process. *Materials Science and Technology (United Kingdom)*, *32*(7), 648–656. https://doi.org/10.1179/1743284715Y.0000000084

84. Gurappa, I. (2002cf). Development of appropriate thickness ceramic coatings on 316 L stainless steel for biomedical applications. *Surface and Coatings Technology*, *161*(1), 70–78. https://doi.org/10.1016/S0257-8972(02)00380-8

85. Tolosa, I., Garciandía, F., Zubiri, F., Zapirain, F., & Esnaola, A. (2010cg). Study of mechanical properties of AISI 316 stainless steel processed by "selective laser melting", following different manufacturing strategies. *International Journal of Advanced Manufacturing Technology*, *51*(5–8), 639–647. https://doi.org/10.1007/s00170-010-2631-5

86. Matthews, M. J., Guss, G., Khairallah, S. A., Rubenchik, A. M., Depond, P. J., & King, W. E. (2016ch). Denudation of metal powder layers in laser powder bed fusion processes. In *Acta Materialia* (Vol. 114, pp. 33–42). https://doi.org/10.1016/j.actamat.2016.05.017

87. Harsch, M., Karger-Kocsis, J., & Herzog, F. (2007ci). Strain development in a filled epoxy resin curing under constrained and unconstrained conditions as assessed by Fibre Bragg Grating sensors. *Express Polymer Letters*, *1*(4), 226–231. https://doi.org/10.3144/expresspolymlett.2007.34

88. Staub, A., Spierings, A. B., & Wegener, K. (2019cj). Correlation of meltpool characteristics and residual stresses at high laser intensity for metal lpbf process. *Advances in Materials and Processing Technologies*, *5*(1), 153–161. https://doi.org/10.1080/2374068X.2018.1535643

89. Kruth, J. P., Froyen, L., van Vaerenbergh, J., Mercelis, P., Rombouts, M., & Lauwers, B. (2004ck). Selective laser melting of iron-based powder. *Journal of Materials Processing Technology*, *149*(1–3), 616–622. https://doi.org/10.1016/j.jmatprotec.2003.11.051

90. Chiang, C.-C. (2011cl). Curing Monitoring of Composite Material Using Embedded Fiber Bragg Grating Sensors. *Advances in Composite Materials - Analysis of Natural and Man-Made Materials*, *September 2011*. https://doi.org/10.5772/18799

91. Thingbo, D., Kringlebotn, J. T., Nakstad, H., & Ronnekleiv, E. (2006cm). *OPTICAL WAVELENGTH INTERROGATOR*.

92. Kolb, T., Mahr, A., Huber, F., Tremel, J., & Schmidt, M. (2019cn). Qualification of channels produced by laser powder bed fusion: Analysis of cleaning methods, flow rate and melt pool monitoring data. *Additive Manufacturing*, *25*(November 2018), 430–436. https://doi.org/10.1016/j.addma.2018.11.026

93. Roths, J., Wilfert, A., Kratzer, P., Jülich, F., & Kuttler, R. (2010co). Strain calibration of optical FBG-based strain sensors. *Fourth European Workshop on Optical Fibre Sensors*, *7653*(September 2010), 76530F. https://doi.org/10.1117/12.866428

94. Kaur, N. (2019cp). *Optoelectronic Humidity and Temperature Sensor using Apodized Pi-Phase Shifted Fiber Bragg Grating A Thesis The Department of Electrical and Computer Engineering*. https://spectrum.library.concordia.ca/984978/

95. Thompson, A. C., Brown, W. G. A., Stoddart, P. R., & Wade, S. A. (2010cq). Bend effects on fibre Bragg gratings in standard and low bend loss optical fibres. *35th Australian Conference on Optical Fibre Technology, ACOFT 2010, January*. https://doi.org/10.1109/acoft.2010.5929958